Analysis of Mono-jet Events at the Tevatron

by

Patrick Eraerds

Diploma Thesis in Physics

presented to the

Faculty for Mathematics, Computer Science and Natural Sciences
of the RWTH University of Aachen, Germany

in March 2006

performed in the

III. Physiscs Institute A
Prof. Dr. Thomas Hebbeker

Abstract

This diploma thesis presents the first wide p_t range (starting from 30 GeV) investigation of central ($|\eta| < 0.4$) mono-jets ($\mathcal{R}_{cone} = 0.7$) using the DØ detector and an integrated luminosity of 396 pb^{-1} of $p\bar{p}$ collisions at $\sqrt{s} = 1.96$ TeV from RunII of the Tevatron.

In the particular case of charged mono-jets no excess in data with respect to the Standard Model prediction was found.

In the particular case of neutral mono-jets an excess in data with respect to the Standard Model prediction was found. This excess most likely originates from un- simulated noise-jets.

Contents

Chapter 1

Introduction

Nowadays physics is divided into lots of different branches like atom physics, nuclear physics, elementary particle physics, solid-state physics, plasma-physics, biophysics, cosmology etc. Each branch explores nature on some specific length scale. The cornerstones are cosmology on the large scale (10^{26} m) and elementary particle physics on the small scale (10^{-18} m).

This diploma thesis deals with a particular topic of elementary particle physics called "mono-jets". This is a label for a certain event topology containing exactly one jet (section 4.1) and "nothing" else.

From the detector point of view such events seem to violate momentum conservation. From the particle point of view (assuming momentum conservation) a parton and undetectable particles (undetectable with respect to the detector used) are created.

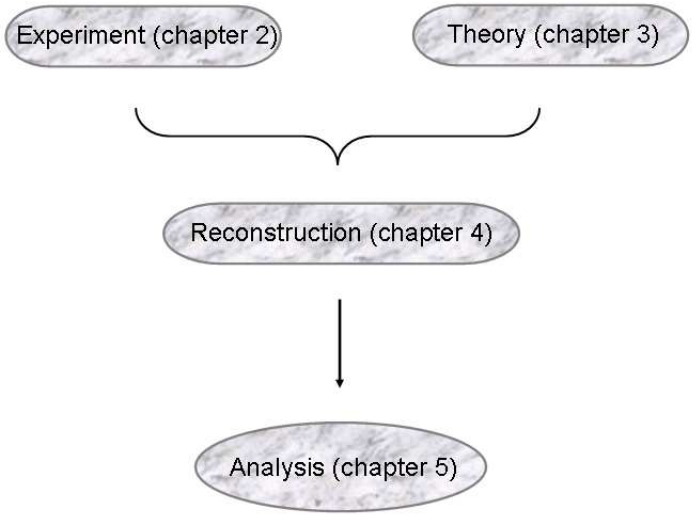

Figure 1.1: Structure of this thesis.

Besides the neutrino there are no other currently confirmed particles which are able to escape the detector without a direct signal.
Thus an excess of mono-jet events with respect to the ones expected from the established theory (the Standard Model) would indirectly indicate the existence of yet unknown parti-

cles.

More recent theories, like enhanced (Kaluza-Klein) gravitation from large extra spatial dimensions or Supersymmetry predict new stable particles (KK graviton and neutralino). These are expected to traverse the detector without recognition and thus they are candidates to appear in the mono-jet channel.

Earlier searches performed by the CDF [1] and DØ [2] collaborations set limits on model parameters but found no evidence for new particles.

Unlike other analyses, this analysis searches the mono-jet channel for deviations from the Standard Model in general, starting at a jet transverse momentum of 30 GeV.

The course of this diploma thesis is displayed in Fig. 1.1.

In chapter 2 the experimental setup is presented, illustrating the most important parts. Chapter 3 reviews some basic principles and notions of particle theory and describes how data coming from the detector is compared to theoretical calculations.
Chapter 4 deals with the reconstruction of particle interactions on the basis of real and simulated detector outputs. Chapter 5 is concerned with the actual mono-jet analysis.

Chapter 2

Experimental Setup

Elementary particle interactions are probed in scattering experiments. A huge accelerator machine accelerates particles to some energy level. At defined interaction points they are brought into head-on collision. Then a detector observes what comes out.
The data to be analysed in this thesis was taken by the DØ detector. It is one of several experiments driven at the Fermi National Accelerator Laboratory (Fermilab, Fig. 2.1), located about 40 miles west of Chicago. Fermilab is one of the leading laboratories advancing the understanding in the elementary particle physics area. It was comissioned by the U.S. Atomic Energy Commission on November 21, 1967. Founding director was Robert R. Wilson.
The most outstanding achievements were the discoveries of the bottom quark in June 1977 (E288 collaboration) and the top quark in Febrary 1995 (DØ in companion with the CDF collaboration).
The history of the DØ experiment is divided into two data taking periods, Run I (1991-1996) and Run II (2001-2009). The time between those runs was used to accomplish major upgrades of several detector parts and the accelerators.
In this chapter the most important parts of the particle accelerator and the Run II DØ detector are presented.

2.1 The Accelerator

The huge particle accelerator at Fermilab, the Tevatron, accelerates protons and antiprotons up to energies of about 980 GeV, yielding a collision energy of 1.96 TeV in total. To provide protons and antiprotons at this energy, several production and acceleration steps have to be passed.

2.1.1 Acceleration Chain

The main parts of the Tevatron and their purposes :

- H^- **generator** (starting point in Fig. 2.2)

  H^- are generated by streaming H_2 gas over a catalytic surface in presence of free electrons. The obtained H^- ions are led into a Cockroft Walton preaccelerator.

Figure 2.1: The FERMILAB site.

- **Preaccelerators**

  After acquiring an energy of 750 keV in the Cockroft Walton the H^- ions are injected into the linear accelerator gaining energy up to 400 MeV. At its end they hit a carbon foil. While passing through the foil the H^- ions strip off both electrons. The remaining proton then reaches the booster synchroton, gaining an energy of 8 GeV ($\rightarrow$ main injector).

- **Antiproton source**

  The main injector (see below) provides 120 GeV protons, which are shot onto a nickel target. This induces a lot of secondary particles including antiprotons. These are collected and led into the antiproton debuncher.

- **Antiproton debuncher**

  The antiprotons coming from the nickel target at different energies get homogenized inside the antiproton debuncher. After the homogenization they have energies of about 8 GeV.

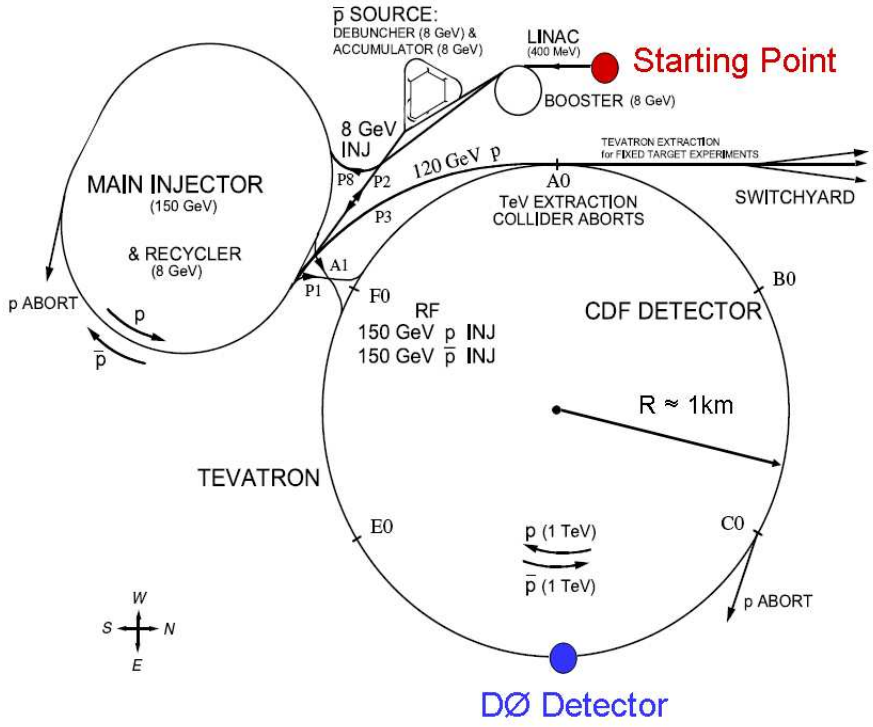

Figure 2.2: The Tevatron acceleration chain [5].

- **Antiproton accumulator**

  Accumulates the homogenized antiprotons from the debuncher and keeps their energy at 8 GeV. Once enough antiprotons are collected they are led into the main injector.

- **Antiproton recycler**

  The antiproton recycler was once built as an accumulator for antiprotons stemming from reduced antiproton bunches (see below) from the Tevatron main ring. These days it serves as an additional accumulator for newly produced antiprotons.

- **Main injector**

  The main injector has to fulfill several tasks :

  - Acceleration of protons (coming from the booster synchrotron) from 8 up to 150 GeV (counterclockwise)
  - Extraction of a fraction of protons at 120 GeV, which are then led onto the nickel target to produce antiprotons

  - Acceleration of antiprotons coming from the accumulator from 8 up to 150 GeV (clockwise)
  - Injection of protons and antiprotons into the Tevatron main ring

- **Tevatron main ring**

  Accelerates protons (moving clockwise) and antiprotons (moving counterclockwise) from 150 GeV to 980 GeV. This equals a velocity of 99.999948% of the speed of light.

Protons and antiprotons are grouped into small packages called bunches. At two interaction points, where the detectors (CDF and DØ) are located, a proton bunch penetrates an antiproton bunch. The higher the density of these bunches the more probable an interaction occurs.

A measure for the interaction rate is the instantaneous luminosity $\mathcal{L}_{inst}$ (see also section 2.2.4). It is subject to steady improvement. Figures 2.3 and 2.4 show the evolutions of the (peak)instantaneous and the integrated luminosity[1].

Once the Tevatron main ring is filled with protons and antiprotons bunches a so-called store begins. It lasts for about 15 to 20 hours. During this time protons and antiprotons get lost, due to interactions among each other and with the beam pipe material. This causes a decreasing luminosity. If the luminosity falls below some operational limit, the remaining protons and antiprotons are aborted (end of store) and the ring is filled again.

A store itself is divided into subsections called runs. These can last up to 4 hours. A run is characterized by fixed data taking parameters. Due to the decreasing luminosity during a store, parameters like for instance trigger prescales (section 4.1.3) have to be readjusted in-between runs.

2.1.2 Tevatron Bunch and Time Structure

As mentioned before protons and antiprotons are grouped into bunches. These bunches have static positions relative to each other (Fig. 2.5).
A full revolution of a bunch in the Tevatron main ring lasts 21 μs (the revolution frequency is about 47.7 kHz). A revolution interval is divided into 1113 units of 18.8 ns, called radio frequency buckets (RFbs). This is the smallest time unit the Tevatron deals with. A so-called tick consists of 7 of those RFbs. One revolution lasts 159 ticks.

36 proton and 36 antiproton bunches revolve the Tevatron unswervingly (in opposite direction). They are grouped in 3 superbunches consisting of 12 bunches each. The first bunch in a superbunch is placed on the first RFb of a tick. Two empty ticks follow and the fourth tick is populated with the second bunch an so on. Thus two bunches are separated by 21 Rfbs $\simeq$ 396 ns.
Superbunches are separated by roughly 2.6 μs. Additional information on this can be found in [4].

[1] Which is just the integral of the instantaneous Luminosity with respect to time.

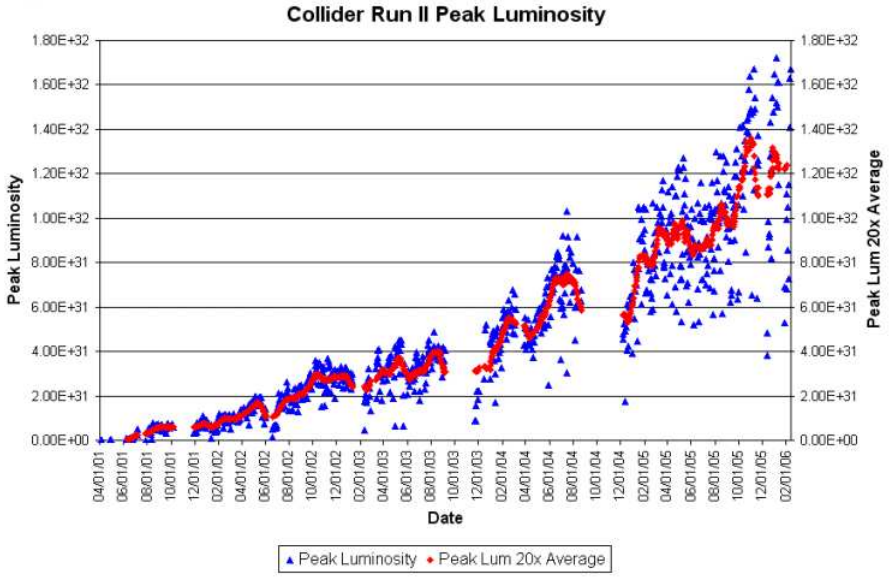

Figure 2.3: Evolution of the peak (instantaneous) luminosity [3].

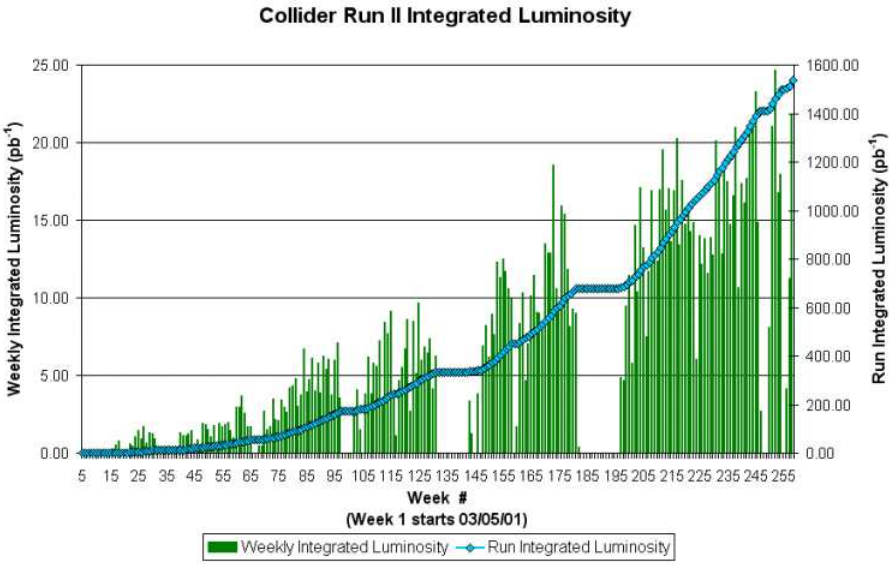

Figure 2.4: Evolution of the integrated luminosity [3].

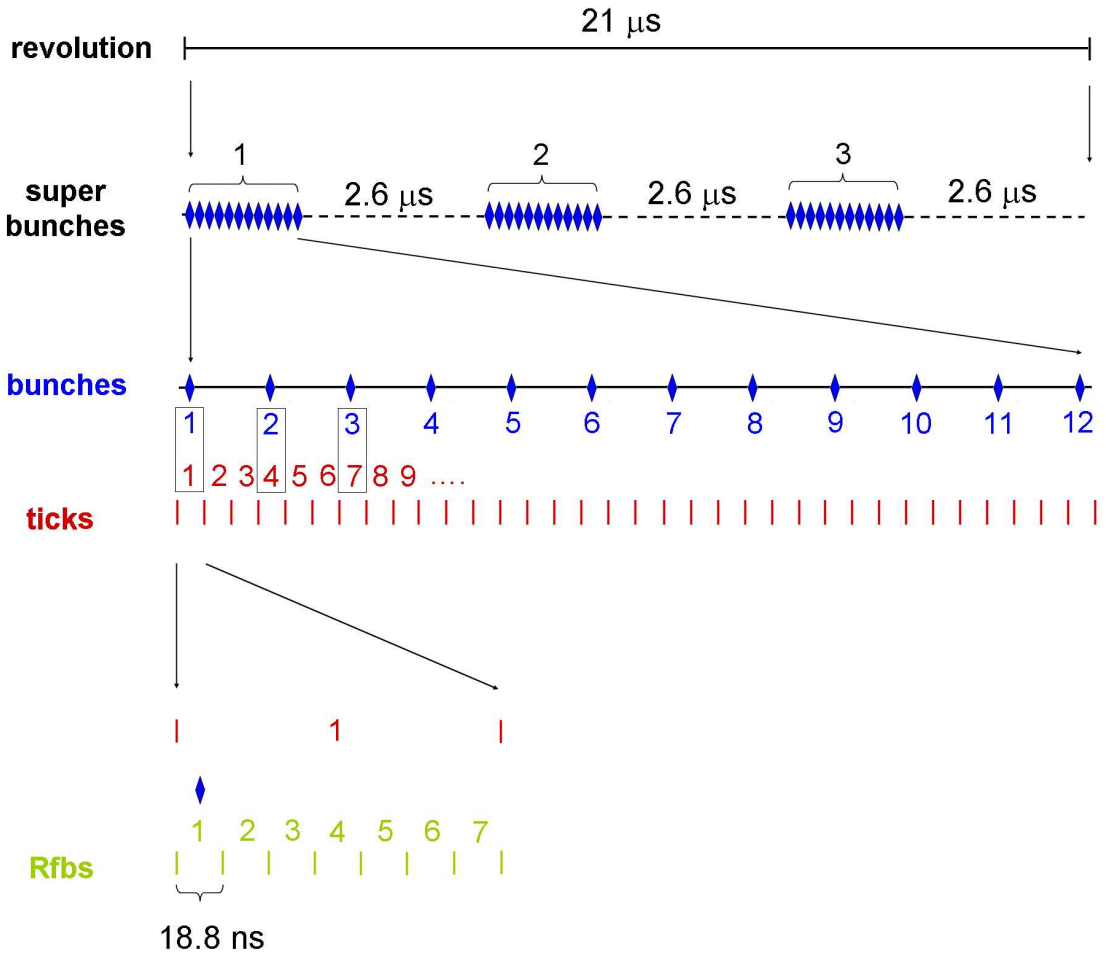

Figure 2.5: Bunch and time structure of the Tevatron main ring.

2.2 The DØ Detector

The DØ detector (Fig. 2.6) is designed like most modern high energy physics detectors. It exhibits the typical layer structure, starting with the central tracking system (consisting of a silicon tracker, a fiber tracker and a solenoid), followed by the calorimeter with its electromagnetic and hadronic parts and last the muon system (consisting of a toroid magnet, drift tubes and scintillators).

The design is due to the knowledge of the properties of known particles. The crucial

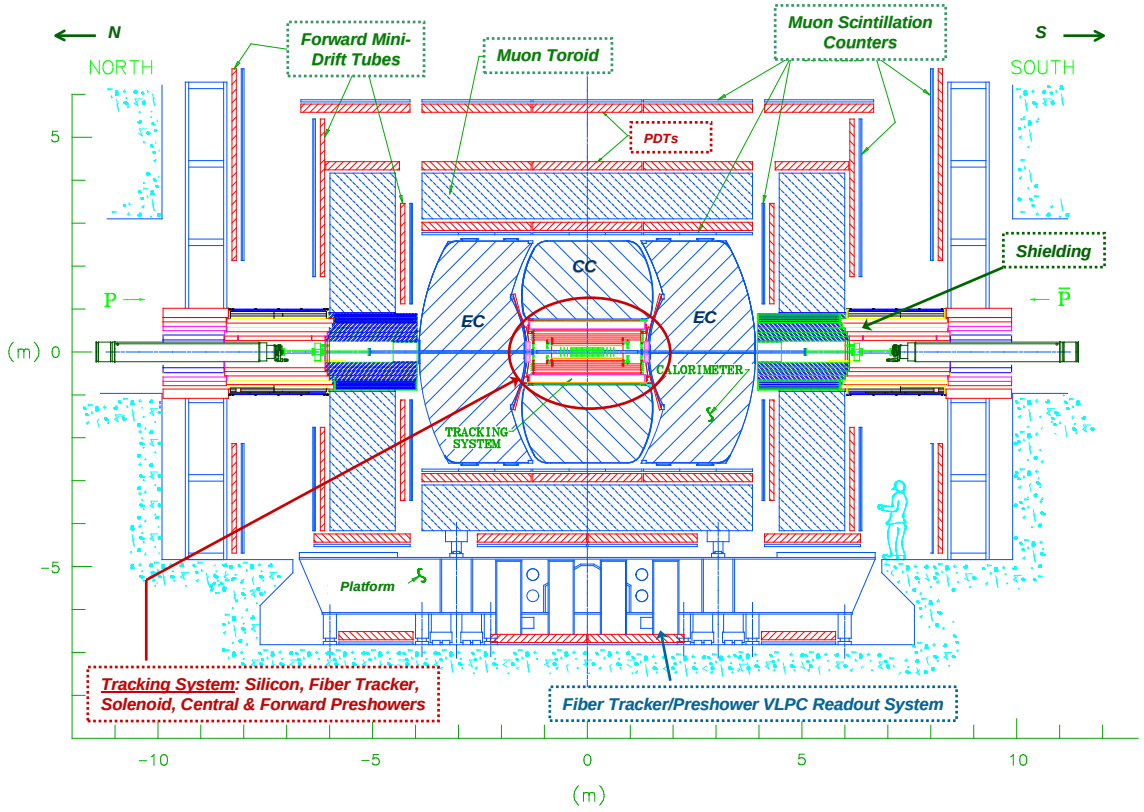

Figure 2.6: The DØ Detector [5].

quantity for electrons and positrons is the material dependent radiation length X_0. It indicates, after which length of flight through some material, the probability to initiate an electromagnetic shower is higher than 63%. Almost the same holds for photons, however the probability is about 54%[2].

The corresponding quantity for strong interacting particles is the material dependent interaction length λ. It indicates after which length of flight the probability to initiate a hadronic shower is higher than 63%.

To get sensible track information of charged particles, the tracking system has to be sufficiently transparent, i.e the effective material length has to be much smaller than the radiation and interaction lengths. Otherwise the probability of initiating a shower is not negligible and no sensible track information to determine the initial momentum (via curvature of the track due to the solenoid field) of the particle can be obtained.

[2]This is due to the different mechanisms of energy loss (bremsstrahlung (electron) and pair production (photon)).

The opposite strategy is applied in the calorimeter. Several radiation and interaction lengths of material are used to enclose electromagnetic and hadronic showers. Due to the fact that for the used materials (uranium, copper) the radiation length is sufficiently smaller than the interaction length [3], electromagnetic and hadronic showers can be separated. Electromagnetic showers primarily evolve in the front section, while hadronic showers primarily evolve in the back section of the calorimeter.

Muons have a mass roughly 200 times greater than the electron. The probability of initiating an electromagnetic shower is propotional to $\frac{E}{m^2}$, where E is the particle energy. This yields an additional factor of $\frac{1}{40000}$. For muon energies achieved at the Tevatron the obtained probability is negligible. Thus the muon can traverse the tracking system, calorimeter and the toroid magnet of the muon system without initiating a shower and loosing significant amounts of its energy (only due to ionization, which is roughly 2 GeV) . Besides the neutrino it is the only known elementary particle (see Table 3.1) expected to be present outside the massive toroid.

Drift tubes and scintillators, deployed outside the toroid, measure the transition of muons.

Neutrinos cannot be observed directly with this detector. It is the only known elementary particle leaving the detector without any direct signal (see also section 4.4) .

An adequate detector coordinate system as well as basic kinematic variables (used in the following) are given in appendix A.1.

The following sections will cover basic detector components in greater detail.

2.2.1 Central Tracking System

The central tracking system consists of a silicon microstrip tracker (SMT, Fig. 2.7), a scintillating fiber tracker (called central fiber tracker (CFT), Fig. 2.8) and a 2-Tesla-solenoid solenoid magnet.

SMT :

The SMT is directly mounted on the beampipe (the inner radius is about 2.6 cm). Its silicon microstrip detectors are arranged in two different structures, barrels and disks. Each barrel is equipped with 4 concentric layers of single-sided as well as double-sided microstrip detector ladders with straight as well as 2° stereo strips. In total there are 6 barrels arranged symmetrically around the nominal interaction point (z=0).

Secondary there are 16 disks, 12 double-sided so-called F-disks with small diameter (about 20 cm), where 4 of them are sandwiched between the barrel segments, and 4 single-sided so-called H-disks with large diameter (about 52 cm) located in the outer region. The disks are deployed to cover regions of large pseudorapidity (up to $|\eta| \simeq 3$). Altogether there are 912 modules with roughly 800000 read out channels.
The single point resolution has been shown to be ≤ 10 μm [8].

[3] For most materials the radiation length is smaller than the interaction length.

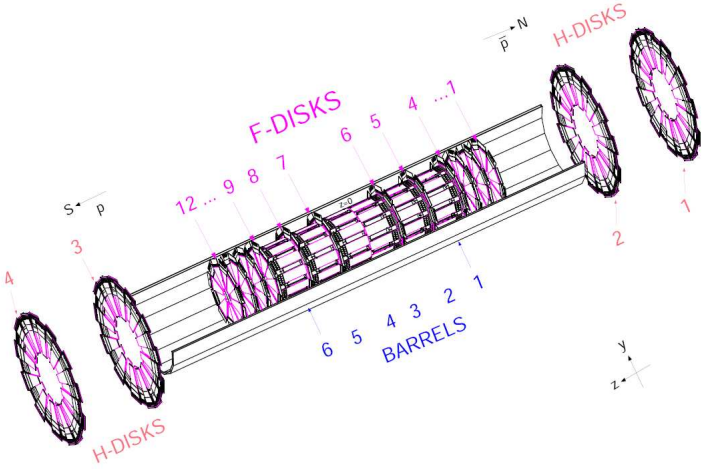

Figure 2.7: The Silicon Microstrip Tracker (SMT) [7].

CFT :

Additional tracking information, is provided by the central fiber tracker. It surrounds the SMT (Fig. 2.6). 74000 scintillating fibers (diameter=835 μm) are mounted on 8 concentric cylinders. Each cylinder supports a double layer of fibers. Layers of straight fibers alternate with $2° - 3°$ stereo fibers. The outer cylinder provides coverage for $|\eta| < 1.7$ and has a radius of about 52 cm. The stand-alone spatial resolution of the fiber tracker is about 100 μm [8]. Together with the SMT it provides a track resolution of about 35 μm for $|\eta| < 2.0$.

The solenoid magnet surrounds both the SMT and CFT. The magnetic field bends tracks of charged particles. From the curvature of the tracks the momentum can be determined. The momentum resolution of the combined tracking system is shown in Fig. 2.9. Since the determination of the momentum depends on the spatial resolution of the tracker, the momentum resolution gets worse as soon as tracks get straight, i.e. the momentum gets large.

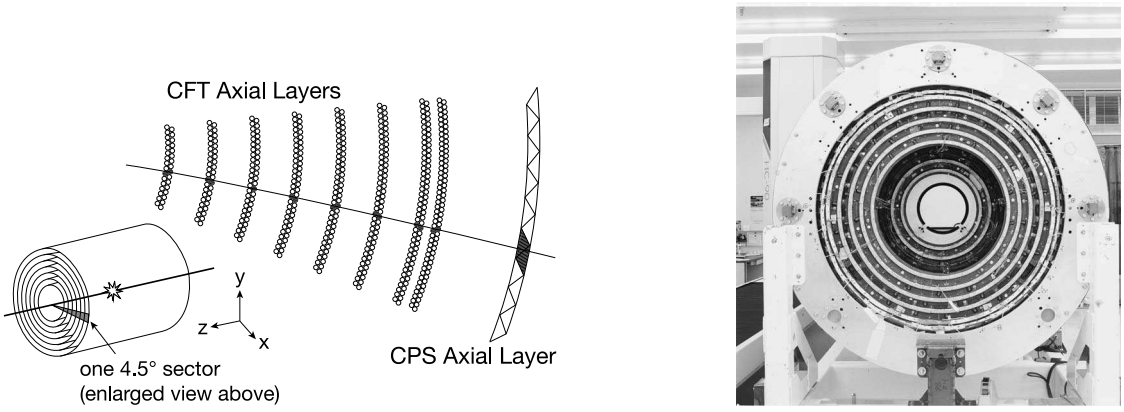

Figure 2.8: Sketch of CFT layers and frontview [9]. On the left also the Central Pre Shower Detector (CPS) is indicated. It is not utilized in this analysis.

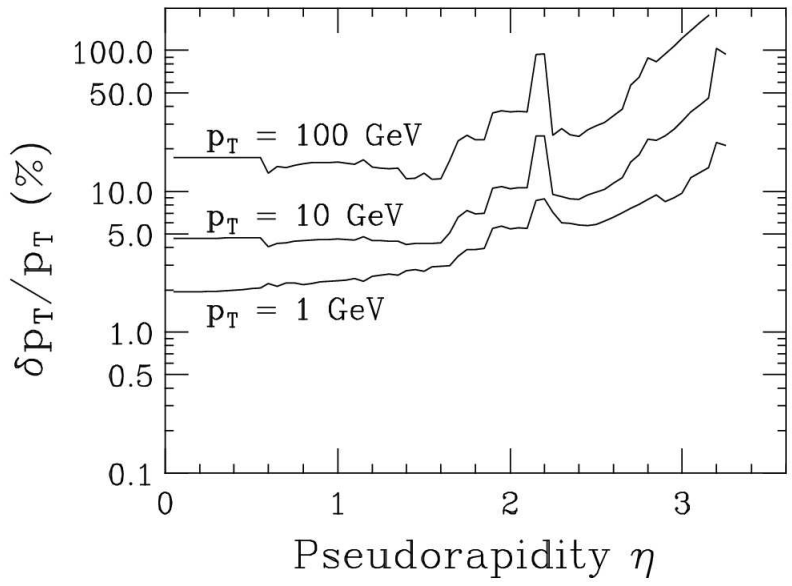

Figure 2.9: Momentum resolution of central tracking system for 3 different values of the transverse momentum p_t as a function of the pseudorapidity [10].

2.2.2 Calorimeter

The DØ calorimeter is an uranium-liquid-argon sampling calorimeter (Fig. 2.10 and Fig. 2.11). It is divided into 3 parts, two endcaps and a central part. Liquid argon as the active medium requires constant low temperature of about 78K. Therefore each part is located inside its own cryostat.

The sampling structure is shown in Fig. 2.11. Different absorber plates are used, according to the electromagnetic, coarse and fine hadronic sections. In the electromagnetic sections thin plates (3 and 4 mm in the central region and endcaps, respectively) made of nearly pure depleted uranium are utilized. The fine hadronic sections are made from 6 mm thick uranium-niobium alloy and the coarse hadronic modules contain relatively thick (46.5 mm) plates of copper (in the central region) or stainless steel (in the endcaps). Altogether the electromagnetic part has an effective length of roughly 21 radiation lenghts X_0, which is less than one interaction length ($\simeq 0.8\lambda$). The hadronic part has an effective length of about 7 interaction lengths λ in total.

To transform particle energy into a measurable signal, an electric field is set up between the absorber plates and readout pads. This is done by grounding the absorber plates and connecting the signal pads to a positive high voltage of about 2 kV. A traversing charged particle ionizes the liquid argon. These secondary charged particles are then pulled to the absorber plates and signal pads[4], yielding an electrical signal proportional to the energy of the initial particle. The electron drift time across the liquid argon gap (2.3 mm) is about 450 ns.

Several unit cells (Fig. 2.11, left) are connected to form the smallest readout unit called calorimeter cell. Calorimeter cells with roughly the same η and ϕ form a calorimeter tower. Such a tower is indicated by the shading in Fig.2.11. The η and ϕ width of each of these towers is about 0.1, dividing the η-ϕ-space into squares of 0.1×0.1.

[4]Electrons are pulled to signal pads, ions are pulled to absorber plates.

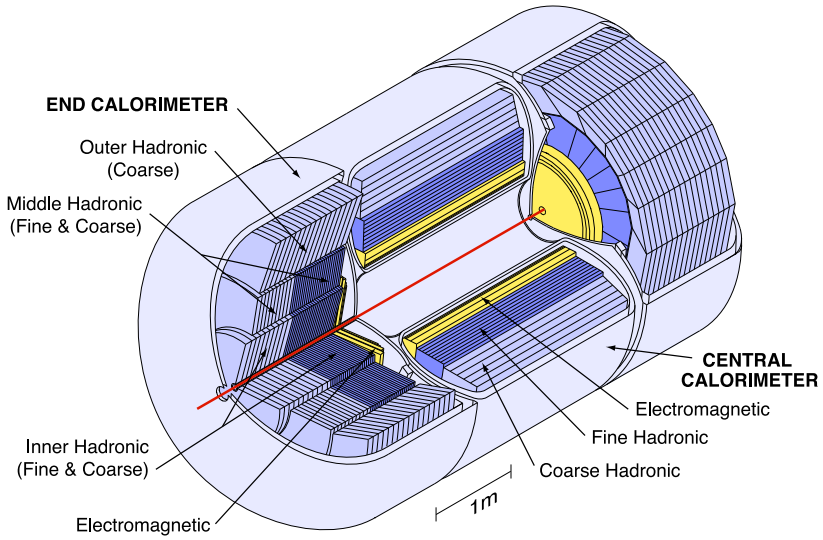

Figure 2.10: The DØ Calorimeter [11].

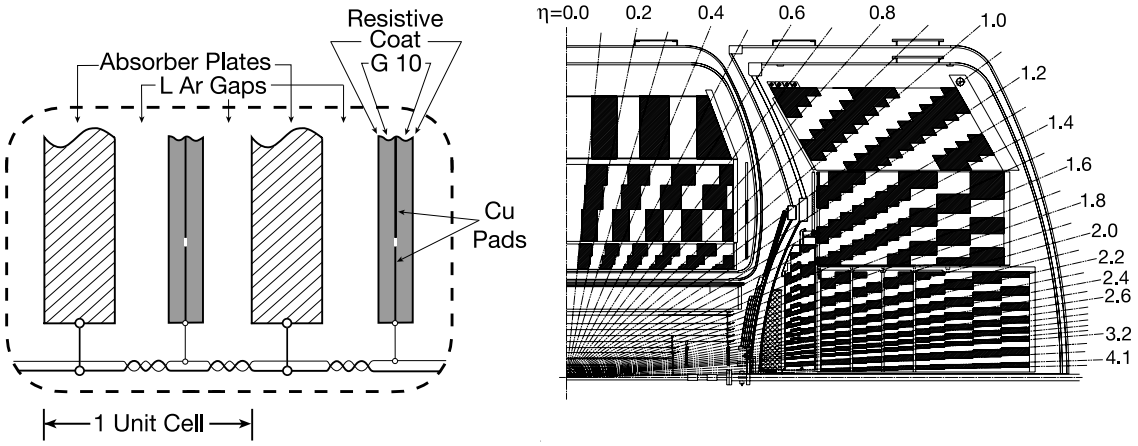

Figure 2.11: Sampling structure and segmentation (calorimeter towers) of the DØ calorimeter [11].

The energy resolution for single particles is described by the following expression :

$$\frac{\Delta E}{E} = \sqrt{C^2 + \frac{S^2}{E} + \frac{N^2}{E^2}}$$

where

- C accounts for calibration and other systematic errors
- S accounts for fluctuations due to the sampling structure of the calorimeter
- N accounts for residual radioactivity from the uranium, causing additional energy depositions not coming from the scattering event

These constants were determined using charged pions [12] and electrons [13] from a test beam. They are displayed in Table 2.1.

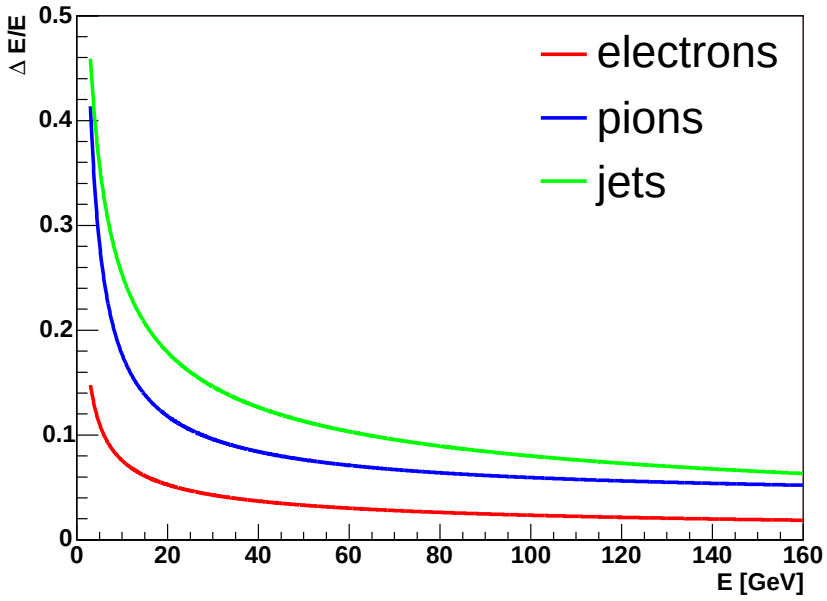

Figure 2.12: Energy resolution of the calorimeter for electrons, pions and jets.

particle	C	S [$\sqrt{\text{GeV}}$]	N [GeV]
e	0.004	0.23	0.202
π	0.045	0.45	0.975

Table 2.1: Constant term (C), sampling (S) and noise (N) constant of the DØ calorimeter.

The energy resolution of jets (section 4.1.1) can be approximately parametrized by [14]

$$\frac{\Delta E}{E} = \frac{0.8}{\sqrt{E/\text{GeV}}}$$

The resolutions are plotted in Fig. 2.12.

Note : The area between central and endcap calorimeters is called intercryostat region (ICR). To sample the energy of showers which might get lost in the cryostat wall, an additional detector, the intercryostat detector (ICD) ranging form $|\eta|$=1.1 to $|\eta|$=1.4 was deployed. The output of the ICD was not utilized in this analysis.

2.2.3 Muon System

The muon system constitutes the outermost layer (Fig. 2.6). It consists of three layers of scintillators and drift tubes (layers A,B and C) and a massive 1.8-Tesla toroid magnet. The magnet again, is necessary to be able to determine the momentum from track curvature. The A layer is inside, the B and C layers are outside the toroid. The system covers a region up to $|\eta| = 2.0$.
The scintillators primarily serve as fast readout modules (the time resolution is about 2.2

ns [15]), giving fast information about the presence of a muon (→ used for triggering (sect. 2.2.5)).

The slower drift tubes (drift times up to 450 ns) measure the tracks of traversing muons. The spatial resolution of the forward drift tubes is $\simeq 0.8$ mm [16].

The momentum resolution can be parametrized by [17]:

$$\frac{\Delta p_t}{p_t} = \sqrt{A^2 p_t^2 + B^2}$$

where A accounts for the limited spatial resolution (cp. with central tracker) and B accounts for multiple scattering in the muon toroid[5]. The reolution parameters are given in Table 2.2. The resolution is plotted in Fig. 2.13.

Central		Forward	
A	B	A	B
0.00437	0.348	0.00184	0.269

Table 2.2: Momentum resolution parameters of the local muon system.

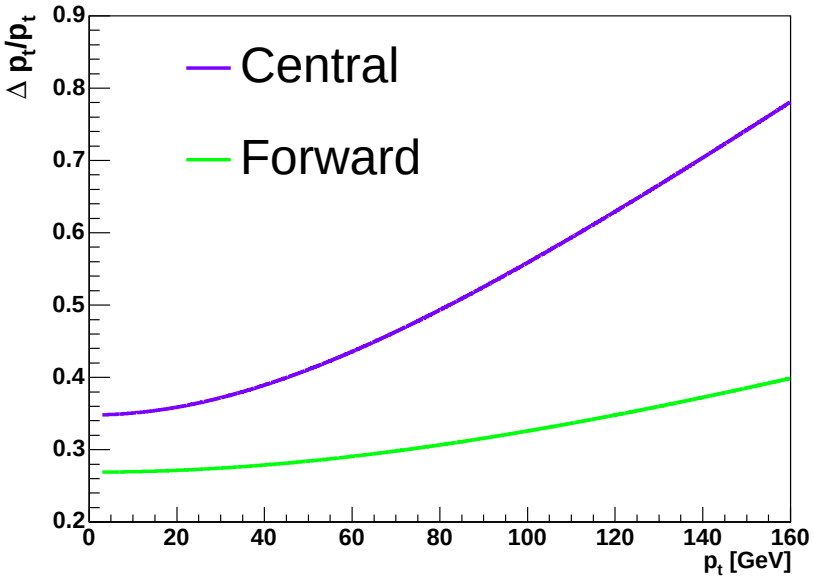

Figure 2.13: Momentum resolution of central and forward muon system.

More detailed information on the muon system can be found in [16].

[5] The muon momentum may be distorted by scattering inside the toroid.

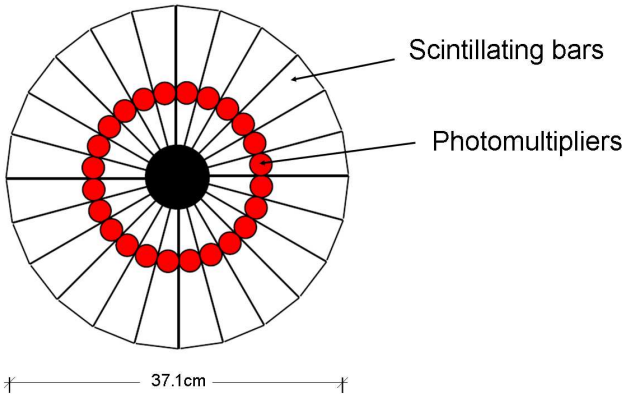

Figure 2.14: Luminosity Monitor [57].

2.2.4 Luminosity and Luminosity Monitor

Every particle physics process like for example $q\bar{q} \rightarrow \mu\nu$ occurs with some probability. A measure for that probability is the cross section σ of the process. The more possible interactions an accelerator provides, the more processes of some kind occur.
The instantaneous luminosity $\mathcal{L}_{inst}$ characterizes the provision of possible interactions of an accelerator per time unit, such that the product of $\mathcal{L}_{inst}$ and σ yields the actual rate $\frac{dN}{dt}$ of events of the considered process :

$$\frac{dN}{dt} = \mathcal{L}_{inst} \cdot \sigma$$

Thus if one wants to determine σ from the event rate dN/dt, $\mathcal{L}_{inst}$ must be known.
A possibility to determine $\mathcal{L}_{inst}$ is to measure events of a process with known σ. Furthermore it is desirable to exploit a process with large cross section, to notice changes of $\mathcal{L}_{inst}$ on short time scales. A suitable process is the inclusive inelastic $p\bar{p}$ scattering.
In DØ, these events are measured with the Luminosity Monitor (LM, Fig. 2.14). This detector consists of two arrays, located at $z = \pm 140\ cm$ (Fig. 2.15), of 24 plastic scintillators radiating outward from the beam pipe, covering $2.7 < |\eta| < 4.4$.
A photomultiplier (red points) is mounted on each scintillator bar turning the scintillator light into an electrical signal.
The design of the LM only allows to measure if at least one interaction in a bunch crossing occured. Assuming that the probability of an interaction within one bunch crossing follows Poisson statistics

$$P(n) = \frac{\lambda^n}{n!} e^{-\lambda}$$

the average number λ of inelastic $p\bar{p}$ interactions per bunch crossing can be determined by counting the fraction of crossings containing no interaction :

$$P(0) = e^{-\lambda}$$

hence

$$\lambda = -\ln(P(0))$$

λ is connected with the interaction rate $dN_{p\bar{p}}/dt$ of inelastic $p\bar{p}$ interactions via the bunch-crossing frequency f_{bc} :

$$\lambda = \frac{\frac{dN_{p\bar{p}}}{dt}}{f_{bc}}$$

The interaction rate is given by

$$\frac{dN_{p\bar{p}}}{dt} = \mathcal{L}_{inst} \cdot \sigma_{p\bar{p},eff}$$

where $\sigma_{p\bar{p},eff}$ is the effective cross section of inelastic $p\bar{p}$ scattering, including factors accounting for acceptance and efficiency :

$$\sigma_{p\bar{p},eff} := \sigma_{p\bar{p}} \cdot A_{acc,eff}$$

with [18]:

$$\sigma_{p\bar{p}} = 60.7 \pm 2.4 \quad mb \quad \text{and} \quad A_{acc,eff} = 0.758 \pm 0.038$$

Thus[6]

$$\mathcal{L}_{inst} = \frac{\lambda \cdot f_{bc}}{\sigma_{p\bar{p},eff}} = \frac{-\ln(P(n=0)) \cdot f_{bc}}{\sigma_{p\bar{p},eff}}$$

The instanteneous luminosity is determined based on 60 s intervals, so-called luminosity blocks. The history of instantaneous and integrated luminosity is shown in Fig. 2.3. The error of the measured luminosity is about 6.5% [18]. Further information on this can be found in [19].

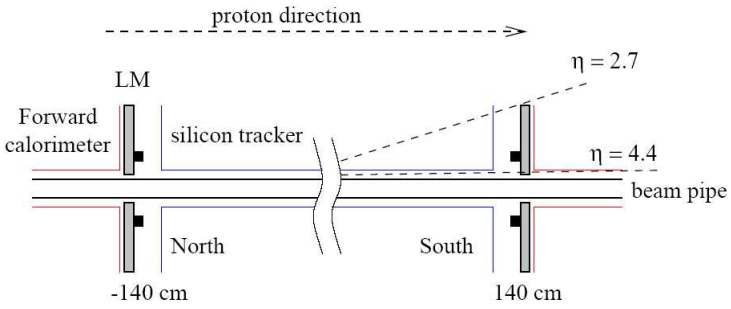

Figure 2.15: Location of the LM scintillator arrays.

2.2.5 Trigger and Data Aquisition

The $p\bar{p}$ interaction rate, including elastic scattering is about 2.5 MHz. Recording event data is restricted to 50 Hz.

However, most of the interactions are of minor interest (elastic scattering).Primarily one is interested in hard inelastic scattering events with certain characteristics. For example, a $W \to \mu\nu$ event is expected to leave a scintillator signal in the muon system or in case of a $Z \to q\bar{q}$ event, one would expect a certain amount of energy in the hadronic calorimeter.

The DØ triggersystem (computers) examines event characteristics to filter out interesting events. The selection of events and the reduction of the event rate is done in three steps, referred to as level 1, level 2 and level 3 trigger.

[6] With an instantaneous luminosity of $8 \cdot 10^{31} cm^{-2} s^{-1}$ and a bunchcrossing frequency $f_{bc} = \frac{36}{21\mu s}$ (36 : number of bunch crossings per revolution, $1/21\mu$s : revolution frequency), the average number of interactions per bunch crossing is about 2.2.

Level 1 checks basic hardware requirements such like those mentioned above. This concerns single detector subsystems (information of different subsystems is not combined). Event classes with large cross sections get prescaled. This means that only each n-th event, fulfilling the level 1 requirement is sent to level 2. Level 1 reduces the event rate to 5-10 kHz.

Stricter hardware and software requirements are checked on level 2. This includes the combination of information of different detector subsystems. By this the event rate is lowered to 1 kHz. If the event passes level 2 the full detector information is read out and digitized.

On level 3 (the final reduction) the full data of an event is combined and "pre-reconstructed". That means, that simpler versions of the actual reconstruction algorithms (section 4) are applied. According to this information events are chosen and written to tape (50 Hz). The average event size is about 250 kB.
Explicit trigger definitions (according to the different levels) can be found in [20]. Definitions of triggers used in this analysis are displayed in Table 5.2.

To ensure good data quality, a fraction of events passing level 3 gets fully reconstructed and standard distributions of physical quantities are compared to reference distributions (global monitoring). Passing this, the full data chosen by level 3 gets reconstructed. The output of this reconstruction is stored in a DØ specific format, called TMB ("thumbnail").

The next chapter covers basics of particle theory and explains how theory is actually compared with the output (electrical signals) the detector provides.

Chapter 3

Particle Theory and Simulation

3.1 General

The established theory for describing interactions (excluding gravitation) of all currently known elementary particles (Table 3.1) is the Standard Model. It is composed of two sub models, the electroweak model, a unification of Quantum Electro Dynamics (QED) and the theory of weak interactions, and Quantum Chromo Dynamics(QCD).

	properties			**interactions**				**type**
particle	mass	el.charge[e]	spin	elm.	weak	strong	gravit.	
e^-	0.511 MeV	-1	$\frac{1}{2}$	+	+	-	+	
μ^-	105.66 MeV	-1	$\frac{1}{2}$	+	+	-	+	
τ^-	1776.99 MeV	-1	$\frac{1}{2}$	+	+	-	+	lepton
ν_e	< 3eV	0	$\frac{1}{2}$	-	+	-	+	
ν_μ	< 0.19MeV	0	$\frac{1}{2}$	-	+	-	+	
ν_τ	< 18.2 MeV	0	$\frac{1}{2}$	-	+	-	+	
u[1]	2.75 MeV	$\frac{2}{3}$	$\frac{1}{2}$	+	+	+	+	
d	6 MeV	$-\frac{1}{3}$	$\frac{1}{2}$	+	+	+	+	
s	105 MeV	$-\frac{1}{3}$	$\frac{1}{2}$	+	+	+	+	quark
c	1.25 GeV	$\frac{2}{3}$	$\frac{1}{2}$	+	+	+	+	
b	4.2 GeV	$-\frac{1}{3}$	$\frac{1}{2}$	+	+	+	+	
t	174.3 GeV	$\frac{2}{3}$	$\frac{1}{2}$	+	+	+	+	
γ	$< 6 \cdot 10^{-17}$eV	$< 5 \cdot 10^{-30}$	1	+	-	-	+	
Z	91.19 GeV	0	1	-	+	-	+	gauge
W^-	80.425 GeV	-1	1	+	+	-	+	boson
gluon[2]	0	0	1	-	-	+	+	

Table 3.1: Elementary particles. For each particle listed, an antiparticle exists that has the same mass but opposite values of electrical charge and quantum numbers. The exceptions to that rule are photon and Z boson, they are both at once. Displayed masses are means of values given in [21].

Gauge principle

Technically these models are based on the principle of gauge invariance, they are gauge theories.

The free propagation of fermions (marked by spin=$\frac{1}{2}$ in Table 3.1) is described by the relativistic Dirac equation or likewise by its associated Lagrangian[3] :

$$(i\partial^\mu\gamma_\mu - m)\psi = 0 \quad ; \quad \mathcal{L} = \bar{\psi}(i\partial^\mu\gamma_\mu - m)\psi$$

where $\psi = \psi(x), (x = (t, \vec{x}))$ is an element of a vectorspace associated to the 4-dimensional spinor representation of the Lorentz group, called Dirac-spinor or Dirac-field. It is associated with the free propagating fermion and antifermion respectively[4].

A description of interacting fermions can be obtained by starting from the Lagrangian of the free theory and demanding a certain invariance (gauge invariance) with respect to the fields ψ.

In the case of electromagnetic interaction, the demand for a local U(1) invariance yields the desired result. More precisely : The desired interaction Lagrangian $\mathcal{L}_{int}$ should remain unchanged (invariant) when replacing the field

$$\psi(x) \quad \rightarrow \quad e^{i\alpha(x)}\psi(x)$$

where $e^{i\alpha(x)}$ is an element of the abelian group U(1) dependent on $\alpha(x)$, a function varying arbitrarily in space time.

The invariant Lagrangian is obtained by doing three things :

a) introduce a vectorfield A_μ which transforms like

$$A_\mu \rightarrow A_\mu - \frac{1}{e}\partial_\mu\alpha(x)$$

when applying the gauge transformation to the Dirac fields

b) replace the common derivative ∂_μ by the so-called covariant derivative :

$$D_\mu := \partial_\mu - ieA_\mu$$

c) introduce an associated kinetic term

$$\frac{1}{4}F_{\mu\nu}F^{\mu\nu} \quad \text{where} \quad F_{\mu\nu} := \partial_\mu A_\nu - \partial_\nu A_\mu$$

[1] Each quark occurs in three different color charges, thus in total there are 18 different quarks (excluding the anti-quarks)

[2] In total there are 8 different gluons.

[3] The Dirac equation is obtained from $\mathcal{L}$ via the Euler Lagrange equation.

[4] The two remaining components account for spin.

The result is :

$$\mathcal{L}_{int} = \mathcal{L}_{QED} = \bar{\psi}(iD^{\mu}\gamma_{\mu} - m)\psi - \frac{1}{4}F_{\mu\nu}F^{\mu\nu}$$

This is the Lagrangian of QED. The vectorfield A_{μ} is called gauge field. It is associated with the photon.

Quantization of Fields

It would be straight forward to apply the Euler Lagrange equation with respect to $\mathcal{L}_{QED}$ to obtain the equation of motion for electromagnetically interacting fermions. However, the solutions of that equation would not lead to a sensible description of particle interactions in the relativistic regime, i.e. $E \gg m$.
These solutions are only sufficient for problems where particle creation via $E = mc$ is prohibited, e.g. the H-atom.
To include particle creation and annihilation, the common description of a particle by assigning a classical field to it, must be overcome.
A classical field inherently exists from $t = -\infty$ to $t = +\infty$, or likewise, a classical field which does not exist at some time t_0 does not exist at any time $t_1 > t_0$.
The major step in overcoming this deficiency is the transition from the classical field to the quantized field. The quantized field is not assigned to a single particle, but rather to a particle class (e.g. class of electrons, class of u-quarks, class of muon neutrinos, etc.)[5]. Single particles of a particle class (e.g. a single electron) are then identified with excitations of the quantum field.

Starting from a ground state $|0\rangle$ (the vacuum, common for all quantized fields associated to particle classes) a particle of some kind can be created by applying a creation operator or vice versa annihilated by applying an annihilation operator (assuming the presence of at least one particle). This is the same concept as known from the theory of the quantum mechanical harmonic oszillator (QMHO).

Now creation and annihilation operators for both particles and antiparticles with spin up and down are needed (fermions) :

- $a^s_{\vec{p}}$ annihilates particles of momentum $\vec{p}$ and spin orientation s (s $\in \{-1/2 + 1/2\}$)
- $a^{s\dagger}_{\vec{p}}$ creates particles of momentum $\vec{p}$ and spin orientation s
- $b^s_{\vec{p}}$ annihilates anti particles of momentum $\vec{p}$ and spin orientation s
- $b^{s\dagger}_{\vec{p}}$ creates anti particles of momentum $\vec{p}$ and spin orientation s

[5]Looking at Table 3.1 implies 16 particle classes. Together with the hypothetical Higgs boson (see below) there are 17 classes, resulting in 17 different quantum fields to be introduced.

A consistent behaviour of these operators is accomplished by demanding anti commutation relations[6] :

$$\{a^s_{\vec{p}}, a^{r\dagger}_{\vec{q}}\} = \{b^s_{\vec{p}}, b^{r\dagger}_{\vec{q}}\} = (2\pi)^3\delta^{(3)}(\vec{p}-\vec{q})\delta^{rs}$$

$$\{a,a\} = \{b,b\} = \{a,b\} = \{a^\dagger, a^\dagger\} = ... = 0 \quad \text{(all other possible combinations} = 0)$$

where the anticommutator is needed to ensure fermionic statistics.
This is different for the QMHO, where each state can aquire an arbitrary number of excitations (bosonic statistics due to commutation relations).

The gauge principle described in the preceding section is also viable for interacting quantum fields. The only thing that needs to be fixed is the presence of the classical fields.
In analogy to quantum mechanics where position q_i and momentum p_i $(i = 1, 2, 3)$ get promoted to operators $(\hat{q}_i, \hat{p}_i)$ which obey the fundamental commutation relations

$$[\hat{q_i}, \hat{p_j}] = i\delta_{ij}$$

$$[\hat{q_i}, \hat{q_j}] = 0 \quad ; \quad [\hat{p_i}, \hat{p_j}] = 0$$

the classical fields get promoted to operators obeying analogues (generalized to a continous fermionic system) commutation relations[7] :

$$\{\hat{\psi}_a(x), \hat{\psi}^\dagger_b(y)\} = \delta^{(3)}(\vec{x}-\vec{y})\delta_{ab}$$

$$\{\hat{\psi}_a(x), \hat{\psi}_b(y)\} = 0 \quad ; \quad \{\hat{\psi}^\dagger_a(x), \hat{\psi}^\dagger_b(y)\} = 0$$

where $a, b \,\epsilon\, \{1,2,3,4\}$ account for the different spinor components and all operators have to be considered at equal times $(x_0 = y_0)$.

The link between the concept of a quantized field with its creation and annihilation operators and the assumption of field operators ψ and $\hat{\psi}$, is that the field operators can be consistently expressed via a fourier integral in terms of creation and annihilation operators [22]:

$$\hat{\psi}(x) = \int \frac{d^3p}{(2\pi)^3}\frac{1}{\sqrt{2E_{\vec{p}}}}\sum_s (a^s_{\vec{p}}u^s(p)e^{-ipx} + b^{s\dagger}_{\vec{p}}v^s(p)e^{ipx})$$

$$\hat{\psi}^\dagger(x) = \int \frac{d^3p}{(2\pi)^3}\frac{1}{\sqrt{2E_{\vec{p}}}}\sum_s (b^s_{\vec{p}}v^{s\dagger}(p)e^{-ipx} + a^{s\dagger}_{\vec{p}}u^{s\dagger}(p)e^{ipx})$$

[6] {a,b}:=ab+ba
[7] Notice, that $i\psi^\dagger$ is the momentum conjugate of ψ

The aim of all this effort was to describe particle reactions including creation and annihilation of particles due to the equivalence of mass and energy ($E = mc^2$).
The modified interaction Lagrangian $\mathcal{L}_{int}$ (now containing field operators instead of classical fields) comprises all the information needed to calculate the evolution of a system of electromagnetically interacting fermions.

The standard procedure is to transform the Lagrangian into its associated Hamiltonian $\mathcal{H}_{int}$. The Hamiltonian , besides determining the energy structure, is responsible for the time evolution of the system.
Now it is not difficult to imagine how the interaction Hamiltonian, including creation and annihilation operators via the field operators, acts on some particle state $|\vec{p}_1\vec{p}_2...\vec{p}_n; s_1 s_2 ... s_n >$ manipulating the number of particles.

Calculating Cross sections

In particle reactions, the initial state is given by an (arbitrary) combination A of n particles heading onto each other. With some probability the final state consists of a combination B of m particles.
The experiment yields probabilities (cross sections, section 2.2.4) of final state configurations (usually starting from a fixed initial state configuration).

The things mentioned above (gauge principle, quantized fields and time evolution) culminate in the formulation of the S-Matrix [23] :

$$S = 1 + \sum_{n=1}^{\infty} \frac{i^n}{n!} \int d^4x_1 d^4x_2 ... d^4x_n T(\mathcal{H}_{int}(x_1)...\mathcal{H}_{int}(x_n)) \tag{3.1}$$

where T is the time-ordering operator.

Its crucial ingredient is the above mentioned interaction Hamiltonian $\mathcal{H}_{int}$, governing the evolution of a system of interacting particles.

Probabilities of particle reactions are now calculated in the following way : Let $|i\rangle$ be a state representing a configuration of (separated) incoming particles and $|o\rangle$ a state representing a configuration of (separated) outgoing particles. Then the probability P_{oi} of producing $|o\rangle$ when starting with $|i\rangle$ is given by the absolute square of the S-matrix element :

$$P_{oi} = |S_{oi}|^2 = |\langle o|S|i\rangle|^2$$

The cross section of a process is then basically calculated by integrating the S-matrix (the absolute square) over kinematically permitted final state configurations. The physics of the interaction is fully contained in the S-matrix element.

Generalized gauge principle

The concept of introducing the interaction into the free theory by demanding a certain

symmetry (U(1) in the case of electromagnetic interactions), can be generalized.
Consider a fermion n-plet

$$\Psi(x) := \begin{pmatrix} \psi_1(x) \\ \psi_2(x) \\ .. \\ \psi_n(x) \end{pmatrix}$$

and a non-abelian group G with a certain n-dimensional representation. Let $\{T_1, ..., T_l\}$ be the generators of G in the chosen representation and $\{\alpha_1(x), ..., \alpha_l(x)\}$ arbitrary functions of space and time.
Starting from the free theory an interaction Lagrangian is obtained by demanding an invariance under the substitution

$$\Psi(x) \rightarrow \exp(i \sum_{i=0}^{l} \alpha_i(x) T_i) \Psi(x)$$

This requires similar to the QED case the introduction of:

a) gauge fields, one for each generator of the group G, which then have to obey certain transformation rules

b) a suitable covariant derivative, replacing the common derivative

c) kinetic terms of the gauge fields

By means of this principle, a describtion of the electromagnetic, weak and strong interactions can be obtained (sections 3.2 and 3.3).

Feynman diagrams

S-matrix elements are calculated order by order (see Equation 3.1). Since these integral expressions are quite unintuitive, pictorial representations were introduced by Stueckelberg and Feynman. These representations are called Feynman diagrams.
For example, the lowest non-trivial order [8] matrix-element of Bhabha scattering ($e^- e^+ \rightarrow e^- e^+$) is represented[9] by the Feynman diagrams shown in Fig. 3.1.

Each part of these diagrams is associated with a mathematical expression, so that the complicated integral can be retrieved by applying some easy translation rules. The outer lines represent in- an outgoing particles, while inner lines indicate how the interaction of the incoming particles is propagated (here : via electromagnetic interaction (photon)).

[8] Lowest trivial order = no interaction, represented by the unity operator "1" in the S-matrix expression
[9] The actual matrix element is obtained by subtracting these contributions.

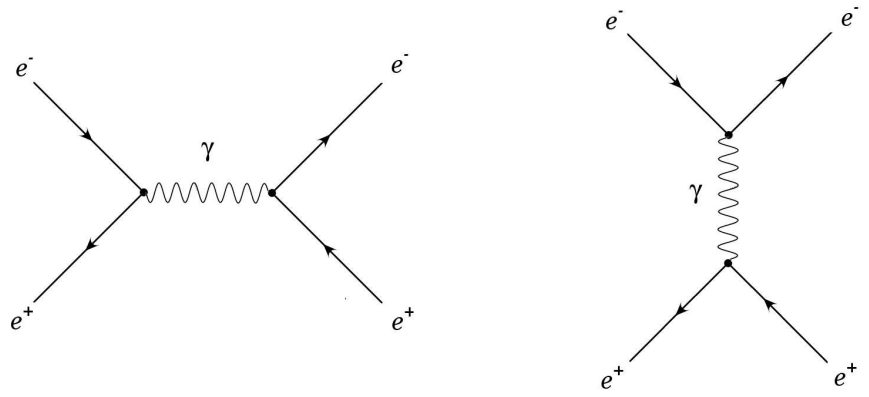

Figure 3.1: Lowest order Feynman diagrams for Bhabha scattering, $e^-e^+ \to e^-e^+$.

Each diagram is a combination of some fundamental pieces called fundamental vertices. In QED there is only one fundamental vertex :

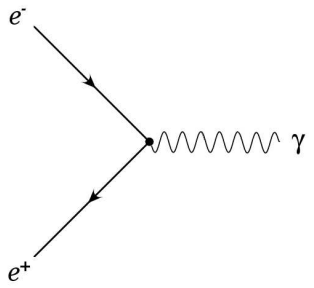

Figure 3.2: Fundamental QED vertex.

In QCD as a more complicated example, there are three:

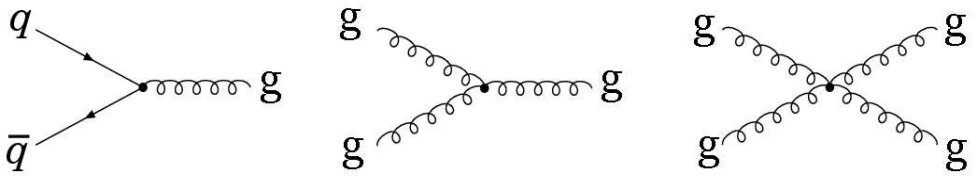

Figure 3.3: Fundamental QCD vertices. q refers to quarks, g to the gauge fields of QCD.

Fundamental vertices indicate which interactions and conversions actually appear.

Spontaneous symmetry breaking

Despite leading to a sensible theory of interactions of electrons and photons (QED) and quarks and gluons (QCD), gauge theories encounter some problems coming with interactions where the gauge fields ought to be associated with particles of non zero mass. This is the case with weak interactions. The demand of gauge symmetry forbids mass terms of the gauge fields. Thus conventional gauge fields cannot be associated with particles of non zero mass.

Therefore the concept of gauge theory is extended to gauge theories with "spontaneous symmetry breaking ".
This extention deals with a hypothetical field $\phi(x)$ (complex scalar field in the simplest case $\phi(x) = \phi_1(x) + i\phi_2(x)$, where $\phi_i(x)$ are real valued). It is additionaly put into the interaction Hamiltonian via a potential $V(\phi)$ of special shape.
This potential has to have the same global symmetry as demanded by the gauge principle, but has to have a ground state which must not exhibit this symmetry (Fig. 3.4).

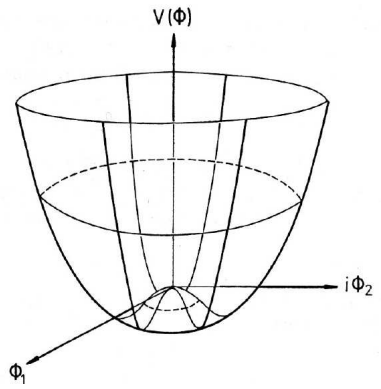

Figure 3.4: Example for U(1) symmetric potential with non U(1) symmetric ground states [24].

Expanding this field around a chosen groundstate (to do so, one has to choose a special groundstate out of a continuous space of equivalent ground states ("spontaneous symmetry breaking")) and including couplings of $\phi(x)$ with other fields by extending the covariant derivative, leads to the desired mass terms of the previously introduced gauge fields.

In addition to that a massive field $h(x)$ remains [10], the so-called Higgs field. Its existence as a real physical field, i.e. as a measurable particle, is not yet proved.

Renormalisation

The complicated but necessary procedure of renormalisation, where diverging S-matrix integrals are regulated, was omitted completely. An introduction can be found in [22].

[10] A remnant of the ground state expansion

3.2 QCD

Strong interaction of quarks[11] are described by the gauge theory of strong interaction, Quantum Chromo Dynamics (QCD).

To obtain the interaction Lagrangian consider again the free theory :

$$(i\partial^\mu\gamma_\mu - m)\Psi = 0 \quad ; \quad \mathcal{L} = \bar{\Psi}(i\partial^\mu\gamma_\mu - m)\Psi$$

where

$$\Psi(x) := \psi(x) \otimes \eta_c$$

where $\psi(x)$ is a common Dirac-spinor and η_c is an element of a vectorspace associated to a 3-dimensional representation of $SU(3)$, called "color-spinor".

This tensor product is adequate for describing quark states on this level (interaction + quantization of fields needed later on). The "color part" of the quark state refers to a new feature of quarks as fermions, namely having a new charge, called color. There are three different modulations of the color charge : red, blue and green. One may choose a basis of 3 orthogonal vectors in the color part of the quark state, each one representing one of the color charges.

In QCD the demanded invariance (symmetry) is governed by the non abelian group $SU(3)$, acting on the color part η_c of the quark state $\Psi(x)$.

Explicitly : The interaction Lagrangian (to be constructed) has to be invariant when replacing

$$\Psi(x) \to \exp(i\sum_{i=0}^{8}\alpha_i(x)T_i)\Psi(x)$$

where $\{T_1, ..., T_8\}$ are the 8 generators[12] of $SU(3)$ obeing $[T_i, T_j] = f_{ijk}T_k$, where f_{ijk} are the structure constants of $SU(3)$ and $\{\alpha_1(x), ..., \alpha_8(x)\}$ are again arbitrary functions of space and time.

To fulfill this, 8 gauge fields G_i have to be introduced. With the definition of the generalized field tensor:

$$F_i^{\mu\nu} := \partial^\mu G_i^\nu - \partial^\nu G_i^\mu - g_s\sum_{k,l=1}^{8} f_{ikl}G_k^\mu G_l^\nu$$

(where g_s is the "coupling constant" (see next section) of strong interactions, similar to the electric charge e for electromagnetic interactions) and a suitable covariant derivative :

[11] This interaction is dominant at hadron colliders.
[12] In some 3-dimensional representation

$$D^\mu = \partial^\mu + i\frac{g_s}{2}\sum_{i=1}^{8} T_i G_i^\mu$$

the desired interaction Lagrangian is obtained :

$$\mathcal{L}_{int,QCD} = \bar{\Psi}(iD^\mu\gamma_\mu - m)\Psi - \frac{1}{4}F_{i,\mu\nu}F_i^{\mu\nu}$$

Fundamental vertices are shown in Fig. 3.3. The second and third one represent the self-interaction of the gauge fields[13]. This new feature (not present in QED) is due to the non abelian gauge group $SU(3)$. The non vanishing structure constants[14] f_{ikl} lead to additional couplings.
Leading order feynman diagrams of QCD processes are shown in figures 3.5 and 3.6.

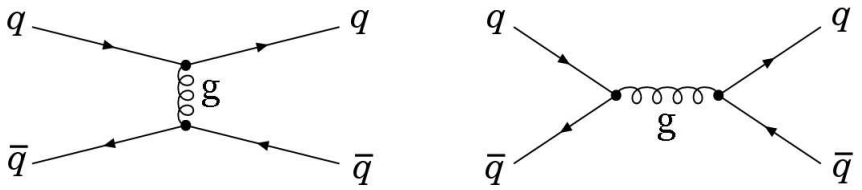

Figure 3.5: Leading order feynman diagrams of the process $q\bar{q} \to q\bar{q}$.

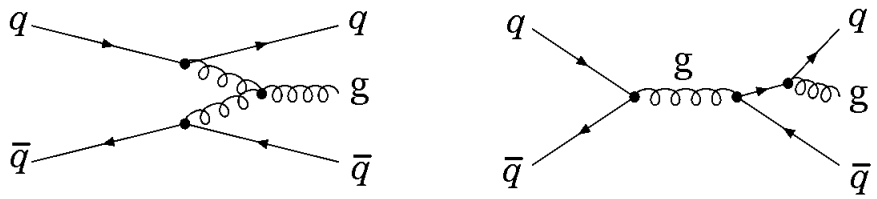

Figure 3.6: Leading order feynman diagrams of the process $q\bar{q} \to q\bar{q}g$.

Asymptotic freedom

Each interaction (electromagnetic, weak, strong and gravitational) is characterized by a coupling α, describing the strength of the interaction. In the case of the strong interaction it is defined by :

$$\alpha_S := \frac{g_S^2}{4\pi}$$

[13]Certain linear combinations of the gauge fields are identified with the actual gluons
[14]In abelian (gauge) groups they are all zero.

in the case of electromagnetic interactions :

$$\alpha_{em} := \frac{e^2}{4\pi}$$

where e is the elementary charge.

The coupling constants and the coupling α itself are dependent on the momentum transfer Q^2 of the particle reaction and their behavior is strongly related to the gauge group of the interaction.

Non abelian gauge groups yield a vanishing coupling ($\alpha(Q^2) \to 0$) for huge momentum transfers ($Q^2 \to \infty$). Particles propagate as if they were free. This is called asymptotic freedom. The opposite hold for abelian gauge groups.

The coupling also decides whether or not perturbation theory[15] is applicable. Each vertex (number of vertices $\propto$ order of expansion) yields a factor $\sqrt{\alpha}$. Thus the convergence of the S-matrix element is directly coupled to this quantity.

QCD as a non-abelian gauge theory exhibits asymptotic freedom, scattering processes can be calculated perturbatively for large momentum transfers.

The coupling of the strong interaction $\alpha_S(Q^2)$ can be parametrized as follows (to lowest order) [24] :

$$\alpha_S(Q^2) = \frac{4\pi}{7\ \ln(Q^2/\Lambda^2)}$$

where it is assumed, that the number of quark flavors equals 6. Λ is a scale parameter which was measured to lie within 100 and 500 MeV. The decline of $\alpha_S(Q^2)$ is shown in Fig. 3.7.

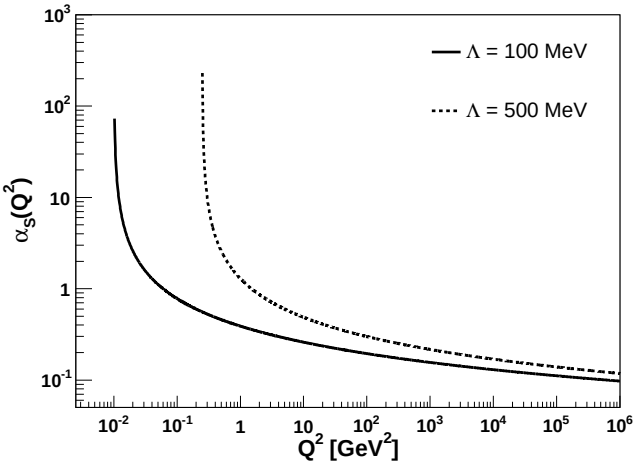

Figure 3.7: Variation of strong coupling $\alpha_S(Q^2)$ for scale parameters $\Lambda = 100$ MeV and $\Lambda = 500$ MeV.

[15] Calculation of cross sections via S-matrix elements.

Confinement

Confinement, describes the fact, that color charged particles (quarks and gluons) cannot be observed as isolated particles. Each attempt to do so has failed. However they can be combined, to constitute a colorless particle, like for instance the proton, which consists of a colorless net combination of two u- and one d-quark.
This is behavior is due to the nature of the strong force. It does not strive to zero when separating partons of a colorless net combination (Fig. 3.8). It rather stays constant. Thus the energy of the force field could grow beyond every barrier unlike what we know (for example) from gravity, where the force field between two masses can aquire only a finite amount of energy, even when the masses are seperated infinitely.
Thus, after reaching a sufficiently great distance, the energy of the force field is sufficient to produce pairs of particles.

If the produced particles have the suitable color-charges, each of the initial particles

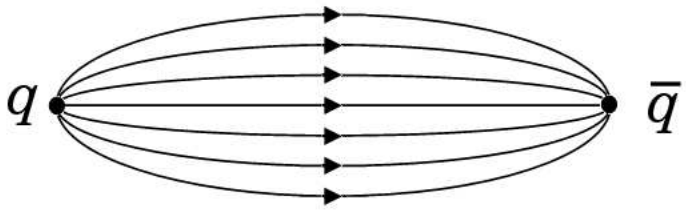

Figure 3.8: Shape of strong force field between quarks constituting a meson (colorless). The potential grows $\propto r$ for a sufficiently large distance r. Once the contained energy is large enough, quark-antiquark pairs can be created.

can merge with one of the produced ones and form a colorless particle, which then can be detected as an isolated particle. This process is called fragmentation or hadronisation (see also section 3.4).

3.3 Electroweak Theory

The electroweak theory is a $SU(2) \times U(1)$ gauge theory [16]. It unifies weak and electromagnetic interactions. States are of the kind :

$$\Psi(x) = (\psi_L(x) \otimes \eta_I, \psi_R(x))$$

where $\psi_L(x)$ and $\psi_R(x)$ are Dirac spinors stemmimg from the subspaces of left- and right-handed states[17], respectively.

This distinction is due to the fact, that just the left-handed components take part in weak interactions. The right handed-components are not affected or do not even exist (neutrinos).

[16] This is a non abelian gauge group (due to $SU(2)$ component).
[17] Being eigenstates of the chirality γ^5 with eigenvalue +1 and -1 , respectively.

This is different for the electromagnetic part of the electroweak interaction, therefore the right-handed part is present in the second component of the state $\Psi(x)$.

η_I is an element of a vectorspace associated to a 2 dimensional representation of $SU(2)$, called isospin spinor. The left-handed parts of associated weakly interacting particles [18] are arranged in isospin dublets. Let $\{v_1, v_2\}$ be a basis of that 2-dimensional space, then $\eta_I = (1,0)$ represents the first one and $\eta_I = (0,1)$ the second one of the associated particles.

Demanding local $SU(2) \times U(1)$ symmetry, when starting from the free theory, requires the introduction of three gauge fields W_1, W_2 and W_3 due to the $SU(2)$-part and one gauge field B due to the $U(1)$-part of the gauge group.

The covariant derivative is now :

$$\mathbf{D}^\mu = (\partial^\mu + i\frac{g}{2}\sum_{i=1}^{3}(T_i W_i)^\mu + i\frac{g'}{2}B^\mu \ , \ \partial^\mu - ig'B^\mu)$$

where the T_i are the three generators of $SU(2)$ in some 2 dimensional representation and g, g' are the coupling constants[19].

The gauge fields W_1, W_2 ,W_3 and B are not directly associated with particles. Like in QCD one has to form certain linear combinations, listed in Table 3.2, where

$$\sin(\theta_w) := \frac{g'}{\sqrt{g^2 + g'^2}} \quad , \quad \cos(\theta_w) := \frac{g}{\sqrt{g^2 + g'^2}}$$

θ_w is called the weak mixing angle. It is a parameter of the theory and has to be determined from experiments. Its connection with the masses of Z and W boson via

$$m_W = m_Z \cos(\Theta_w)$$

yields a value of $\Theta_w \simeq 28.7°$.

The measured elementary charge e is connected with the coupling constants and the weak mixing angle via

$$e = g'\cos(\theta_w) = g \sin(\theta_w)$$

Since the W^+, W^- and Z boson are massive particles, the concept of spontaneous symmetry breaking, like explained in section 3.1 has to be applied. This yields the desired mass terms for the gauge fields.

[18] Associated are : $(\nu_e, e), (\nu_\mu, \mu), (\nu_\tau, \tau), (u, d'), (c, s')$ and (t, b') where d', s', b' are linear combinations of d, s, b. See this section.

[19] g due to the $SU(2)$ and g' due to the $U(1)$ part of the interaction. They are not independent of each other.

particle	associated field
Photon	$A^\mu := B^\mu \cos(\theta_w) + W_3^\mu \sin(\theta_w)$
Z boson	$Z^\mu := -B^\mu \sin(\theta_w) + W_3^\mu \cos(\theta_w)$
W^+ boson	$W^{(+)\mu} := \frac{1}{\sqrt{2}} (W_1^\mu + iW_2^\mu)$
W^- boson	$W^{(-)\mu} := \frac{1}{\sqrt{2}} (W_1^\mu - iW_2^\mu)$

Table 3.2: Particles and associated gauge field combinations in the electroweak theory.

The interaction Lagrangian is not be stated here, it is quite complex and requires more detailed explanations (it can be found in [21]). Instead the fundamental vertices are given (Fig. 3.9-Fig. 3.12) (vertices including the higgs field were omitted).

Due to the non abelian gauge group, self interactions of the gauge fields similar to the QCD case are obtained (Fig. 3.11 and Fig. 3.12).

Quark Flavor Mixing

An important feature of weak interactions is called flavor mixing. A u-quark can transform into a d-quark via emitting a W-boson.

Contrary : Strong and electromagnetic interactions are stricly flavor conserving, the emission of a gluon or photon never changes the quark flavor.

The mixing is summarized in the complex valued CKM-matrix :

$$V_{CKM} = \begin{pmatrix} V_{ud} & V_{us} & V_{ub} \\ V_{cd} & V_{cs} & V_{cb} \\ V_{td} & V_{ts} & V_{tb} \end{pmatrix}$$

where $|V_{ud}|$ is the probability of switching a u-quark into a d-quark via W-boson emission and so on. The measured mean values are[20]:

$$\begin{pmatrix} |V_{ud}| & |V_{us}| & |V_{ub}| \\ |V_{cd}| & |V_{cs}| & |V_{cb}| \\ |V_{td}| & |V_{ts}| & |V_{tb}| \end{pmatrix} = \begin{pmatrix} 0.9745 & 0.224 & 0.0037 \\ 0.224 & 0.9737 & 0.042 \\ 0.0094 & 0.04 & 0.9991 \end{pmatrix}$$

Because of this, quark states[21] , like defined in section 3.2 are not eigenstates of the electroweak interaction.

Eigenstates are found by applying a relative rotation via the CKM-matrix in flavor space, affecting d, s and b quark states (following common conventions). These states are marked by a dash (d', s', b').

$$\begin{pmatrix} d' \\ s' \\ b' \end{pmatrix} = V_{CKM} \begin{pmatrix} d \\ s \\ b \end{pmatrix}$$

[20] Taken from [21].

[21] Quark states defined in QCD are eigenstates of mass and flavor, respectively.

Leading order Feynman diagrams of electroweak processes can be found in section 5.2.2.

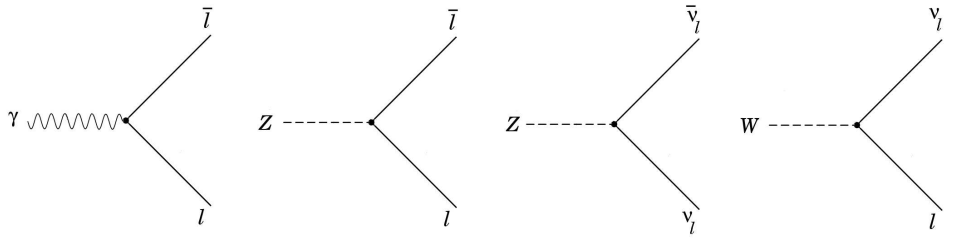

Figure 3.9: Lepton-boson vertices. l denotes either e, μ or τ.

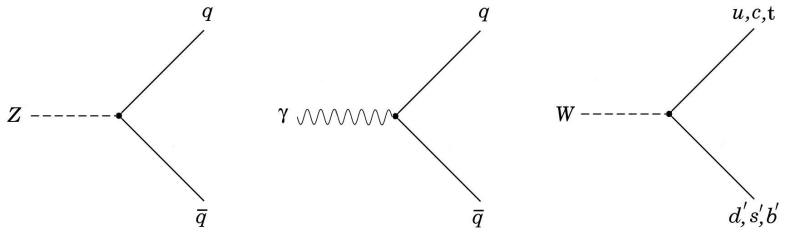

Figure 3.10: Quark-boson vertices.

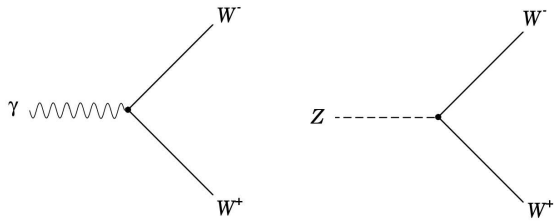

Figure 3.11: Self interaction of gauge bosons via 3-boson-vertices.

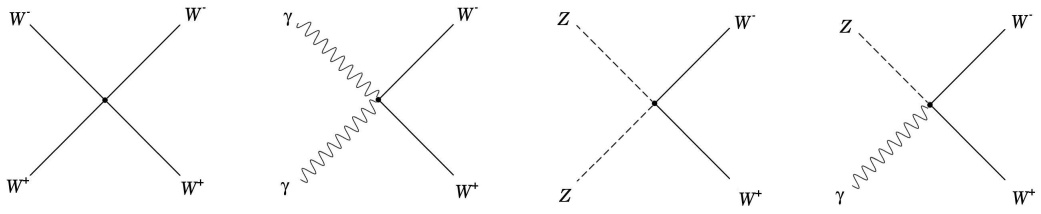

Figure 3.12: Self interaction of gauge bosons via 4-boson-vertices.

3.4 Mono-jets in the Standard Model and from Beyond

Jets (section 4.1) are detector representations of partons (quarks and gluons). The notion mono-jet labels an event topology with exactly one jet and nothing else (to be concretized in section 5.1). Here "nothing else" means nothing else from the detector point of view. From the physics point of view, this comprises the creation of undetectable particles (with respect to the detector used). Thus any particle reaction with a final state consisting out of one parton and undetectable particles (whatever they may be) yields the mono-jet topology. This circumstance makes the mono-jet channel attractive for testing numerous theories predicting reactions with final state partons and new (yet undetected) particles. A final state with one parton and undetectable particles is referred to as "mono-jet final state " in the following.
On a general basis mono-jet final states may be produced by the virtue of two simple prototype vertices sketched in Fig. 3.13. On the left, X (could be any Standard Model particle)

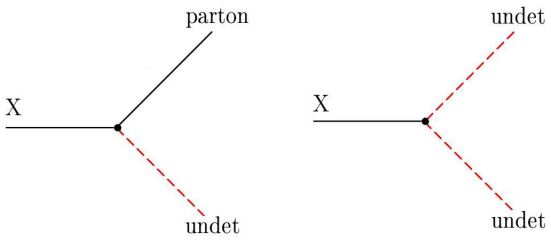

Figure 3.13: Sketches of prototype vertices for mono-jet production.

transforms into a parton and an undetectable particle. On the right, X transforms into two undetectable particles.
Examples how these vertices may be used to build processes exhibiting the desired mono-jet final state are shown in Fig. 3.14.
The only Standard Model particles which cannot be detected by the used DØ detector are

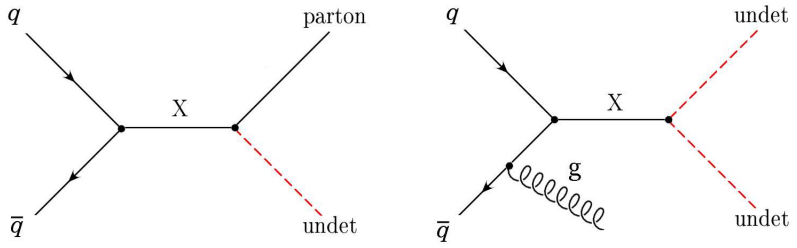

Figure 3.14: Sketches of possible processes with mono-jet signature.

neutrinos. While the left vertex of Fig. 3.13 is not realizable (there is no vertex containing neutrinos and partons at once, this would violate either lepton or baryon number conservation), there exists a realization of the right one (Fig. 3.15).
However in a real experiment things are not this straight. Since mono-jet events have to be defined from the detector point of view, one has to deal with additional Standard Model sources. For example, due to detector inefficiencies particles may not be recognized as such and thus processes with non mono-jet final states may contribute as well. Fig. 5.3

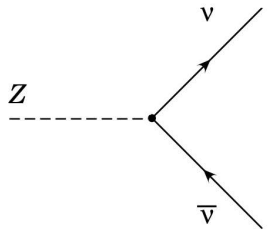

Figure 3.15: Realization of prototype vertex for mono-jet prodution in the SM.

shows some non mono-jet final state processes[22] expected to contribute to the mono-jet class. Other sources are considered in section 5.

In the following two non Standard Model sources of mono-jet events are discussed.

Mono-jets from Large Extra Dimensions

Like mentioned before, the Standard Model does not comprise gravitational interactions. Besides technical problems in modelling a quantized field theory of gravitation, the more convincing reason for that is the strength of the gravitational interaction when masses/energies of involved objects are small (m$\ll m_p$[23]).

Energies achieved by today's scattering experiments are in the TeV (10^3 GeV) range, thus the influence of gravitional interaction is assumed to be negligible[24].

In high energy particle collisions, particles approach each other to distances of about 10^{-18} m. The behavior of gravity hasn't been independently tested on such scales. Actually it hasn't been tested at distances smaller than 0.1 mm [26] yet. Thus a deviation of its strength at small distances is not excluded and could be of relevance to particle reactions probed in today's scattering experiments.

A proposal of enhanced gravity dealing with extra spatial dimensions was given by Nima Arkani-Hamed, Savas Dimopoulos and Gia Dvali [25][26]. The idea behind this is as follows :

In addition to the common three spatial dimensions at least one extra finite dimension (flat of radius R in the simplest case, Fig. 3.16 left) is assumed.
The actual graviton is able to propagate in all spatial dimensions. Due to the finiteness of R the momentum with respect to the extra dimension is quantized :

$$p_4 = \frac{n}{R} \quad , \quad n \in Z$$

These momentum states (of the actual graviton) are interpreted as massive excitations of the common graviton (Newtonian gravity) with masses

$$m = |p_4|$$

[22] In the Standard Model.
[23] Planck mass $m_p := \sqrt{\frac{1}{G}} \simeq 1.2 \cdot 10^{10}\ GeV$ where G is the gravitational constant from Newton's law.
[24] This assumption originates from the basic knowledge of gravity, i.e. Newton's law.

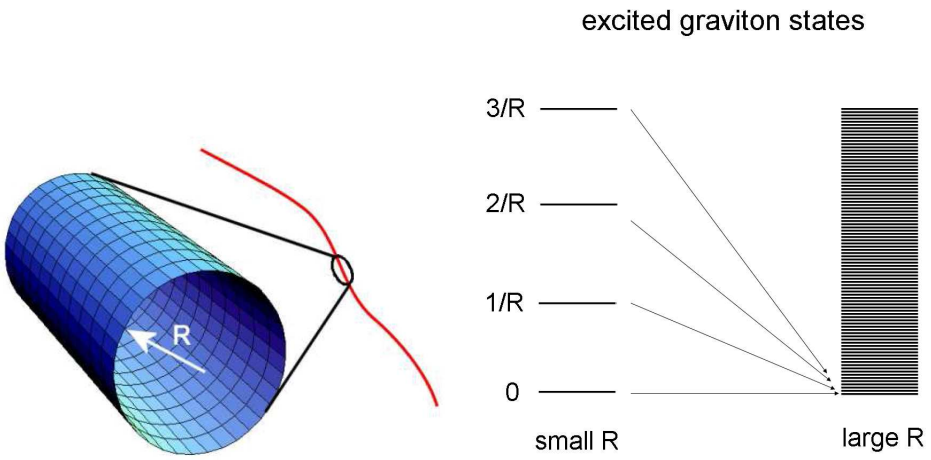

Figure 3.16: Left : Flat extra spatial dimension with radius R [53]. Right : The spacing of excited graviton states depends on the radius R of the extra spatial dimension. The larger R the more states are accessible (given an energy E at disposal).

Excited states are referred to as Kaluza-Klein (KK) gravitons. The "0-mode" ($p_4 = 0$) is identified with the common graviton.

Each of these states contributes ($\propto \frac{1}{m_p^2}$) to the propagation of gravity, enhancing phase space by a factor $\propto ER$, where E is the energy at disposal.
The same works for d extra spatial dimensions of radius R, yielding an additional factor

$$\propto (ER)^d$$

and a strength

$$\propto (ER)^d \frac{1}{m_p^2}$$

If the factor is sufficiently large (this depends on the radius R of the extra dimensions) gravity may play a role even in today's collider experiments.

The enhancement vanishes if distances $r \gg R$ are approached. The gravitational flux lines can not continue to penetrate in the extra dimension and the field thins out, the common $\frac{1}{r}$ dependency is obtained again [25].

An effective field theory including Standard Model particles and enhanced gravitation (from large extra dimensions) was proposed in [27]. It also includes direct KK graviton production with mono-jet final states (where the KK-graviton is assumed to be the undetectable particle). Effective Feynman diagrams of mono-jet final state processes are shown in Fig. 3.17.

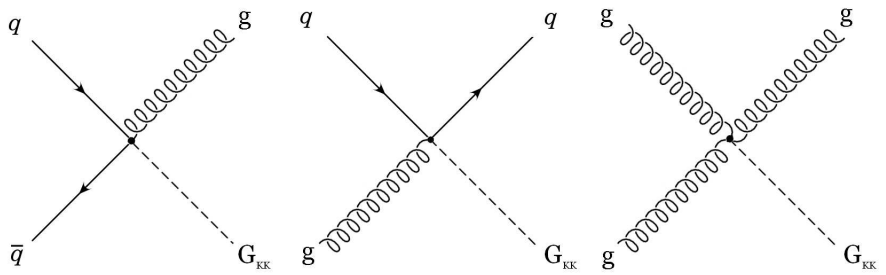

Figure 3.17: Effective Feynman diagrams for direct KK-graviton production according to [27].

Mono-jets from Supersymmetry

Supersymmetry is an extension of the Standard Model assuming that each of the particles listed in Table 3.1 (+ anti particles) has a supersymmetric partner. More precisely : each fermion gets a bosonic and each boson gets a fermionic partner. Explanations of the motivations of this assumption can be found in [54].

The lightest predicted supersymmetric particle, the neutralino[25] $\tilde{\chi}_1^0$, is stable under the assumption of R-parity conservation. R-parity is a multiplicative quantum number defined by

$$R := (-1)^{3B+L+2S}$$

where B : baryon number[26], L : lepton number[27] and S : spin. R equals 1 for Standard Model and -1 for supersymmetric particles.

The lightest supersymmetric particle would be forced to decay into Standard Model particles[28]. However, under the assumption of R-parity conservation this decay channel is forbidden, thus the neutralino would be stable.

Since no direct evidence of such a particle has been found yet, it is expected to traverse the DØ detector without detection.

The Supersymmetry vertex shown in Fig. 3.18 includes neutralinos and a Standard Model Z boson. This vertex is a realization of the second prototyp vertex shown in Fig. 3.13 and thus yields mono-jet final states. Like in the case of the Standard Model also non mono-jet final states in Supersymmetry may contribute to the class of mono-jets. A prcocess worth mentioning is shown in Fig. 3.19. It may contribute to a large extent due to the favored strong coupling.

[25] A linear combination of the fermionic partners of the neutral Standard Model gauge bosons

[26] B= $\frac{1}{3}$ for quarks and B= $-\frac{1}{3}$ for antiquarks. The same holds for their supersymmetric partners (squarks). B=0 for all other Standard Model particles and their supersymmetric partners (Table 3.1).

[27] L=1 for lepton and L=-1 for antileptons. The same holds for their supersymmetric partners (sleptons). L=0 for all other Standard Model particles and their supersymmetric partners.

[28] Assuming that no other unknown particles do exist.

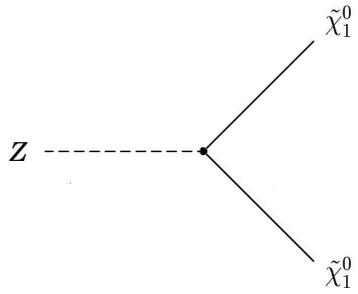

Figure 3.18: Weak coupling of Z boson and neutralino in Supersymmetry.

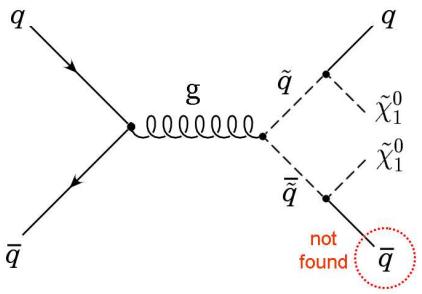

Figure 3.19: Supersymmetry mono-jet background process. $\tilde{q}$ are the supersymmetric partners of quarks called squarks. This process contributes to the mono-jet channel in case one of the final quarks gets not detected properly. See section 5.5 for further explanations on background sources.

3.5 Event Generators and Detector simulation

In section 2 the experimental setup and the actual output of the detector was described. In this section basics of particle theory were reviewed, indicating how cross sections of elementary particle reactions are calculated.
Since proton and antiproton are not elementary particles and particle theory does not provide detector signals, these outputs seem to be incomparable. The gap has to be filled, otherwise no conlusion about the validity of the theory can be drawn.

This task is devided into two steps. The first step is done by event generators, the second one by detector simulations.

1. Event generators :

Things an event generator accounts for (further details can be found in [33]) :

a) choice of constituents of proton and antiproton (i.e. quarks and gluons) entering the hard scattering process and assignment of some fraction of the total proton/antiproton momentum (980GeV)

- The structure of the proton was determined in inelastic electron proton scattering experiments. These results are implemented via parton distribution functions. These distribution functions yield the probability that parton i takes part in the

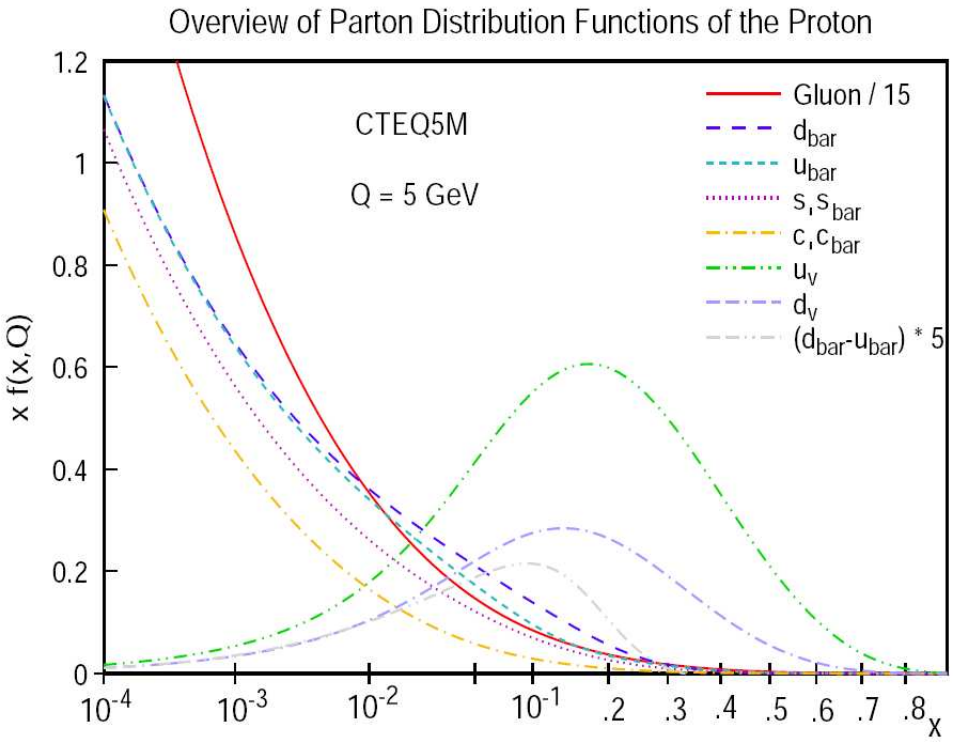

Figure 3.20: Parametrizations of parton distribution functions inside proton [32]. In addition to the valence-quarks (uud), virtual pairs of light quarks (u,d,c and s) and gluons contribute to the structure of the proton. The net number ($\int_0^1 (f_q(x) - f_{\bar{q}}(x))dx$) of the various quarks has to be : 2 for u-quarks, 1 for d-quarks and 0 for c- and s-quarks.

hard scattering and carries a fraction x of the total momentum, dependent on the total momentum transfer Q^2 of the particle reaction. Parametrizations of these functions are shown in Fig. 3.20.

b) cross sections of elementary particle interactions

- particle theory like described in the preceding sections provides the framework of how to calculate cross sections of particle interactions. Like mentioned before S-matrix elements are calculated order by order. These calculations get more and more extensive and most of them are not yet done. Therefore many processes are only implemented in leading order (LO). Some corrections are implemented though. For example corrections of the bremsstrahlungs-type, where an initial or final state quark emits one or more gluons and photons (photon emission holds for any charged final state particle as well). This correction is independent of how the actual process looks like, and hence can be implemented in a global manner.

c) hadronization of final state partons into colorless hadrons, photons and leptons

- To account for that, certain hadronization models are implemented (presently there exists no calculation from first principles (including the QCD Lagrangian), yielding a sensible description of hadronization). The most common one is the Lund string model. Its principle is sketched in Fig. 3.21 (see also section 3.2 "Confinement")

d) decay of unstable hadrons

- As far as the decay products and branching ratios are known, they are implemented (problems→[33]).

e) statistical fluctuations due to the probabilistic nature of quantum mechanics

- This problem is tackled with Monte Carlo techniques. An introduction can be found in [36]

Event generators used in this analysis are Pythia [33] and Alpgen [62].

2. Detector simulation :

The output of the event generator are leptons, photons and hadrons with assigned energy and direction.
In this second step, the interaction of these particles with the detector is simulated. The GEANT based program d0gstar [34] simulates magnetic fields, track curvature and shower evolution corresponding to the actual design of the detector (Fig. 3.22).
Thereafter the program D0sim [35] turns energy depositions of affected components into electrical signals. It also adds :

- minimum bias events
- calorimeter pileup from previous events
- calorimeter noise
- SMT / CFT noise and inefficiencies
- muon noise and inefficiencies

This output is provided in the same data format as the real detector output. From now on real and simulated data can be treated on equal footing (cp. Fig. 3.23).

In the next chapter it is explained how information about the initial particle interaction is retrieved from the detector and simultion output.

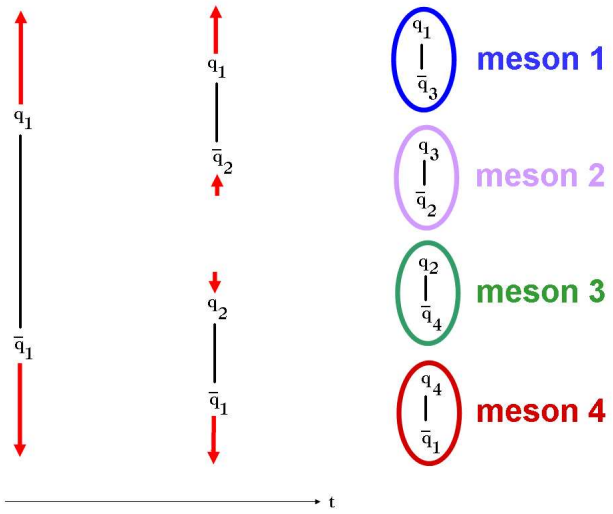

Figure 3.21: Principle of Lund String Model in the simplest case. Black lines indicate a string, representing the force field of strong interactions. Red arrows indicate excessive kinetic energy with respect to bound state. Once the force field owns sufficient energy, a pair of quark and antiquark is produced. If all the excessive kinetic energy is transformed, colorless combinations of quarks remain (here : mesons).

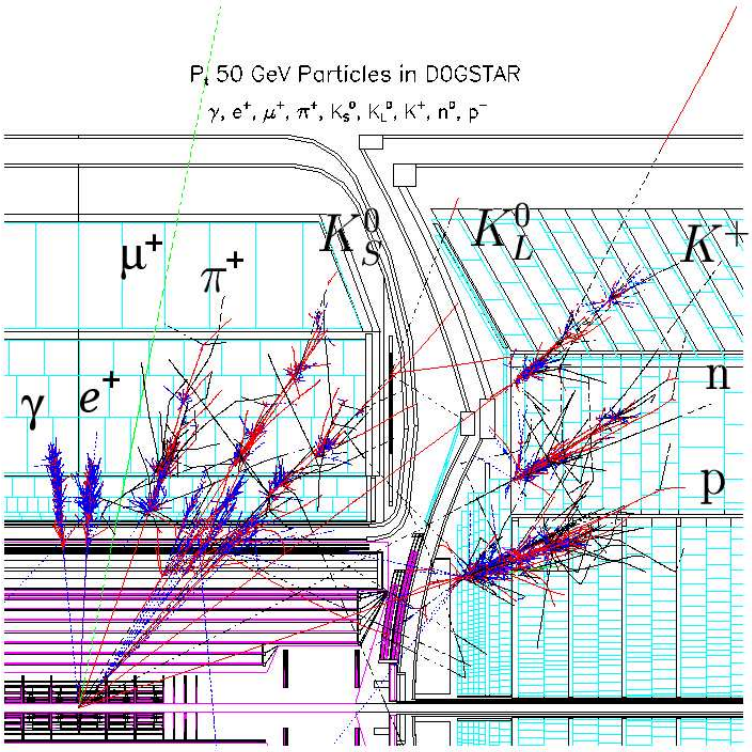

Figure 3.22: Simulation of interaction between particles and detector components with D0gstar [59].

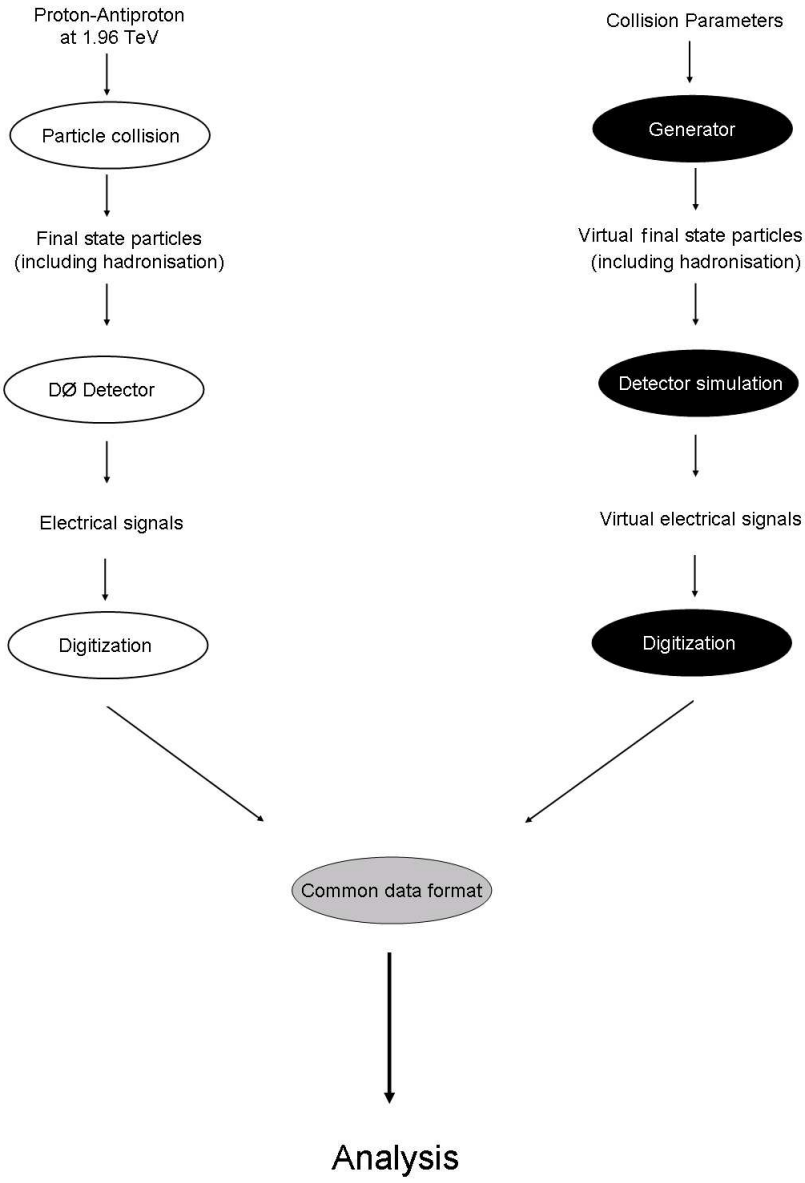

Figure 3.23: Summary of steps towards comparability of theoretical and experimental outputs.

Chapter 4

Object Identification/Reconstruction

Like taking a picture of some object, where the picture does not contain the original object itself, but rather information about it, a detector like DØ takes a picture of a particle scattering event. Such a picture may look like the one shown in Fig. 4.1 (an explanation of the event display is given in appendix A.2).

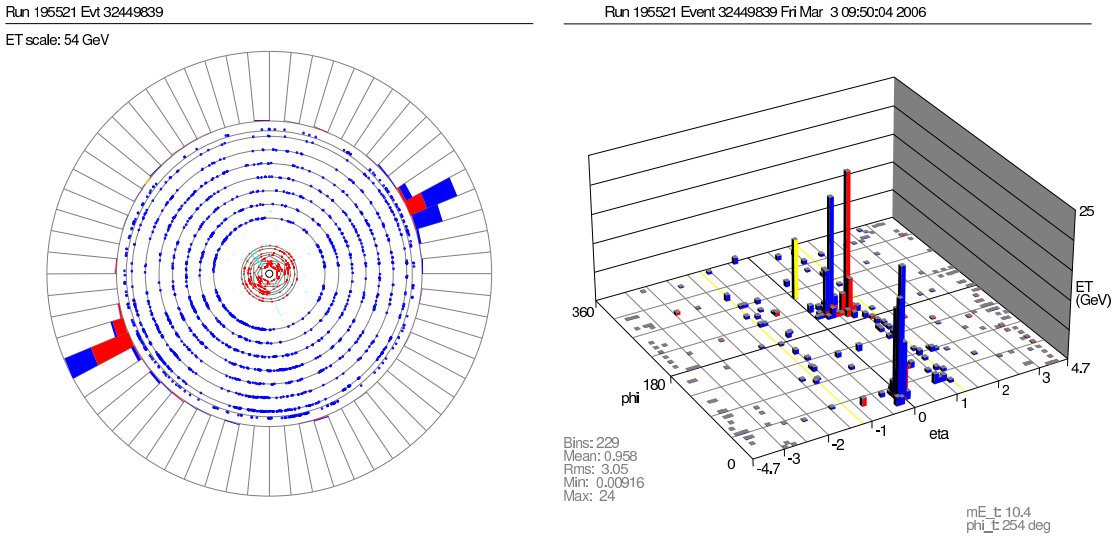

Figure 4.1: Graphical illustration of detector output. Left : $r - \phi$ view. Blue points indicate CFT, red point SMT hits. Energy depositions are indicated by red (eletromagnetic calorimeter) and blue (hadronic calorimeter) bars. Right : $\eta - \phi$ Lego Plot (calorimeter information only). Again, bars indicate energy depositions.

The obtained information basically consists of values of energy depositions in the calorimeter and of time and position of single hits in the tracking system (Fig. 4.1). From that, the original particle process has to be reconstructed.
The design of the detector was chosen due to the distinguishing characteristics of different particles (section 2). Therefore it possible to separate signals of different particles to reasonable extent.

The next sections will cover the identification methods of partons, muons, electrons and photons and is concluded by comments on the calculation of the missing transverse energy (MET).

4.1 Partons

Partons as color charged particles cannot exist as free particles. The hadronization process turns them into a bunch of colorless hadrons moving roughly into the same direction. These particles (or their decay products) actually interact with the detector material.

The charged fraction (if present) of contained particles leaves signals in the tracking system, while almost all contained particles (charged and uncharged) interact with the calorimeter material. This is the reason why partons are originally identified via the calorimeter system.

Due to this behavior it is expected that a parton leaves a focussed energy deposition in the calorimeter (possibly with attached tracks).

To identify this signature a search algorithm is needed. The algorithm used in this analysis is the "Run II Cone Algorithm", formerly known as "Improved Legacy Cone Algorithm (ILCA)". It exclusively searches the calorimeter output. Its output are **calorimeter-jets**.

4.1.1 Cone Algorithm

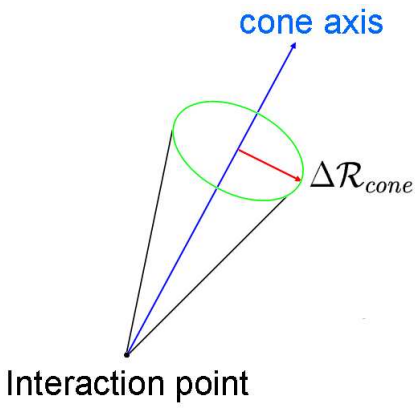

Figure 4.2: Sketch of cone, used to scan energy depositions in the calorimeter.

The utilized cone algorithm pursues a simple strategy : It starts with a cone of some radius[1] $\Delta\mathcal{R}_{cone}$ and an axis defined by the interaction point and a seed (Fig. 4.2). The seed may be a calorimeter tower exceeding some energy threshold[2]. Now the energy weighted centroid of all energy depositions inside the cone is calculated (Fig. 4.3). While the origin

[1] In (η, ϕ)-space. The definition of distance in (η, ϕ)-space is given in appendix A.1.

[2] Actually, due to computing time restrictions it was decided to form clusters ("preclusters") of adjacent towers inside a cone of radius $\Delta\mathcal{R} = 0.3$ around a tower exceeding an E_t threshold of 0.5 GeV and the total E_t inside the 0.3-cone exceeding 1 GeV, to serve as seeds. This reduces the number of possible seeds of about one order of magnitude.

of the cone stays fixed, the centroid is used to define a new cone axis. With respect to this new cone, the energy weighted centroid is calculated again. This is done until the cone axis reaches a "stable position" (i.e. its fluctuation is below some threshold).

Stable cones are called proto-jets . Also midpoints of proto-jets are used as seeds[3], if their distance lies within $[\Delta\mathcal{R}_{cone}, 2 \cdot \Delta\mathcal{R}_{cone}]$. Stable cones found with respect to these midpoints, also enter the list of proto-jets.

Overlapping proto-jets are either merged or split. If the fraction of shared transverse energy is more than 50% of the transverse energy of the lower E_t proto-jet, both will be merged, otherwise the energy is individually assigned to the proto-jet that is closest in (η, ϕ)-space. After this the found objects are called calorimeter-jets[4].

- this analysis uses a cone radius of $\Delta\mathcal{R}_{cone} = 0.7$

Jets can be assigned a direction (direction of stable cone axis), an energy (by adding energy depositons inside the cone) and transverse momentum (by adding the transverse projections of energy depositions inside the cone).

The purpose of considering the cone algorithm was to identify final state partons. The simplest possibility would be to identify parton quantities with jet quantities. What holds for the direction, does not hold for energy and momentum. Several corrections summarized by the notion "Jet Energy Scale" are applied.

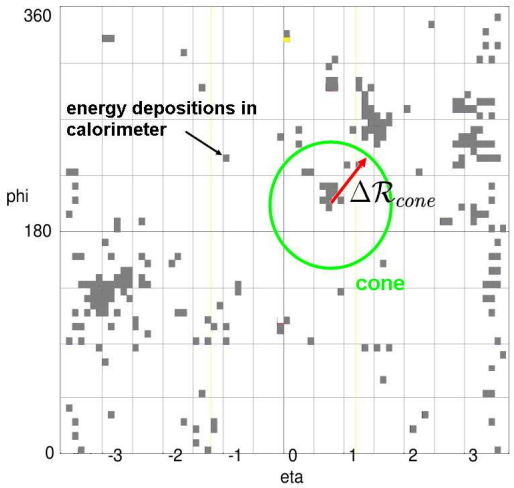

Figure 4.3: Shown are energy depositions in the calorimeter $((\eta, \phi)$-space). A grey square marks a calorimeter tower exceeding an energy threshold of 0.5 GeV. The search for stable cones ("proto-jets") is indicated.

[3]This is done to avoid sensitivity to soft radiation. Information on cone algorithms in general and their theoretical requirements (infrared safety, collinear safety, etc.) can be found in [28].

[4]More information can be found in [37].

4.1.2 Jet Energy Scale

The energy assigned to a jet like described above, is not yet the best approximation of the parton energy. Sources of error are :

- calorimeter noise (+)
- energy depositions outside the cone, stemming from the parton (–)
- different detector response in different regions (+/–)
- energy from underlying events, typically 0.8 underlying events per interaction (+)
- different response to different particles, due to fluctuations in the fragmentation process (–)

The (+) and (–) signs indicate if the effect enlarges or reduces the energy found in the cone with respect to the energy of the parton.
The corrected energy is parametrized by :

$$E_{corrected} = \frac{E_{meas} - E_{offset}(\mathcal{R}, \eta, \mathcal{L})}{R_{calo}(\mathcal{R}, \eta, E_{meas}) F_{cone}(\mathcal{R}, \eta, E_{meas})} \tag{4.1}$$

where :

- E_{meas} : the energy found by just adding the energy inside the cone (no corrections applied)
- E_{offset} : accounting for the offset (+) due to calorimeter noise and underlying events
- R_{calo} : accounting for the different response of the calorimeter in different regions
- F_{cone} : accounting for the fraction of energy outside the cone
- $\mathcal{R}$: Radius of the cone ($\mathcal{R}$=0.7 in this analysis)
- η : (appendix A.1)
- $\mathcal{L}$: Luminosity

Values for the correction terms are determined with the aid of photon+jet events. The single photon recoils against the parton. Due to momentum conservation, the transverse energies of the photon and parton are equal. Since the measurement of the photon energy is more reliable,

a) electromagnetic showers are much more focussed than a hadronic shower, thus the out of cone showering is much smaller,

b) an electromagnetic shower is not affected by fragmentation fluctuations and

c) the electromagnetic calorimeter is much less affected by noise,

the reconstructed photon energy can be used to calibrate the energy found by the cone algorithm. This yields the correction factor. The jet energy correction versus p_t and versus η and the error bands are shown in Fig. 4.4.

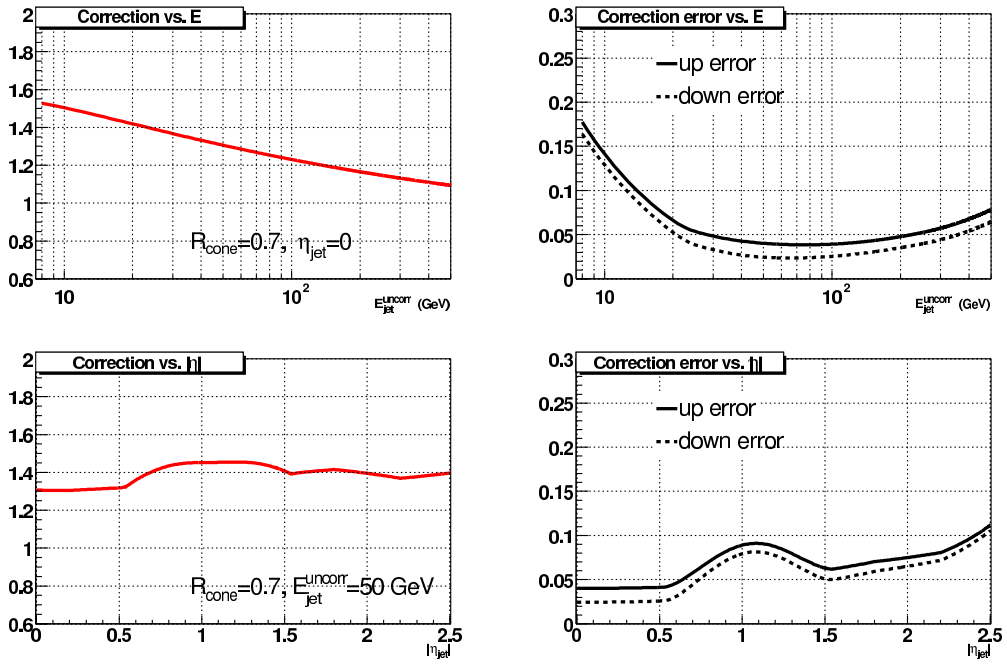

Figure 4.4: JES correction vs uncorrected jet-energy and vs $|\eta_{jet}|$ for data, taken from [56]

4.1.3 Selection Criteria

Jets found by the "Run II Cone Algorithm" do not necessarily originate from a parton ("parton-jet"). They may as well originate from other particles, which cause similar energy depositions or noise ("noise-jets"). To filter jets caused by partons from those caused by other particles or noise effects, additional criteria are demanded :

- electromagnetic fraction (emf) :

$$0.05 < emf := \frac{E_{ECAL,cone}}{E_{CAL,cone}} < 0.95$$

where $E_{ECAL,cone}$ is the fraction of uncorrected jet energy inside the jet cone found in the electromagnetic calorimeter and $E_{CAL,cone}$ is the total uncorrected energy inside the jet cone (this includes electromagnetic and hadronic calorimeter) .
Jets from partons contain hadrons, and may contain photons and leptons. In particular neutral pions are an integral part of the produced hadrons. Pions decay into two photons. Photons deposit their energy in the electromagnetic calorimeter. Thus it is expected, that a jet caused by a parton exhibits an $emf > 0$. Therefore the lower boundary is set to 0.05. Electromagnetic objects like electron or photon, completely deposit their energy inside the electromagnetic calorimeter, thus $emf \simeq 1$. Therefore the upper boundary is set to 0.95.

- coarse hadronic fraction (chf) :

$$chf := \frac{E_{CHCAL,cone}}{E_{CAL,cone}} < 0.4$$

where $E_{CHCAL,cone}$ is the fraction of uncorrected jet energy inside the jet cone found in the hadonic calorimeter.
The coarse hadronic calorimeter is suspectible to noise effects. Thus jets with a large fraction of energy coming from that part are removed.

- ratio of the highest to the next-to-highest transverse energy cell ($hotf$) :

$$hotf < 10$$

It is expected, that a jet caused by a parton spreads its energy almost evenly over several calorimeter towers. Jets with an energy deposition being too focused on a small calorimeter region (i.e. single cells) are suspected to be noise-jets.

- number of towers containing 90% of the jet energy ($n90$) :

$$n90 > 1$$

This can be seen as a supplement to the $hotf$ criterion.

- L1 Confirmation :

$$\frac{L1Set}{p_t(1-chf)} > \begin{cases} 0.4 & : \text{ central and endcap region} \\ 0.2 & : \text{ ICD region} \end{cases}$$

This criteria compares the uncorrected scalar transverse energy L1Set[5] seen by the level 1 trigger to the reconstructed transverse momentum p_t times the fraction of energy seen by the electromagnetic and the fine hadronic calorimeter $(1-chf)$. Hereby noise-jets emerging from the electronics assembly are removed.

Jets fulfilling these criteria are called **quality-jets**. Quality-jets are corrected for jet energy scale.

4.1.4 Track-jets

Originally (in DØ) jets are calorimeter objects. Their definition includes no track requirement. Usually one expects, that a jet includes charged particles (e.g. charged pions), therefore associated tracks may exist.
This is exploited by another method where only track information is used to identify parton final states. Objects found by this method are called **track-jets** . They are independent of calorimeter information.

The algorithm [43] used to find track-jets is an extension of the standard simple cone algorithm.

[5] Scalar sum of transverse energy inside cone, excluding the coarse hadronic calorimeter.

Starting with the highest p_t track of an event, η, ϕ and z are calculated. z is defined as the z-position of closest approach of the track. Looping in descending order of track p_t, tracks are added to the jet cone if :

- $\Delta\mathcal{R}(track_i, track_{i+1}) < cone\ radius$
- $\Delta z(track_i, track_{i+1}) < \delta z$

where δz is the maximal distance with respect to z-direction.
Once a track has been added, the variables (η, ϕ and z) are recomputed by adding the track momentum and averaging the z-position. Parameters used in this analysis are :

- $cone\ radius = 0.5$
- $\delta z = 1.0$ cm

A cluster of tracks is labeled as track-jet if :

- at least two tracks are inside the cone
- total E_t of tracks inside cone > 2 GeV
- seed track $E_t > 1$ GeV

Track-jets are important to this analysis only if they are matched to quality-jets and carry some sufficient large fraction of the quality-jets transverse momentum (charged particle fraction, section 5.5).

4.1.5 Bad-jets

Given the situation, that a jet is found by the cone algorithm which does not fulfill at least one of the criteria of section 4.1.4, the jet gets categorized as a **bad-jet**.
These bad-jets are still part of the event, but they are not regarded as representation of any final state particle. Nevertheless bad-jets are be caused by partons[6] in some extend, but the largest fraction is suspected to originate from noise effects and other particles. Bad-jets are not corrected for jet energy scale.

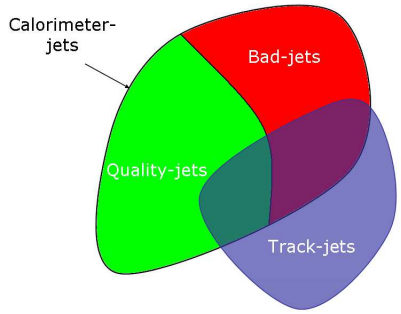

Figure 4.5: Relationship between different jet types (no quantification indicated).

[6]See Fig. 5.19, where bad-jets are also found in the Monte Carlo simulation.

4.2 Muons

Muons are identified via the muon system (see section 2.2.3). However, not each signal coming from the muon system implies the presence of a muon coming from the interaction point. Like in the case of jets, some minimal signal criteria have to be fulfilled. These are ("loose"-criteria) :

- at least two A layer wire hits and at least one A layer scintillator hit
- at least two BC layer wire hits
- at least one BC layer scintillator hit

In case of a central track match[7], two alternative criteria exist :

- at least one BC layer scintillator and at least two BC layer wire hits, or
- at least one scintillator and at least two A layer wire hits

Muons are important to this analysis in the sense, that they are not wanted, if they are not contained in a jet.

To descriminate muons inside jets from isolated ones, an isolation criteria is applied. A muon is labeled "isolated" if the following conditions are met :

- sum of energy in calorimeter cells in a hollow cone (Fig. 4.6) with radii $\Delta\mathcal{R}_i = 0.2$ and $\Delta\mathcal{R}_a = 0.4$ with respect to the muon track less than 8 % of the muon p_t
- sum of p_t of all tracks within a cone of radius $\Delta\mathcal{R} = 0.5$ around the muon track [8] less than 6% of muon p_t.

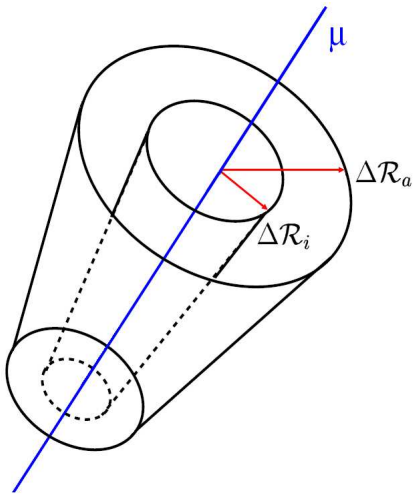

Figure 4.6: Illustration of isolation criteria.

[7] The muon system information may be sufficient to identify the central track caused by the muon.
[8] Excluding the muon track itself, when matched

4.3 Electrons and Photons

Electrons[9] and photons are identified with the electromagnetic part of the calorimeter and the tracking system. Shower shapes of electrons and photons look the same, the only difference is the existence of a track pointing to a shower caused by an electron. Electron and photon signals are considered as of reasonable quality if the following criteria are fulfilled :

- $emf := \frac{E_{ECAL,0.4}}{E_{CAL,0.4}} > 0.9$ where $E_{ECAL,0.4}$ is the energy inside the electromagnetic calorimeter contained in a cone with radius $\Delta\mathcal{R} = 0.4$ around the electron/photon direction and $E_{CAL,0.4}$ the total energy (electromagnetic + hadronic) inside the cone.
- $hmx7 < 20$: hmx7 is a quantity calculated from several variables concerning shower shape, energy deposition and vertex position. Its value indicates the correlation of the measured shower and reference showers from Monte Carlo simulations. Details can be found in [48] and [49].

Electrons are important to this analysis if they are not contained in a jet, i.e. they are isolated (similar to the muon case). An electron/photon is considered to be isolated, if

$$iso := \frac{E_{CAL,0.4} - E_{ECAL,0.2}}{E_{ECAL,0.2}} < 0.15$$

4.4 Missing Transverse Energy MET

Under the assumption of momentum conservation with respect to the transverse plane[10], the vectorial sum of transverse components of the momentum of all produced particles must add up to zero.

Particles like the neutrino leave the detector without recognition. Thus, such an event seems to violate momentum conservation, when looking only at momenta of reconstructed particles .
For those cases a new variable called "missing transverse energy" (MET)is introduced (Fig. **??**).

The MET variable is also adequate to characterize mono-jet events. One parton + undetectable particles means that on detector level the azimuthal angle between the direction of the jet and MET equals 180° and the ratio p_t/MET equals 1 (Fig. 4.8). The MET variable used in this analysis is calculated in the following way [30] :

- determine the missing transverse energy according to all calorimeter cells with energy > 0 , except those belonging to the coarse hadronic calorimeter,
- correct for those cells of the coarse hadronic part belonging to quality-jets,
- account for jet energy scale of quality-jets,

[9] The notion "electron" always denotes electrons and positrons. No differentiation is made here.

[10] The longitudinal components of the momentum of the interacting quarks are not balanced, since the longitudinal components of the momenta of proton and antiproton are not equally distributed to the constituting quarks (see section 3.4 parton distribution functions of proton). The transverse component of the protons and antiprotons momenta is about 0, therefore the transverse momenta of the constituents are about 0 as well. Thus the transversal components of momenta of produced particles must add up to zero.

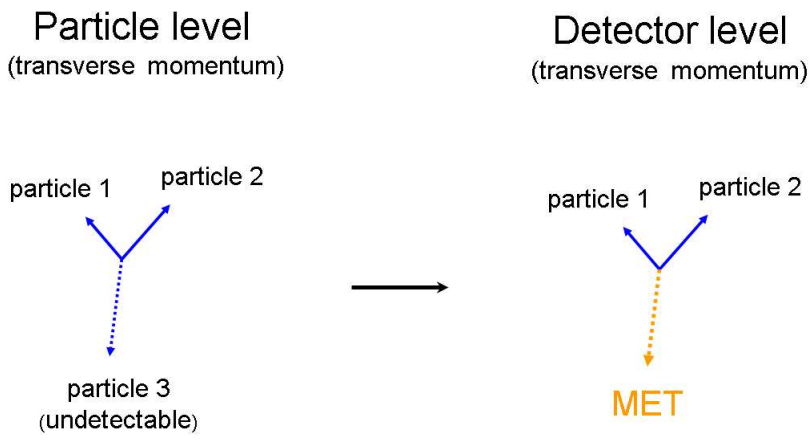

Figure 4.7: MET is generated by undetectable particles. On the left : transverse momentum conservation on particle level. On the right : transverse momentum conservation on detector level, where MET substitudes the undetectable particle.

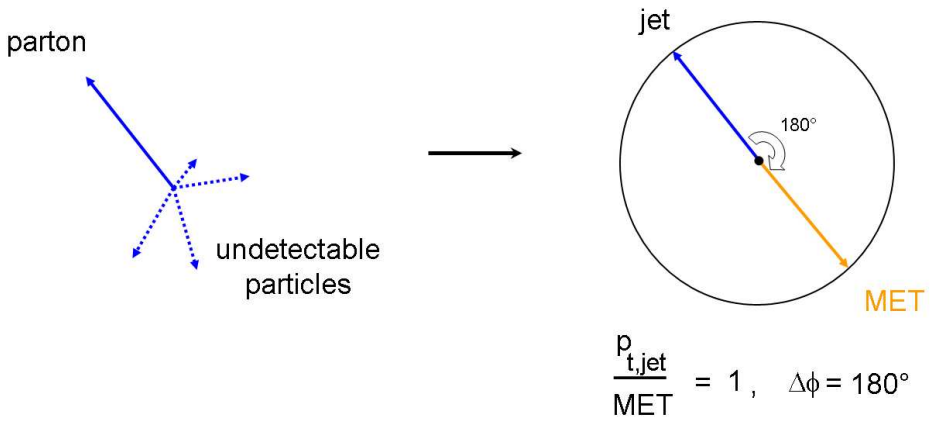

Figure 4.8: MET in mono-jet event. MET points in the opposite direction with the same absolute value.

- account for electromagnetic scale of good em-objects, i.e. photons and electrons fulfilling the criteria given in section 4.3, if they do not match a quality-jet,
- account for medium[11] muons (track matched or not) by simply subtracting the transverse momentum of each muon. To avoid energy double counting, the energy the muon looses as a minimum ionizing particle ($\simeq 2GeV$) is subtracted.

[11] "medium" is a stricter requirement concerning the quality of a muon signal than the "loose" requirement given in section 4.2. The exact definition can be found in [31].

Chapter 5

Mono-jet Analysis

5.1 Introduction

These days a lot of models beyond the Standard Model predict new particles (see section 3.4). In case these particles are undetectable[1] and couple to Standard Model particles in the manner described (Fig. 3.13, 3.17, 3.18, 3.19), they are expected to leave a mono-jet signature (one jet plus nothing else).
In a real experiment the notion "nothing" it is not well defined. Particles need to be identified (reconstructed) from the detector output. However, every identification method has its limitations (regions of bad efficiency[2]). We define "nothing" starting from that point, where the identification process gets unreliable.

5.1.1 Definition

In this analysis an event is called mono-jet event, if the following conditions are met :

- exacly one quality-jet (sect.4.1.1) above a p_t threshold of 30 GeV and $\eta < |0.4|$ ("jet 1")
- no second quality-jet above a p_t threshold of 15 GeV and $|\eta| < 2.6$
- the ratio $p_{t,jet1}/MET \in [0.9, 1.1]$ (Fig. 4.8)
- $\Delta\phi(jet1, MET) \geq 0.9 \cdot \pi$ (Fig. 4.8)
- no isolated muons with $p_t > 10$ GeV and $|\eta| < 2$
- no isolated electrons and photons with $p_t > 10$ GeV and $|\eta| < 2.6$
- no bad-jets above a p_t threshold of 15 GeV and $|\eta| < 2.6$

[1] With respect to the detector used.
[2] In case of jets these are low p_t and high pseudorapidity regions.

The bad-jet veto was adopted since their origins may be final state partons (see section 5.6). A mono-jet event according to this definition is shown in Fig. 5.1.

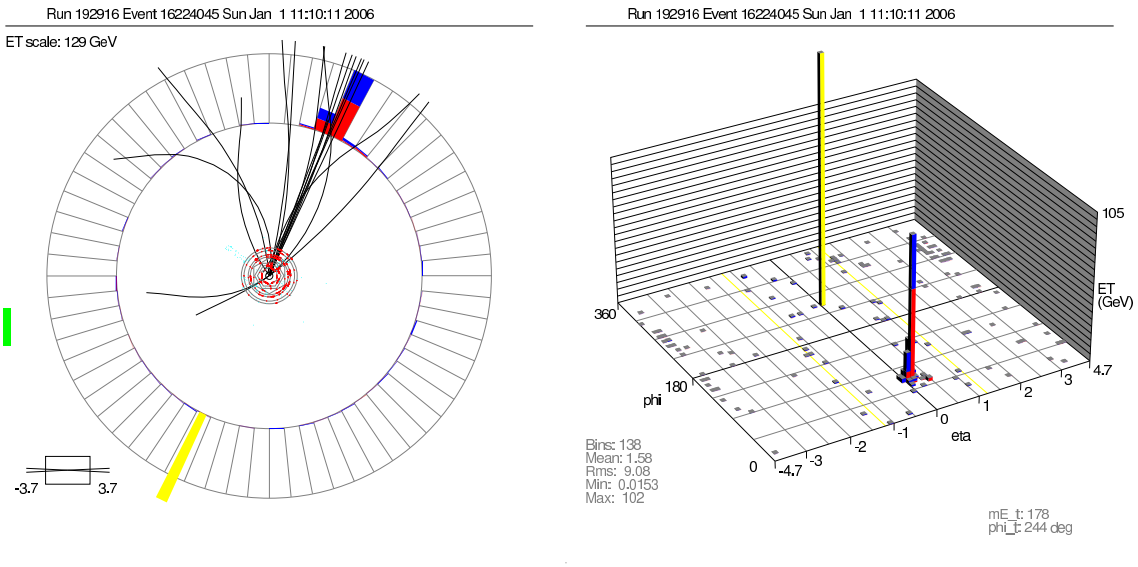

Figure 5.1: Mono-jet event. The leading quality jet exhibits a transverse momentum of roughly 180 GeV.

5.1.2 Considered mono-jet sources

Four categories of mono-jet event sources are considered in this analysis (they can be considered as background sources to new physics mono-jet events) :

1. Mono-jets due to Standard Model processes with mono-jet final states (parton + undetectable particles, see sect.5.1)

2. Mono-jets due to detector and reconstruction inefficiencies

3. Mono-jets due to atmospherical muons ("cosmics")

4. Mono-jets due to detector deficiencies ("noise effects")

The aim is to either account for these categories by simulations or if not available to reduce them as much as possible.

Category 1 :

a) relevance :

The relevance of this category has already been discussed in section 3.4. It contains only one process ($Z + jet \rightarrow \nu\bar{\nu} + jet$).

b) treatment :

This contribution is considered as irreducible (with respect to mono-jets due to new physics). Therefore it is accounted for by simulated events (Table 5.1).

Category 2 :

a) relevance :

The second category contains cases where Standard Model processes with non mono-jet final states get detected or reconstructed as mono-jet events (according to the definition given before). A list of expected processes is shown in Table 5.1 and Fig. 5.3.

Examples :

- A W$\rightarrow \tau\nu$ event with initial state radiation where the muon is not properly detected, thus not reconstructed, fulfills the mono-jet event definition.
- A QCD $q\bar{q} \rightarrow q\bar{q}$ event (di-jet event) where one of the partons heads into the beam pipe direction and thus can not be detected properly, fulfills the mono-jet event definition.

Processes including a τ-lepton play a special role. τ-leptons may decay hadronically, leave a jet signature in the calorimeter and finally contribute to the set of parton jets (in case all quality criteria are fulfilled). It is not attempted to seperate jets caused by τ-leptons from jets caused by partons. Therefore the process W$\rightarrow \tau\nu$ is considered as well.

b) treatment :

Also these contributions are considered as irreducible. They are accounted for by simulated events (Table 5.1).

Remarks :

- Only processes with the largest cross sections were used (therefore the list may not be exhaustively).
- Leading order cross sections of QCD and $Z/\gamma^* \rightarrow q\bar{q}$ are as calculated by Pythia.
- Leading order cross sections of Alpgen samples are as calculated by Alpgen.
- Next to leading order cross sections of W samples were taken from [55].
- Non QCD k-factors (accounting for next to leading order contributions) were taken from [55], [61]. Assumed errors on cross sections are discussed in section 5.2.

- Next to leading order contributions of QCD processes were taken care of by a global k-factor of $1.35 \cdot (1 \pm 0.12)$ (Fig. 5.2).
- All Pythia samples are complemented by initial and final state radiation (section 3.4).
- The DØ specific request-ids (uniquely labeling the MC sample) of these samples are listed in appendix A.2.

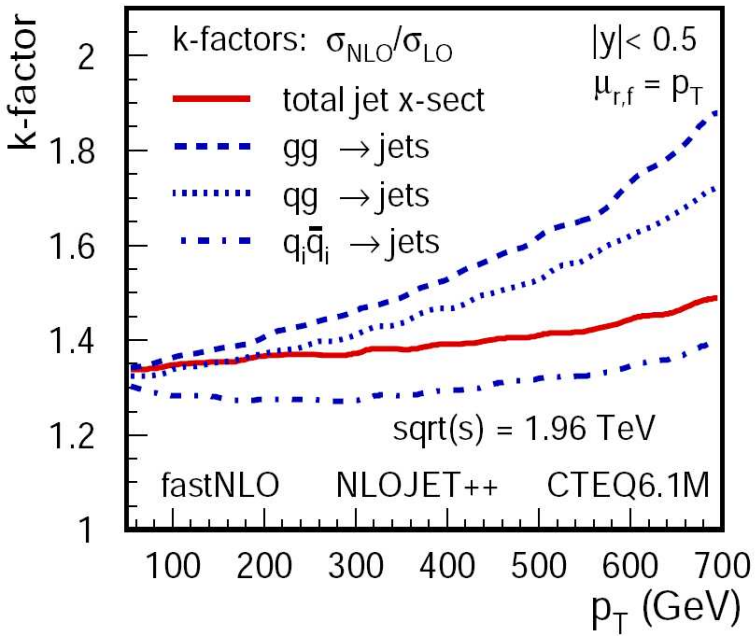

Figure 5.2: QCD k-factor taken from [51].

Category 3 :

a) relevance :

Atmospherical muons are created when cosmic radiation interacts with the atmosphere. Once in while a high energetic muon is created and traverses the detector. With some probability a calorimeter shower is initiated (this gets more probable the higher the energy of the muon). If these energy depositions get reconstructed as jet, the event exactly matches the mono-jet definition, since the jet is balanced only by MET.

b) treatment :

Currently there is no MC simulation available for this scenario and we have no quantitative estimation of the influence of atmospherical muons. Therefore it is attempted to reduce this contribution as good as possible. This is done by means of the muon system scintillators. Due to their good time resolution ($\Delta t = 2.2$ ns, section 2.2.3) it is possible to apply a veto on muons traversing the detector outside an interval around the nominal interaction time. The explicit parameters are given in section 5.5. This requirement of course does not totally remove their influence.

No.	**process**	**category**	**generator**	**used cross section** σ_{NLO} [pb]	k-factor (NLO)	N_{events}
1	$Z + jet \to \nu\bar{\nu} + jet$	1	Alpgen	474 (m_Z=60-130 GeV)	1.167	195000
2	$W \to \tau\nu$	2	Pythia	2769	1.356	548731
3	$W \to \mu\nu$	2	Pythia	2769	1.356	916250
4	$W \to e\nu$	2	Pythia	2769	1.356	914750
5	$Z/\gamma^* \to q\bar{q}$	2	Pythia	3141 (m_Z=60-130 GeV)	1.38	251000
6	$Z + 2jet \to \nu\bar{\nu} + 2jet$	2	Alpgen	174 (m_Z=60-130 GeV)	1.306	55250
7	QCD	2	Pythia		1.35	
	$10 < \hat{p}_t < 20$			724410000		209000
	$20 < \hat{p}_t < 40$			40900000		209000
	$40 < \hat{p}_t < 80$			1755000		460870
	$80 < \hat{p}_t < 160$			52650		355000
	$160 < \hat{p}_t < 320$			905		117414
	$320 < \hat{p}_t < 960$			4.66		20000

Table 5.1: Monte Carlo Samples of mono-jet channel contributing processes from category 1 and 2. Implemented parametrization of parton distribution functions is CTEQ5L (for all samples). Leading order Feynman diagrams showing how these processes contribute are shown in Fig. 5.3. Displayed cross sections include the k-factors.

Category 4 :

a) relevance :

The calorimeter (in the first place) is suspectible to noise effects. Such noise signals may be identified as jets ("noise jets"). It is expected that once in a while a noise-jet makes its way through all quality criteria (section 4.1.3) and cuts. Noise-jets are like in the case of atmospherical muons balanced only by MET. This again matches the mono-jet event definition .

b) treatment :

Noise effects of different detector subsytems (calorimeter, tracking system, muon system,...) are expected to be independent of each other. To get a grip on mono-jets caused by calorimeter noise, we demand a confirmation of the calorimeter jet by the central tracking system ($\rightarrow$ **charged mono-jets**, cp. with section 4.1).
The algorithm described in section 4.1.5 searches the tracker output for associated tracks to form track-jets. The influence of noise effects to track-jet confirmed calorimeter quality-jets is expected to be negligible. The explicit requirements and matching conditions are given in section 5.5.

5.1.3 Course of the Analysis

This analysis does not pursuit any of the particular approaches to mono-jets where a certain signal, predicted by a new theory (section 3.4), is isolated. It rather tries to enlighten, if there is at least a basic potential for new physics concerning the mono-jet channel in general. For this purpose the number of expected (from the Standard Model) and measured mono-jet events is compared over a wide range starting from a transverse momentum of 30 GeV.

The first step will be the consideration of a general jet data sample (inclusive jet sample). Here data is compared with the Standard Model QCD prediction (other sources like electroweak jet production are negligible on this general level). After that this sample is searched for mono-jet events according to the definition given before.

The exact proceeding is as follows :

1. Description of how differential cross sections and their errors are calculated (Sect. 5.2).

2. Selection of a suitable data sample (Sect. 5.3).

3. Comparison of data and Monte Carlo simulation with respect to the inclusive jet sample (Sect. 5.4).

4. Approach of the final mono-jet sample (Sect. 5.5).

5. Analysis of mono-jet events in the final sample (Sect. 5.6).

6. Summary and Conclusion (Sect 5.7).

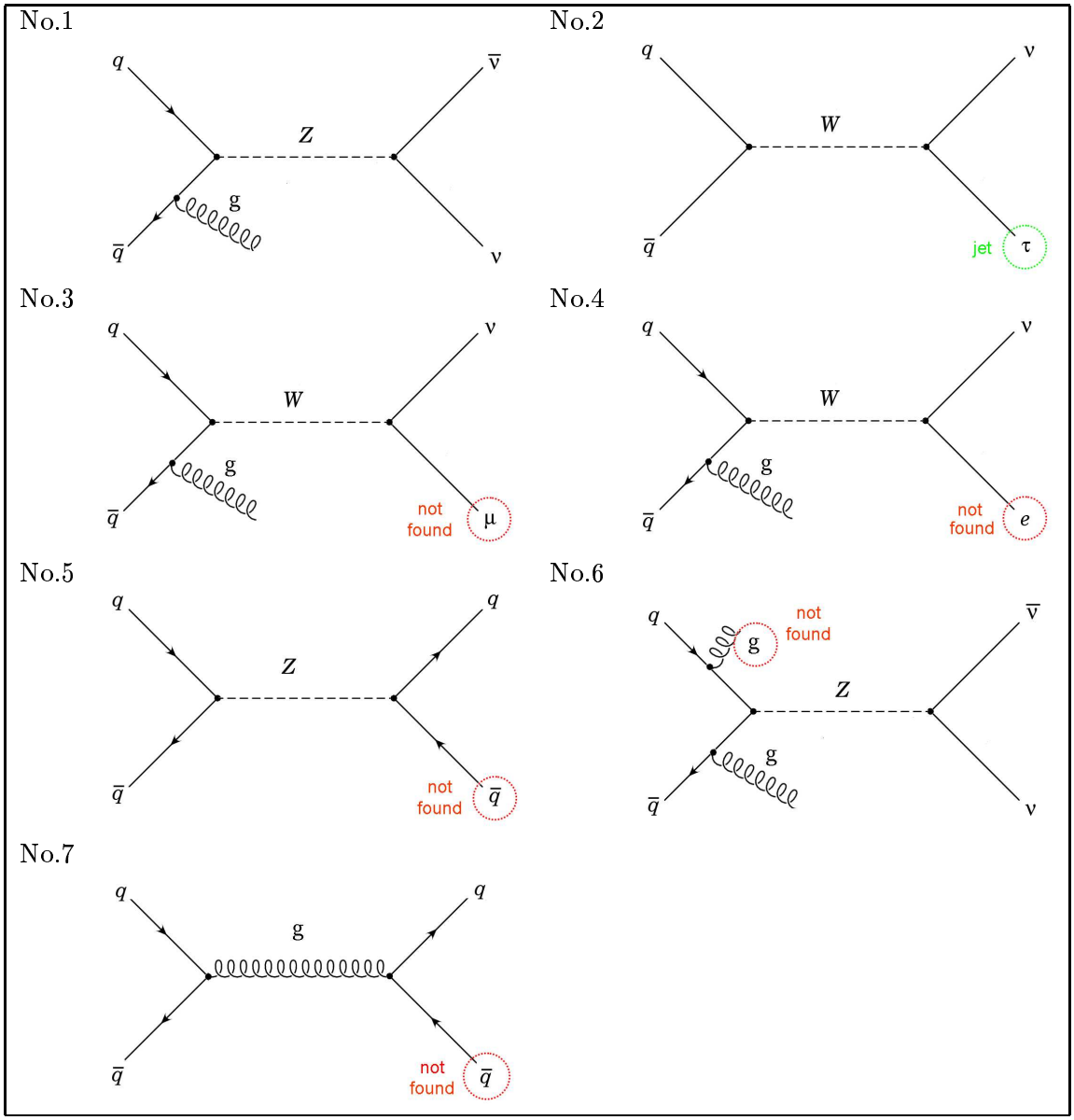

Figure 5.3: Leading order Feynman diagrams of processes contributing to mono-jet class (Table 5.1). Due to detector and reconstruction inefficiencies final state particles may not be recognized as such.

5.2 Differential Cross Section and Error Calculation

Let Λ be any of the later on displayed quantities, i.e. $\Lambda \in \{p_t, \eta, \phi, MET, ...\}$. The differential cross section $d\sigma/d\Lambda$ is determined as follows :

a) **Data :**

Each event is weighted by $1/\mathcal{L}_i$ where $\mathcal{L}_i$ is the trigger luminosity (Table 5.2) of trigger i according to the trigger which selected the event.
Let $d\Lambda$ be some finite interval. The weights of events yielding a contribution to the

considered interval are summed, thus

$$\frac{d\sigma}{d\Lambda} = \sum_{i=1}^{n_{trig}} \frac{N_{\Lambda,i}}{\mathcal{L}_i} \tag{5.1}$$

where $N_{\Lambda,i}$ is the number of events inside the interval $d\Lambda$ selected by trigger i and n_{trig} the number of triggers (disjoint trigger intervals and trigger luminosities are displayed in Table **??**).

Statistical error :

$$\Delta\left(\frac{d\sigma}{d\Lambda}\right)_{stat} = \sqrt{\sum_{i=1}^{n_{trig}} \frac{N_{\Lambda,i}}{\mathcal{L}_i^2}}$$

where Poisson statistics ($\Delta N = \sqrt{N}$) was assumed.

Systematic errors :

- Luminosity : The global relative error of the luminosity $\Delta\mathcal{L}/\mathcal{L}$ is about 6.5% [18]. The error on the differential cross section is assumed to be :

$$\Delta\left(\frac{d\sigma}{d\Lambda}\right)_{lum} = \frac{d\sigma}{d\Lambda} \cdot \frac{\Delta\mathcal{L}}{\mathcal{L}}$$

- Jet energy scale : To estimate the error on JES the entire analysis was redone (on data, MC unchanged) using upper (+) and lower (−) error values of JES (see Fig. 4.4) for all quality-jets in the event. This yields varied differential cross sections

$$\frac{d\sigma^{(+)}}{d\Lambda} \quad \text{and} \quad \frac{d\sigma^{(-)}}{d\Lambda}$$

respectively.
The error on the differential cross section is assumed to be :

$$\Delta\left(\frac{d\sigma}{d\Lambda}\right)^{(\pm)}_{JES} = \left|\frac{d\sigma}{d\Lambda} - \frac{d\sigma^{(\pm)}}{d\Lambda}\right|$$

Possible asymmetries were propagated to the total error.

Total error :

The total error is obtained by adding the single contributions quadratically (assuming independence):

$$\Delta\left(\frac{d\sigma}{d\Lambda}\right)^{(\pm)}_{tot} = \sqrt{\left(\Delta\left(\frac{d\sigma}{d\Lambda}\right)_{stat}\right)^2 + \left(\Delta\left(\frac{d\sigma}{d\Lambda}\right)_{lum}\right)^2 + \left(\Delta\left(\frac{d\sigma}{d\Lambda}\right)^{(\pm)}_{JES}\right)^2}$$

b) **Monte Carlo :**

$$\frac{d\sigma}{d\Lambda} = \sum_{i=1}^{n_{MCs}} \frac{k_i \cdot \sigma_i}{N_{MC,i}} N_{\Lambda,i}$$

where σ_i is the leading order (LO) cross section of the process i (Table 5.1), k_i the k-factor of process i, $N_{MC,i}$ the number of events contained in sample i, n_{MCs} the total number of used Monte Carlo samples and $N_{\Lambda,i}$ the number of events of sample i contributing to the interval Λ.

Statistical error :

$$\Delta\left(\frac{d\sigma}{d\Lambda}\right)_{stat} = \sqrt{\sum_{i=1}^{n_{MCs}} \left(\frac{k_i \cdot \sigma_i}{N_{MC,i}}\right)^2 N_{\Lambda,i}}$$

(again assuming Poisson statistics).

Systematic errors:

- cross section : The next to leading order (NLO) cross section of process i is given by :

  $$\sigma_{i,NLO} := k_i \cdot \sigma_i$$

  The error on $\sigma_{i,NLO}$ depends on the considered sample. Used Monte Carlo samples are displayed in Table 5.1 . The relative error on the NLO cross section for W and Z samples was assumed to be 4% [61].
  The error on the QCD NLO cross section was propagated via an assumed error on the k-factor of 12% (Fig. 5.2).
  The single W and Z error contributions were added in absolute terms, since they are not independent of each other. Then this contribution was quadratically added to the QCD contribution, yielding

  $$\Delta\left(\frac{d\sigma}{d\Lambda}\right)_{\sigma_{NLO}}$$

5.3 Data Sample

The events chosen from the full recorded data set (between December 2001 and August 2004) are those selected by the jet triggers listed in Table 5.2. This sample is provided by the common samples group. It is labeled as **"CSskim-QCD-p14.fixtmb2.02"**, where p14 labels the reconstruction software version (DOReco) and fixtmb2.02 the offline re-reconstruction software version (PASS2 data).

This data is provided in a DØ-specific format called TMB ("thumbnail"). Before doing the analysis this data is processed with the package TopAnalyze [39] to give Root-files [38] as output. These Root-files consisting of Root-Trees, still containing the relevant information, are then analysed.

Cleaning the sample :

The data sample still needs to be cleaned of "bad" events, provided via lists of bad runs and bad luminosity blocks (LBs) . Runs and LBs are marked as bad if inconsistencies are found, which do not match the usual behavior of the detector. This can be due to broken detector parts or unusual noise appearance. Lists of bad runs and bad LBs were compiled in the following way :

- Requesting bad runs corresponding to the detector parts being crucial to the analysis at the Offline Run Quality Database [40]. These are the CFT[3] and the calorimeter → list 1.
- Taking the JET/MET group [41] bad luminosity block selection → list 2.
- Using list 1 and list 2 as an input for the luminosity calculation tool "runrange_luminosity" [42]. As an output it provides improved trigger-wise ordered lists of bad LBs → list 3.

Events contained in at least one of these three lists were removed from the data sample.
The final cleaning step concerns special noise phenomena [60] (noon noise, empty crate, coherent noise, ring of fire). Events labeled by at least one of those, were excluded.

Calculating the luminosity :

As indicated before the luminosity is calculated with the tool runrange_luminosity [42]. As an input it demands a bad run and a bad luminosity block list as well as a runrange-list including trigger names and runranges (139500-196584). The calculated total delivered luminosity is :

$$\mathcal{L}_{del} = 498 \pm 32 pb^{-1}$$

The calculated trigger dependent luminosities[4] are listed in Table 5.2.

5.4 Inclusive Jet Sample

The inclusive jet sample constitutes the starting point of the data/MC[5] comparison. It is defined by the following requirements :

- a reconstructed vertex within $|z_0| < 50$ cm, with at least 3 attached tracks
- at least one reconstructed quality-jet[6] with $p_t > 30$ GeV and $|\eta| < 0.4$

Before the comparison is done, the calculated trigger luminosities (Table 5.2) are cross-checked and jet trigger turn on thresholds are determined (section 5.4.1).
After that (in section 5.4.2) samples of simulated events suitable to model the data are introduced (here : QCD Monte Carlo). In section 5.4.3 basic distributions are compared and discussed.

[3] Good track information is needed for reliable track-jet reconstruction.
[4] Different due to prescaling (section 2.2.5).
[5] MC = Monte Carlo = simulated events
[6] A jet which fulfills all standard quality criteria (listed in section 4.1.4)

trigger	**definitions**			$\mathcal{L}_{trigger}$	**min.** p_t	**max.** p_t
	level 1	level 2	level 3	$[pb^{-1}]$	[GeV]	[GeV]
JT8TT	one calorimeter trigger tower with $E_t > 5$ GeV	unrestricted	one simple cone jet with $E_T > 8$ GeV	0.025 ±0.002	–	–
JT15TT	two calorimeter trigger tower with $E_t > 3$GeV	unrestricted	one simple cone jet with $E_T > 15$ GeV	0.113 ±0.007	30	70
JT25TTNG	three calorimeter trigger tower with $E_t > 5$ GeV	unrestricted	one simple cone jet with $E_T > 25$ GeV	2.16 ±0.14	70	90
JT45TT	two calorimeter trigger tower with $E_t > 5$ GeV	unrestricted	one simple cone jet with $E_T > 45$ GeV	35.90±2.33	90	130
JT65TT	three calorimeter trigger tower with $E_t > 5$ GeV	one jet candidate with $E_t > 20$ GeV	one simple cone jet with $E_T > 65$ GeV	172.48±11.21	130	180
JT95TT	three calorimeter trigger tower with $E_t > 5$ GeV	one jet candidate with $E_t > 50$ GeV	one simple cone jet with $E_T > 95$ GeV	386.05±25.12	180	230
JT125TT	four calorimeter trigger tower with $E_t > 5$ GeV	one jet candidate with $E_t > 60$ GeV	one simple cone jet with $E_T > 125$ GeV	395.79±25.73	230	∞

Table 5.2: Jet trigger definitions on different trigger levels. *Remarks :* • A trigger tower ($\Delta\eta \times \Delta\phi = 0.2 \times 0.2$) consists out of 4 calorimeter towers. In total there are 1280 trigger towers • A jet candidate is formed by clustering $n \times n$ (currently $n = 5$) trigger towers which are centered on seed towers (=level 1 trigger towers)[45] • The simple cone algorithm applied on level 3 uses no midpoints as additional seed candidates (unlike the "Run II Cone Algorithm" (sect. 4.1.1)) • $\mathcal{L}_{trigger}$ is the trigger luminosity (this section) • min. and max. p_t indicate in which region the several triggers are actually used. These values are determined in section 5.4.

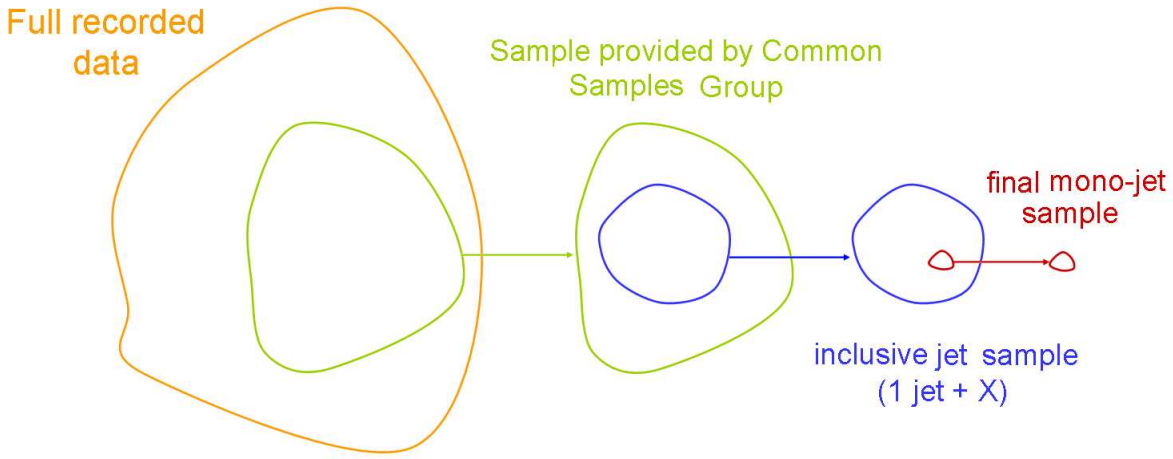

Figure 5.4: Steps towards the final mono-jet sample.

5.4.1 Final Preparations

Crosscheck of calculated trigger luminosities

To crosscheck the calculated trigger luminosities and trigger performance, the p_t distribution of the highest p_t quality-jet (within $|\eta| < 0.4$) for different triggers were plotted (Fig. 5.5).
The smooth transition between different triggers indicates the validity of these values. Inconsistencies would result in leaps between differents curves. The plot was split due to clarity.

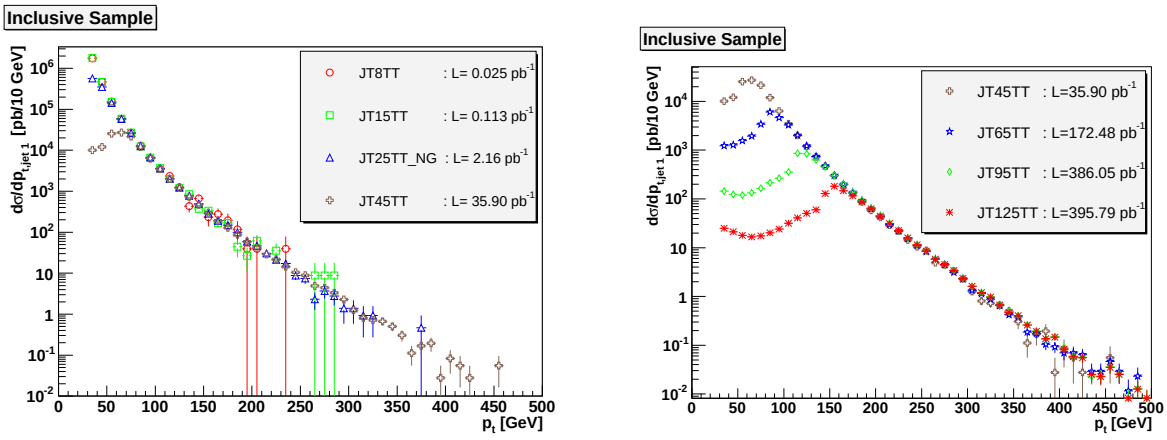

Figure 5.5: p_t distributions of highest p_t jet within $|\eta| < 0.4$ according to the different jet triggers.

Determination of jet trigger turn on thresholds

Low p_t jet triggers are highly prescaled, thus exhibit low statistics for high p_t jets (small cross section). On the other hand, high p_t jet triggers are blind with respect to low p_t jets. A data sample with reasonable statistics in the full p_t range is built by combining suitable p_t ranges of different jet triggers.
To do so the turn-on thresholds of jet triggers have to be determined.

Each trigger is characterized by two domains concerning its efficiency :

- blind domain : event characteristics do not match the trigger definition, these events are not selected by the trigger

- efficiency domain : event characteristics match trigger definition, these events are selected by the trigger (assuming that triggers are 100 % efficient)

The transition region (turn-on threshold) for jet triggers is determined by comparing each trigger with its lower neighbor trigger (e.g. JT65TT is the lower neighbor of JT95TT). This is an adequate method, because the trigger definition of the considered trigger defines a true subset[7] of events matching the definition of the lower neighbor trigger.
Therefore it can be assumed, that when looking at the transition region of the considered trigger, the lower neighbor trigger is well in its efficiency domain.
The distinguishing feature of the jet-triggers is the transverse momentum of the matching jet. Therefore the efficiency ϵ_{JT95} of trigger JT95TT (the others as well) may be defined by :

$$\epsilon_{JT95}(p_t) := \frac{\frac{N_{95}(p_t)}{\mathcal{L}_{95}}}{\frac{N_{65}(p_t)}{\mathcal{L}_{65}}}$$

where $N_{95}(p_t)$ is the number of events seen by JT95TT with respect to the transverse momentum of the matching jet ($N_{65}(p_t)$ accordingly).
The trigger luminosities ($\mathcal{L}_{95}$ and $\mathcal{L}_{65}$, Table 5.2) account for the different prescales of the triggers[8]. The procedure is feasible for all jet-triggers except JT8TT, because there is no lower neighbor trigger.
The results are shown in Fig. 5.6. The turn on thresholds are marked by a green line.

The composition of jet triggers is done in the following way : each trigger is used starting from its threshold p_t up to where the higher neighbor trigger reaches its own threshold. The ranges are displayed in Table 5.2.

5.4.2 Simulated Events

The events contained in the chosen data set (green sample in Fig. 5.4), were selected by jet triggers. The dominant jet production processes at hadron colliders are those of QCD. Other

[7] Due to different prescales, this holds not for the actually selected events.
[8] This yields a reasonable normalization of the turn on curves (Fig. 5.6). They are not mandatory.

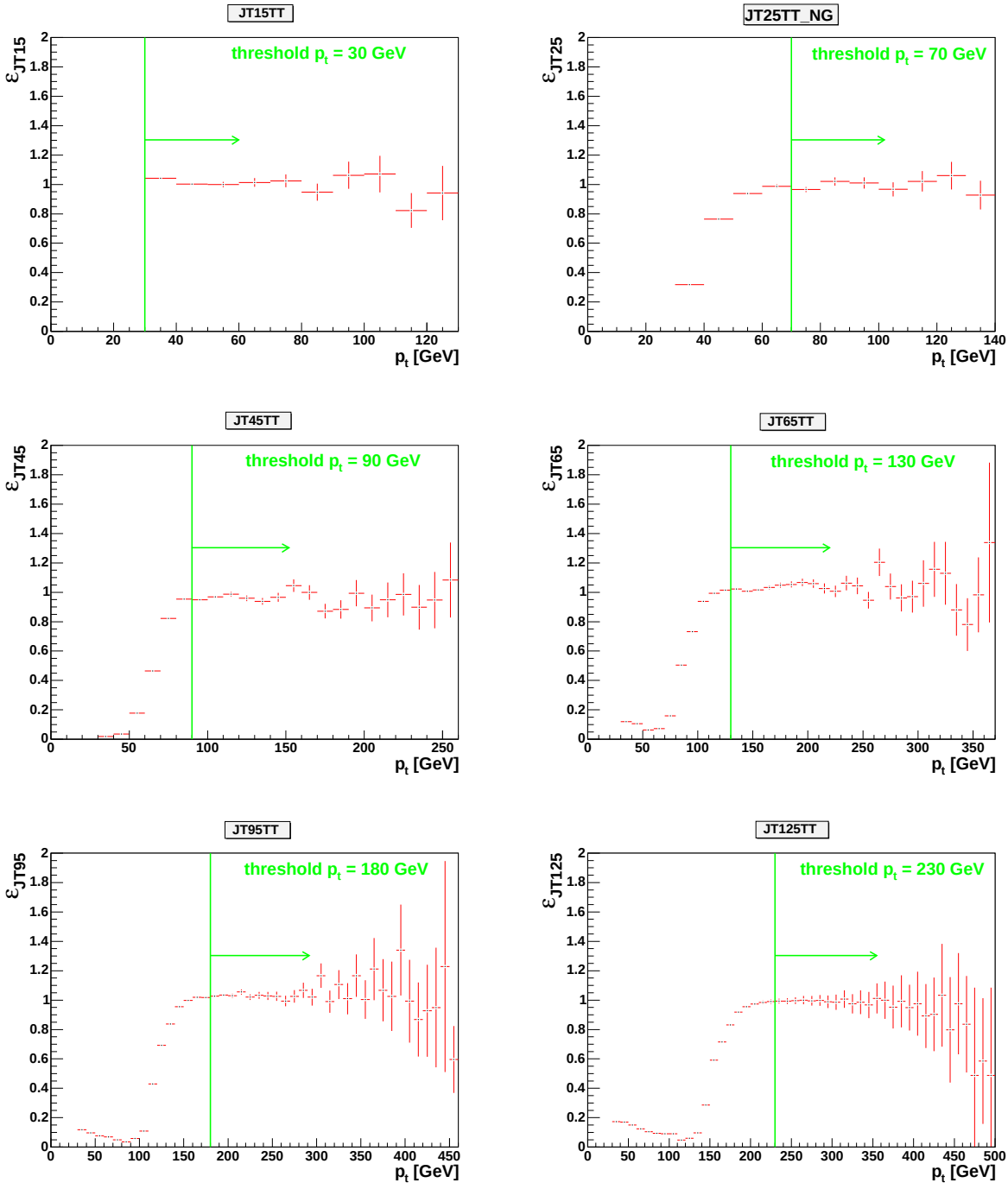

Figure 5.6: Jet trigger turn on curves.

jet production processes (electroweak) are negligible on this level (inclusive jet production). Thus simulated events of QCD should be sufficient to model the general behavior. Therefore it is not necessary to comprise any additional Monte Carlo samples than those listed in Table 5.1.

5.4.3 Data/MC Comparison

a) **p_t distribution of the leading central quality jet** (Fig. 5.7) :

The upper plot shows the p_t distribution of the leading (=highest p_t) central (=$\eta <$ |0.4|) quality-jet[9].
The lower plot shows the ratio of the differential cross section of data and MC. Statistical and total errors are indicated by the shading.

The integral of the differential cross section with respect to the interval $p_t \in [30\ \text{GeV}, \infty]$ yields

for data :

$$\sigma_{[30,\infty],data} = 2.54\ \pm 0.17\ (\text{lum})\ \pm^{0.66}_{0.56}\ (\text{JES})\ \cdot 10^6\ \ pb$$

$$= 2.54\ \pm^{0.68}_{0.58}\ (\text{tot})\ \cdot 10^6\ \ pb$$

for MC :

$$\sigma_{[30,\infty],MC} = 2.73\ \pm 0.31\ (\text{tot})\ \cdot 10^6\ \ pb$$

Statistical errors are negligible in both cases. The distributions and the integrals of data and MC agree within the total error.

The total error of data is dominated by the error of the jet energy scale. Its relative error is plotted in Fig. 5.8. It evolves from about 20% in the low p_t, up to 60 % in the high p_t region. The p_t distribution and the behavior of the jet energy scale error is in accordance with earlier analyses (e.g. [58]).

b) **η and ϕ distribution of the highest p_t jet** (Fig. 5.11) :

Due to the small η range the distribution is almost plain. Non-QCD contributions are not visible ($< 10^2\ pb/0.63$ and $< 10^2\ pb/0.1$ respectively) in the linear plot. Their η distribution is plain as well. The same holds for the ϕ distribution.

c) **Missing transverse energy MET** (Fig. 5.12) :

While we find agreement of data and MC for MET<100 GeV within the total errors (not plotted), the deviation for MET>100 GeV is not covered by the Standard Model prediction.

[9] The data distribution is in accordance with earlier analyses, e.g. [58].

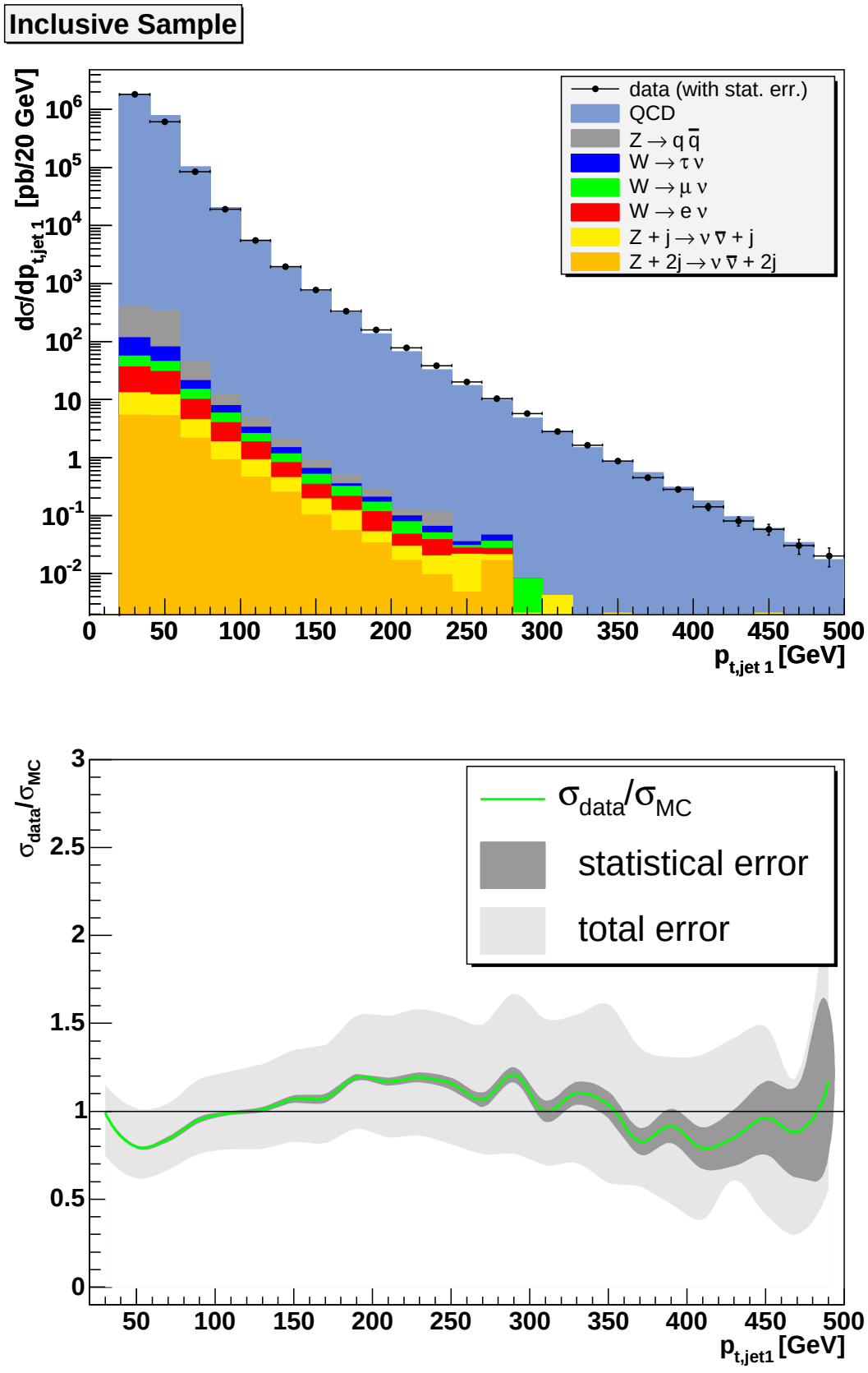

Figure 5.7: Top : p_t distribution of the leading (=highest p_t) central (=$|\eta < 0.4|$) quality-jet. Bottom : Ratio of data and Monte Carlo with statistical and total errors.

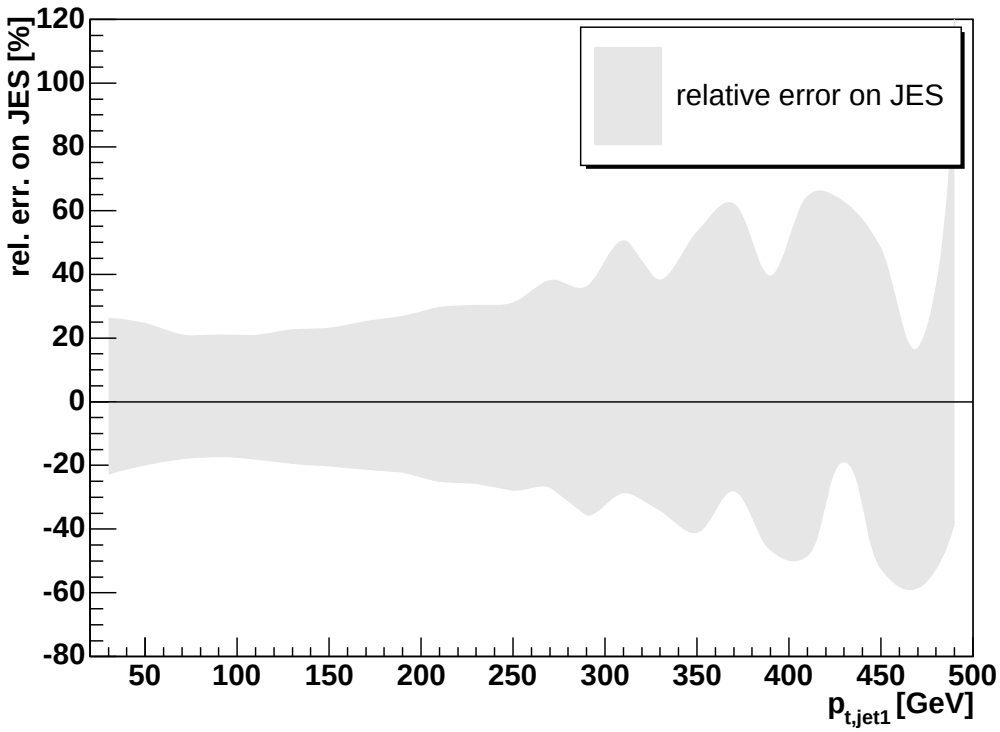

Figure 5.8: Distribution of the relative error on the jet energy scale (JES).

MET originates from two sources :

1. noise effects
2. undetectable particles (neutrinos, possibly yet unknown particles)

In the majority of cases an analysis, searching for new particles with aid of a MET requirement, is concerned with the separation of these contributions.
In this analysis a separation is attempted with respect to mono-jet events (definition includes MET requirement). The general case was not examined.
The observed deviation, though, indicates possibly new physics in the jets+MET channel.

d) **Number of quality-jets with $p_t > 15$ GeV within $|\eta| < 2.6$** (Fig. 5.10):

Events contained in the first bin are mono-jet candidates. However, most of the one-jet-events are not mono-jet events (according to the definition given in section 5.1). Their amount is largely reduced ($\simeq 98\%$) when the MET/$p_{t,jet1} \simeq 1$ condition is demanded. A largely contributing scenario is shown in Fig. 5.9.

The event actually contains two calorimeter jets, where only one is within the "fiducial" region (here : defined by $|\eta| < 2.6$). The MET is calculated with respect to both jets, thus failing the MET/$p_{t,jet1} \simeq 1$ condition (red circles). Similiar scenarios including 2 or more jets outside the fiducial region contribute to a moderate extent as well.

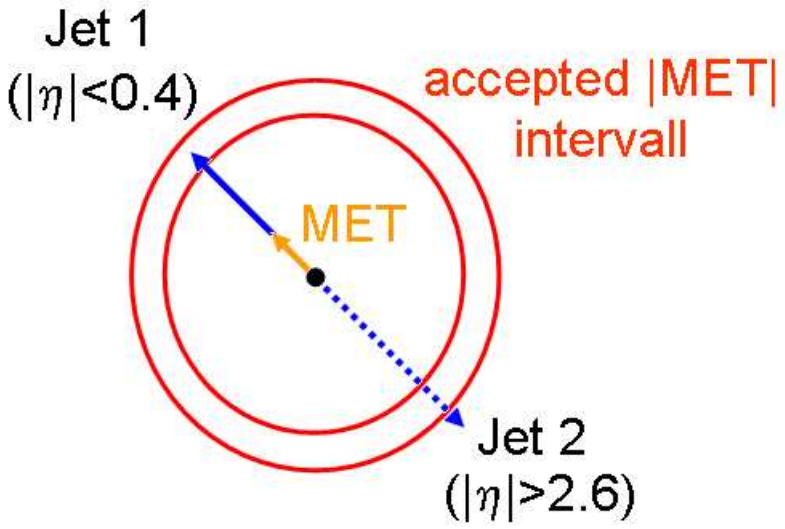

Figure 5.9: View onto transverse plane. Arrows indicate the transverse momentum. Red circles indicate the MET/$p_{t,jet1} \simeq 1$ condition.

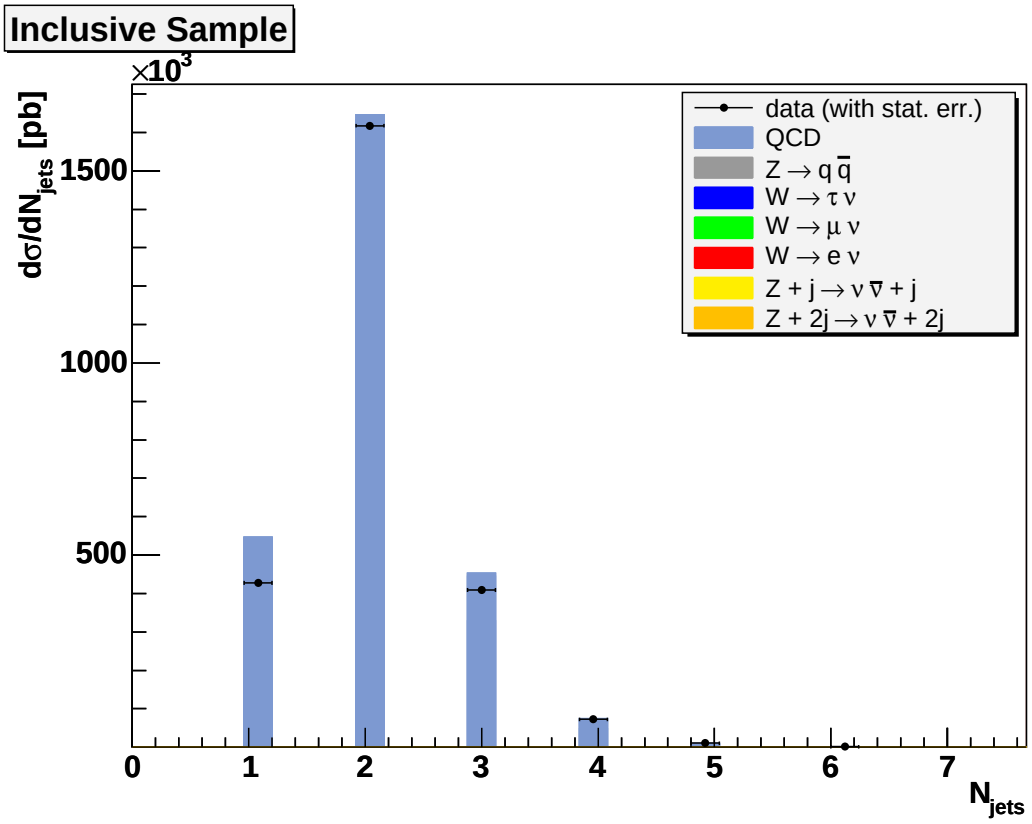

Figure 5.10: Number of quality-jets with $p_t > 15$ GeV, $|\eta| < 2.6$ per event.

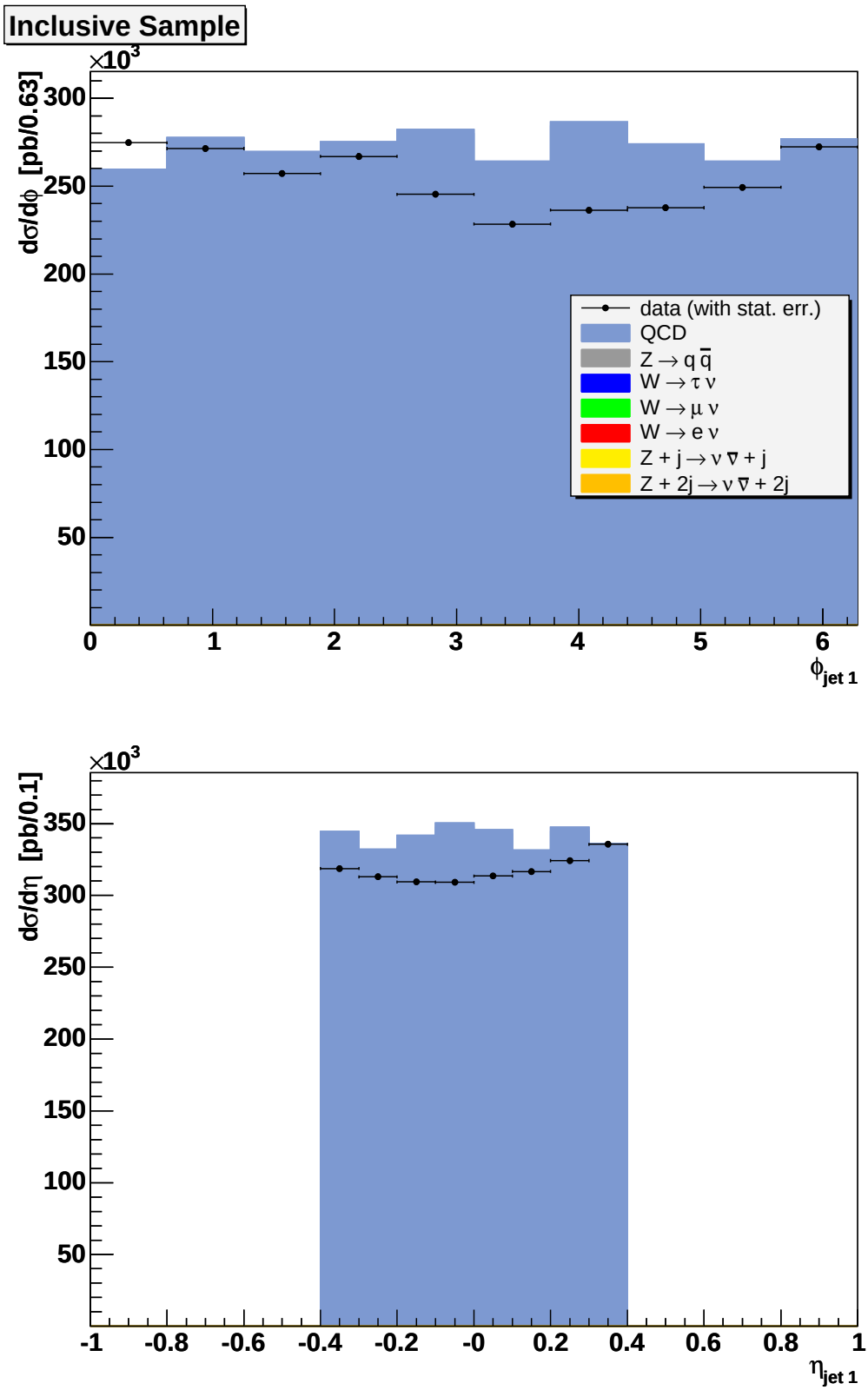

Figure 5.11: ϕ and η distribution of the leading central quality-jet.

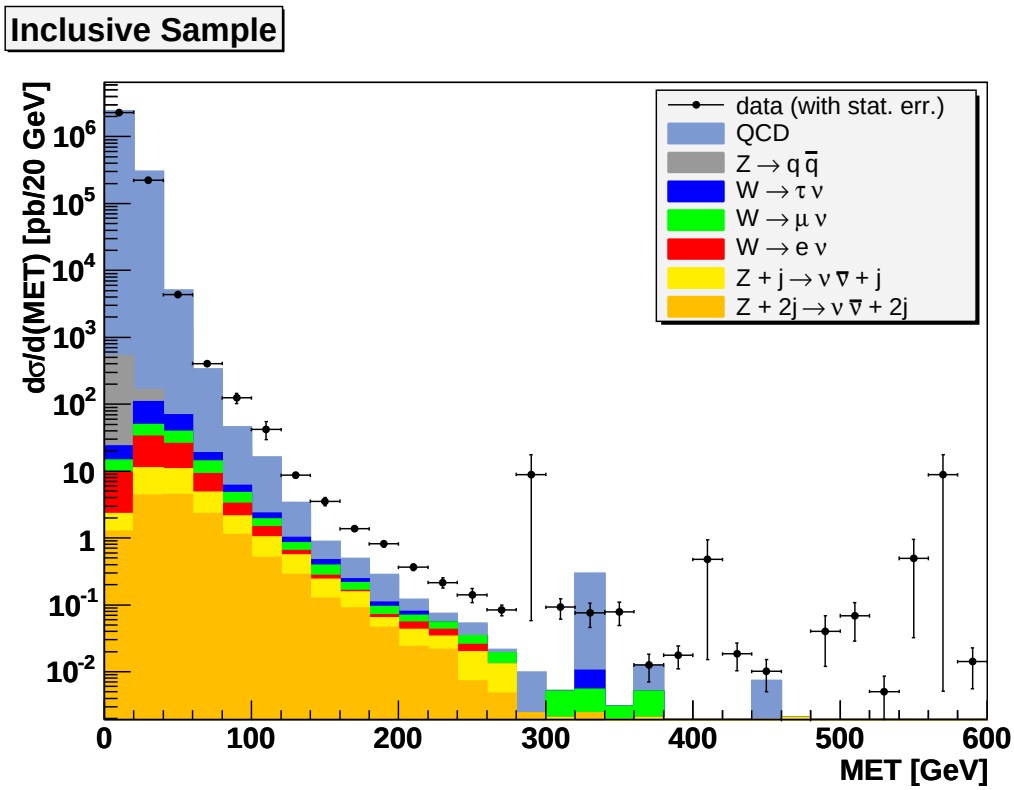

Figure 5.12: Distribution of missing transverse energy MET.

5.5 Approach of the final Mono-Jet Sample

Now the final mono-jet sample is approached. The applied cuts are listed in the following. They are motivated by the definition of mono-jets and considered background sources (given in section 5.1). Plots shown in this section are all with respect to the inclusive sample.

1.) **Cut on number of quality-jets**:

Events containing a second quality-jet with :

- $p_t > 15$ GeV
- $|\eta| < 2.6$

are removed.
Fig. 5.13 shows the p_t distribution of the second leading quality-jet. The applied cut is marked by the black line and arrow.

2.) **Cut on** $\Delta\phi(jet1, MET)$, (Fig. 5.14):

$\Delta\phi(jet1, MET)$ is defined as the azimuthal angle between the direction of the leading p_t quality-jet ("jet 1") and the direction of the missing transverse energy (MET). See also Fig. 4.8.

Events where

- $\Delta\phi(jet1, MET) < 0.9 \cdot \pi$

are removed.

3.) **Cut on ratio $p_{t,jet1}$/MET** , (Fig. 5.15):

Events where :

- $p_{t,jet1}/MET \notin [0.9; 1.1]$

are removed.
The distribution shows that most of the considered mono-jet sources are peaking in the region around 1 (excluding $Z \to q\bar{q}$ and QCD).

4a.) **Cut on isolated muons and reduction of atmospherical muons**, (Fig. 5.16):

Isolated muons :
Events containing isolated muons fulfilling the "loose" condition[10] with :

- $p_t > 10$ GeV
- $|\eta| < 2$

are removed.

Atmospherical muons :

Cut isolated muon cut includes no restrain on scintillator times. Thus isolated atmosherical muons are reduced as well. However, atmospherical muons, if recostructed as jet, are not expected to be isolated. They are expected to rather look like if they emerge from the jet they caused. The amount of events according to this scenario is reduced by the following requirement :

Events containing loose muons with :

- $p_t > 10$ GeV
- $|\eta| < 2$
- $|t_A| > 10\ ns$ for A layer scintillator time
- $|t_{BC}| > 10\ ns$ for BC layer scintillator time

where t_A and t_{BC} are measured with respect to the nominal interaction time (t=0), are removed.
No isolation criteria is demanded for these muons. On the other hand quality-jets containing muons (b-jets) are kept.

[10] Isolation and "loose" criteria are defined in section 4.2.

4b.) **Cut on isolated photons and electrons** (Fig. 5.17):
Events containing isolated photons or electrons[11] with :

- $p_t > 10$ GeV
- $|\eta| < 2.6$

are removed.
Currently there is no MC simulation available and we have no quantitative estimation of the influence of atmospherical muons. Their influence can only be lowered by this cut.

5.) **Cut on bad-jets** (Fig. 5.19) :
The definition of bad-jets was given in section 4.1.5. Events including at least one bad-jet with :

- $p_t > 15$GeV
- $|\eta| < 2.6$

are removed.
The distributions show a large excess of bad-jets in data. Bad-jets are suspected to basically emerge from noise effects. However, to some extent bad-jets are also found in the Monte Carlo simulation which indicates that some fraction of bad-jets may originate from final state partons. Therefore these events are excluded.

6.) **Track-jet confirmation** :
A calorimeter quality-jet ("cqjet") is considered as "track-jet confirmed" if a track-jet ("tjet") exists, which matches the conditions :

- $\Delta\mathcal{R}(\text{tjet, cqjet}) < 0.3$
- $cpf := \dfrac{p_t(\text{tjet})}{p_t(\text{cqjet})} > 0.05$

cpf stands for "charged particle fraction". The first criteria ensures a good overlap of calorimeter and track-jet cones, the second one ensures that attached tracks fulfill a minimum p_t requirement depending on the p_t of the calorimeter-jet. We call a track-jet confirmed mono-jet, **charged mono-jet**.

Cut	description	Events left	Figure
0	Inclusive Sample	1278543	
1	Cut on number of quality jets	82246	5.13
2	Cut on $\Delta\phi(jet1, MET)$	56304	5.14
3	Cut on ratio $p_{t,jet1}$/MET	1288	5.15
4	Cut on muons, photons and electrons	833	5.16 ,5.17
5	Cut on badjets	629	5.19
6	track-jet confirmation	170	5.20

Table 5.3: Summary of applied cuts, and number of events.

[11] Isolation and quality criteria are defined in Section 4.3

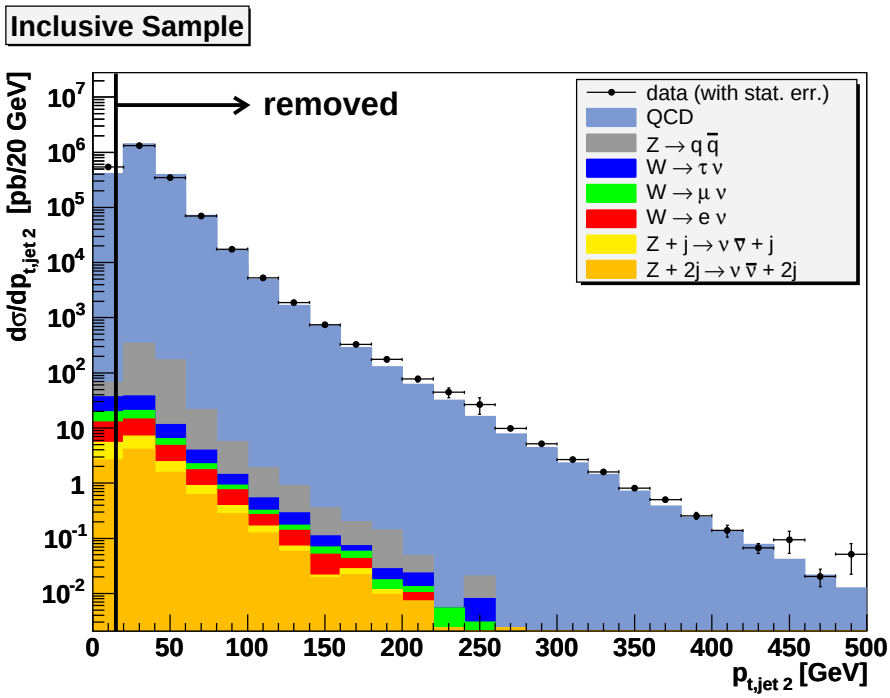

Figure 5.13: p_t distribution of second leading quality-jet within $|\eta| < 2.6$. The arrow indicates the applied cut at $p_t = 15$ GeV.

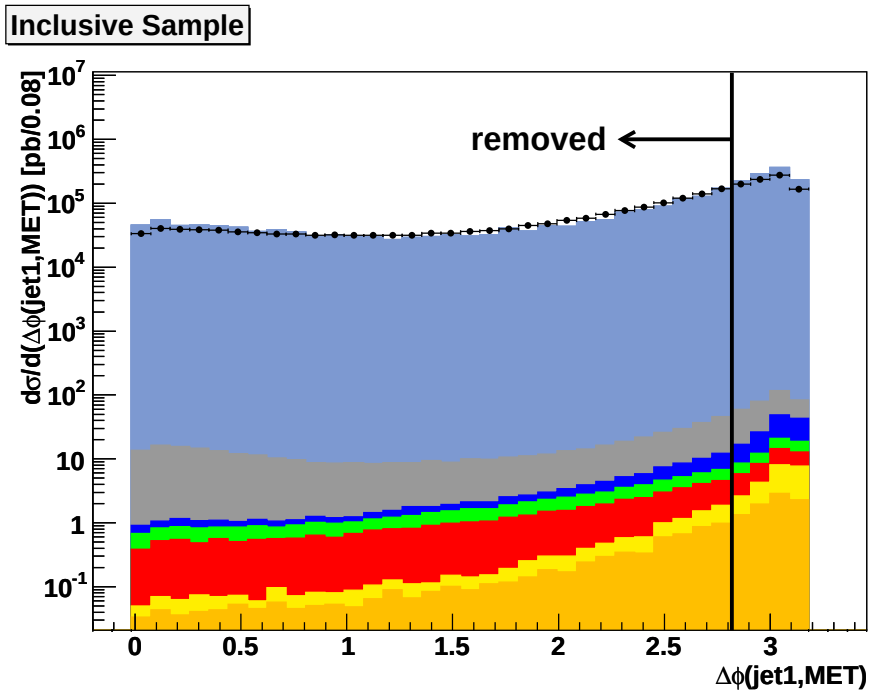

Figure 5.14: Distribution of the azimuthal angle between leading central quality-jet and MET.

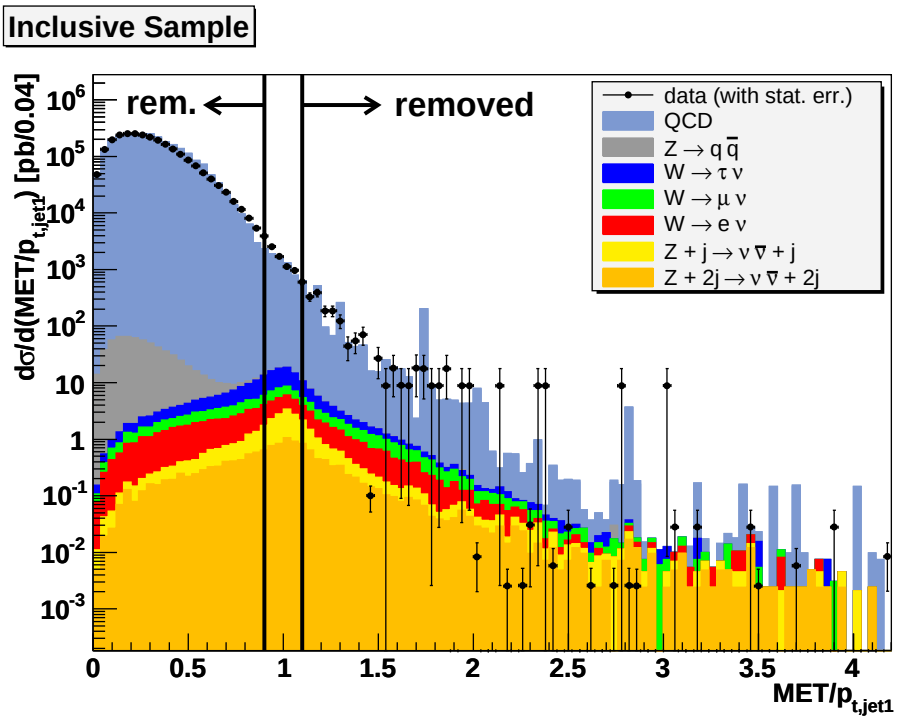

Figure 5.15: Distribution of the ratio MET/$p_{t,jet1}$.

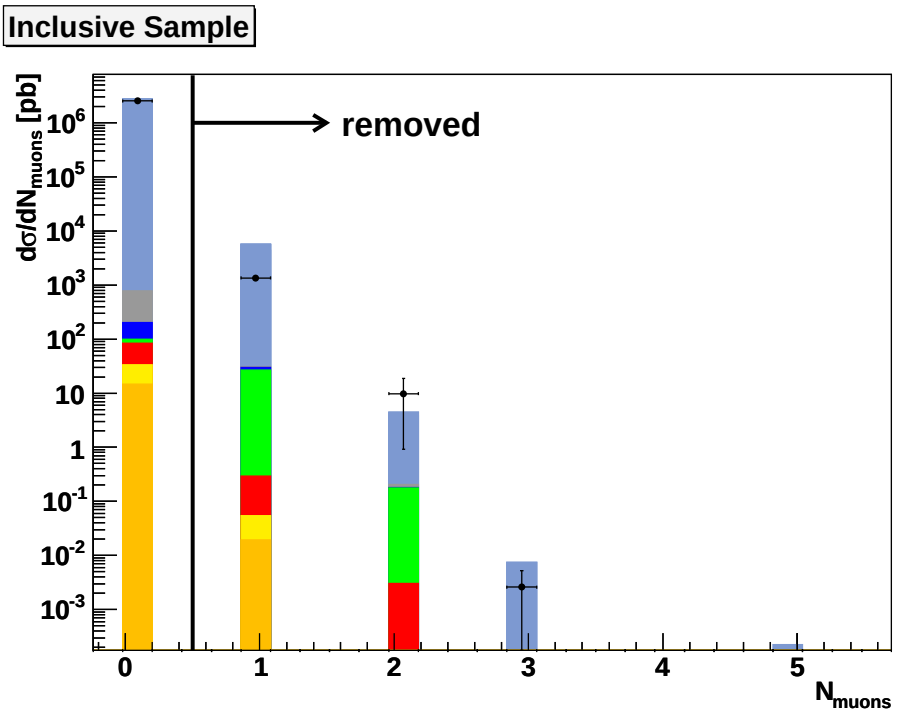

Figure 5.16: Number of isolated muons.

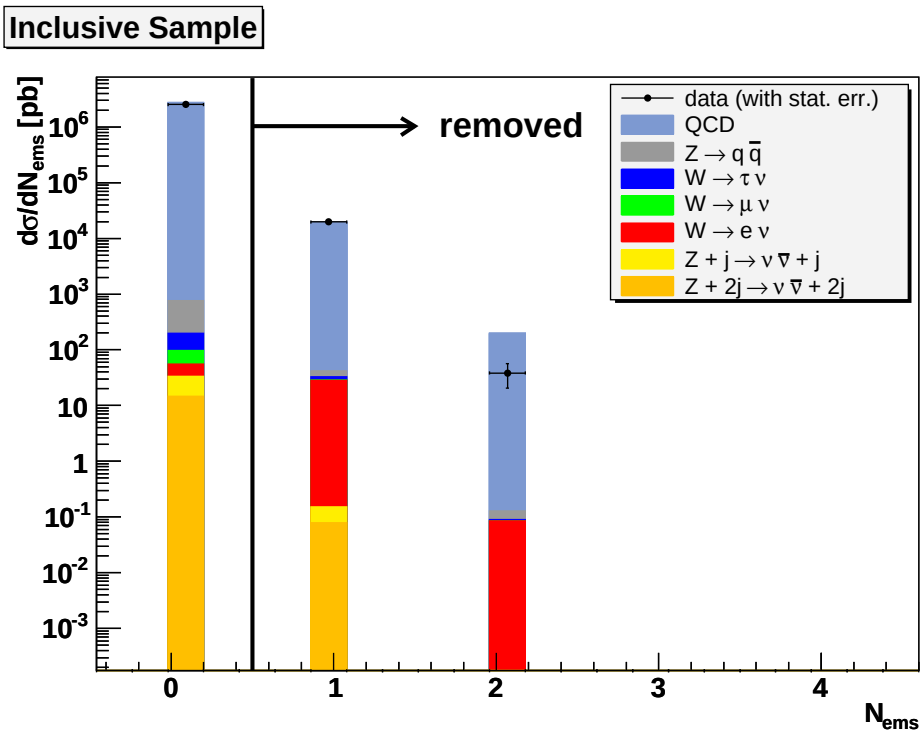

Figure 5.17: Number of isolated photons and electrons ($N_{ems} = N_{pho} + N_{elec}$) with $p_t > 10$ GeV.

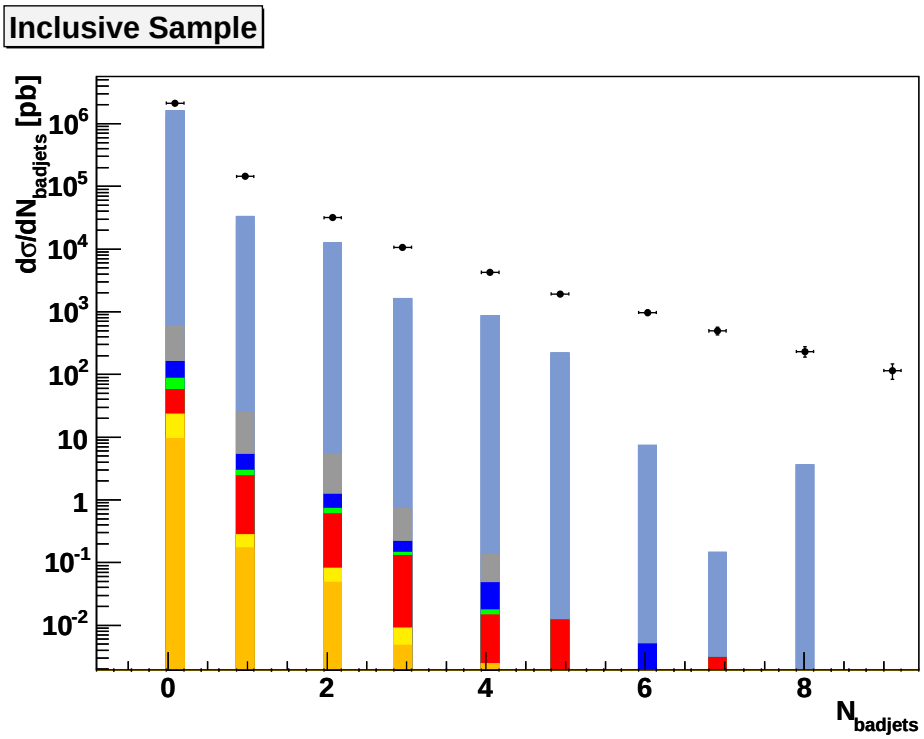

Figure 5.18: Number of bad-jets with $p_t > 15$ GeV within $|\eta| < 2.6$

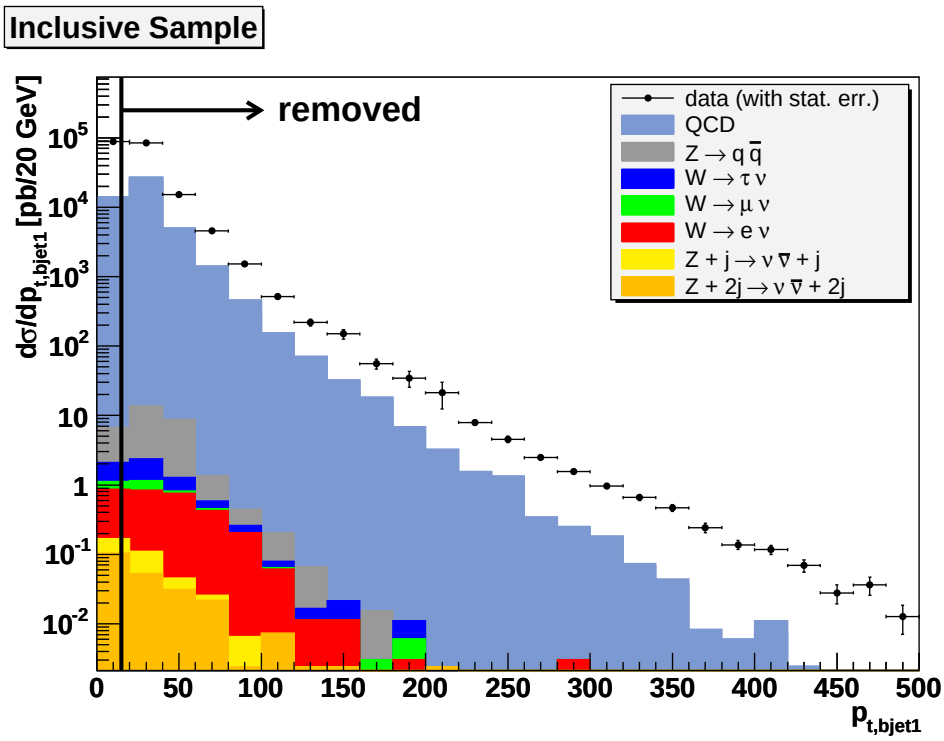

Figure 5.19: p_t distribution of leading bad-jet within $|\eta| < 2.6$.

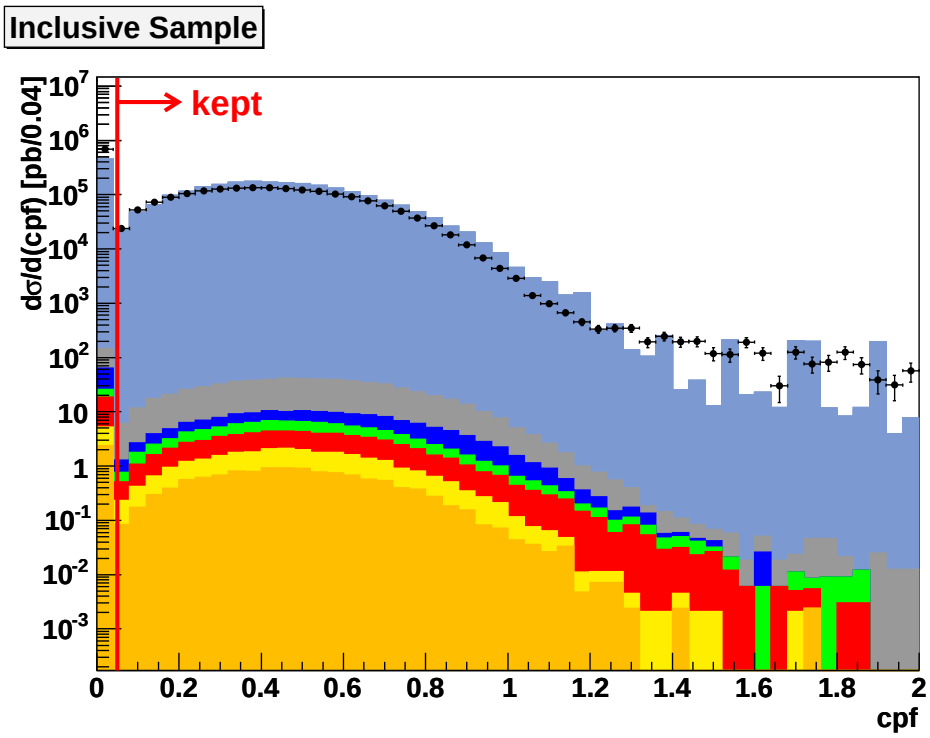

Figure 5.20: Charged particle fraction (cpf) of leading central quality-jet. In case of failing the track-jet matching condition, cpf was set to zero.

5.6 Final Mono-Jet Sample

The p_t distribution of the leading central quality-jet after the application of cuts 1-6 is shown in Fig. 5.21 and Fig. 5.22.

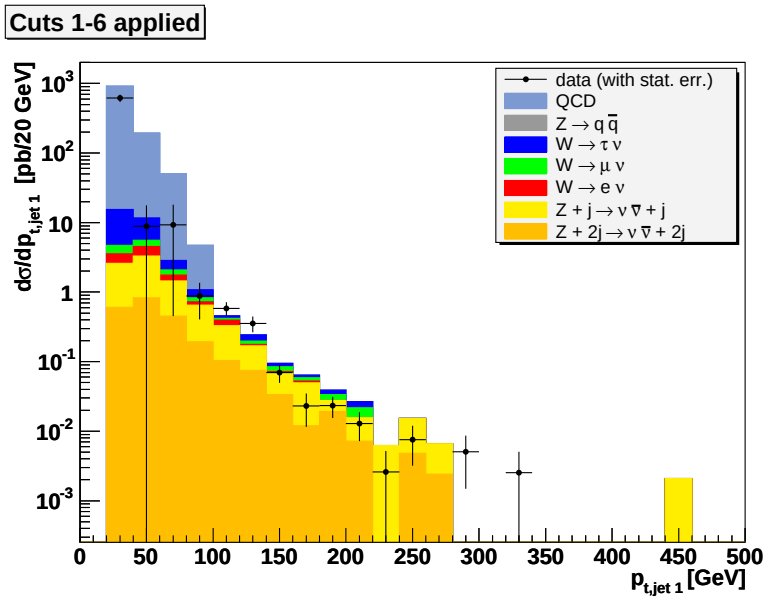

Figure 5.21: p_t distribution of the leading central quality-jet after the application of cuts 1-6.

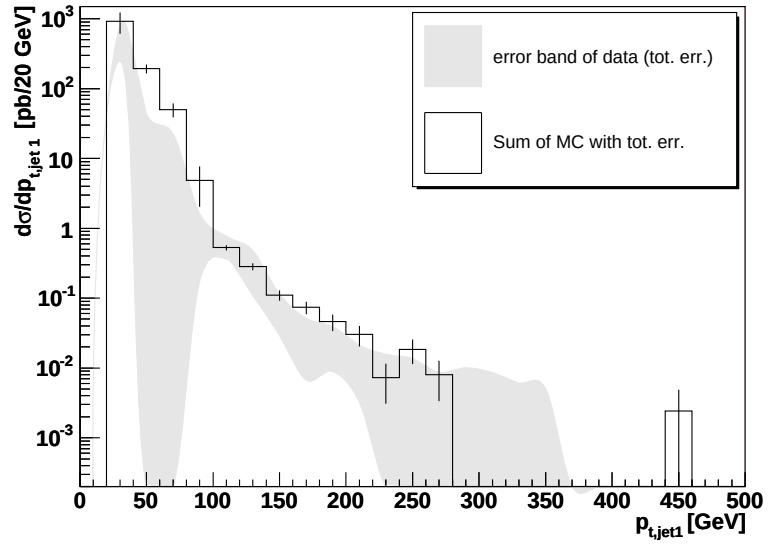

Figure 5.22: Like Fig. 5.21, but with total errors of data and MC. The grey band indicates upper and lower bounds of the total error of data. The histogram represents the sum of MC samples (compare with Fig. 5.21). Perpendicular bars indicate the total error of MC.

Remarks :

p_t regions with reasonable statistics in data and MC ($p_t < 40$ GeV and $p_t > 120$ GeV) show good agreement within the total errors (Fig. 5.21).

The region (60 - 120 GeV) exhibits either bad statistics in data (60 - 100 GeV) or in Monte Carlo (80 -100 GeV). No agreement within the total errors, but also no excess of data events is found here.

The integral of the differential cross section with respect to the interval $p_t \in [30\ GeV, \infty]$ yields

- for data :

$$\sigma_{[30,\infty],data} = 638\ \pm 75\ (stat)\ \pm 41\ (lum)\ \pm^{191}_{381}\ (JES)\ pb$$
$$= 638\ \pm^{210}_{391}\ (\text{tot})\ pb$$

- for MC :

$$\sigma_{[30,\infty],MC} = 1168\ \pm 311\ (stat)\ \pm 130\ (sys)\ pb$$
$$= 1168\ \pm 337\ (\text{tot})\ pb$$

These values agree within the total error.

The integral with respect to the interval $p_t \in [100$ GeV, $\infty]$ yields

- for data :

$$\sigma_{[100,\infty],data} = 1.09\ \pm 0.16\ (stat)\ \pm 0.07\ (lum)\ \pm^{0.35}_{0.49}\ (JES)\ pb$$
$$= 1.09\ \pm^{0.39}_{0.52}\ (\text{tot})\ pb$$

- for MC :

$$\sigma_{[100,\infty],MC} = 1.11\ \pm 0.06\ (stat)\ \pm 0.04\ (sys)\ pb$$
$$= 1.11\ \pm 0.07\ (\text{tot})\ pb$$

These values already agree within the statistical errors.
Charged mono-jets with the highest found p_t values are shown in appendix A.4.

5.6.1 Neutral Mono-jets

It is worthwhile to take a look at the p_t distribution of mono-jets failing the track-jet confirmation (cut 6), shown in Figures 5.23 and 5.24.

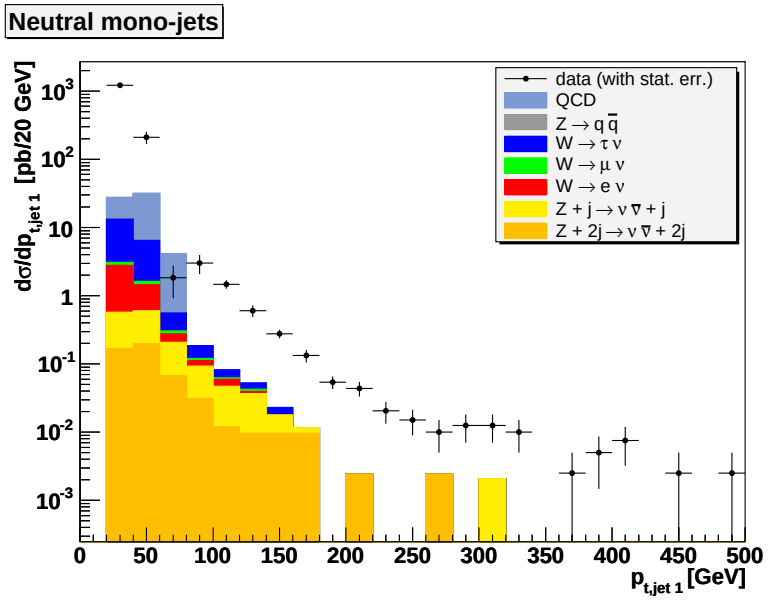

Figure 5.23: p_t distribution of leading central quality-jet after the application of cuts 1-5, but failing the track-jet confirmation (neutral mono-jets).

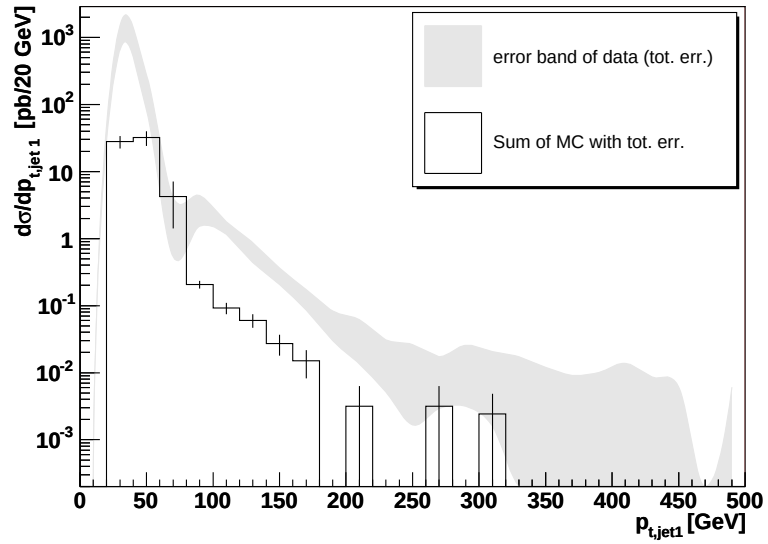

Figure 5.24: Like Fig. 5.23 , but with total errors of data and MC. The grey band indicates upper and lower bounds of the total error of data. The histogram represents the sum of MC samples (compare with Fig.5.23) with the total error of MC (perpendicular bars).

We call these mono-jets, **neutral mono-jets**.

Remarks :

The low p_t region (30 - 60 GeV) reveals a huge excess in data events with respect to the Standard Model prediction. This excess is not covered within the total errors (see integral below).
The region starting from 60 GeV reveals a huge excess as well but unfortunately the QCD Monte Carlo exhibits bad statistics and thus it can not be excluded that the excess is in accordance with the Standard Model prediction.

The integral of the differential cross section with respect to the interval $p_t \in [30\,GeV, 60\,GeV]$ yields

- for data :

$$\sigma_{[30,60],data} = 1430 \ \pm 112 \ (stat) \ \pm 93 \ (lum) \ \pm^{316}_{675} \ (JES) \ \ pb$$

$$= 1430 \ \pm^{348}_{691} \ (\text{tot}) \ \ pb$$

- for MC :

$$\sigma_{[30,60],MC} = 60 \ \pm 10 \ (stat) \ \pm 5 \ (sys) \ \ pb$$

$$= 60 \ \pm 11 \ (\text{tot}) \ \ pb$$

The actual reason for applying the track-jet confirmation was to exclude noise-jets, but in addition to that neutral mono-jets may also be caused by atmospherical muons, whose impact could not be excluded entirely or even from processes from beyond the Standard Model. It was not attempted to seperate these possible contributions.

5.7 Summary and Conclusion

In this thesis the first wide p_t range investigation of mono-jets starting from 30 GeV was presented.
For this purpose the notion "mono-jet event" was motivated and defined and possible sources of such events were discussed. To be able to compare the number of observed events with the ones expected from the Standard Model, these sources were accounted for by simulated events or if no simulations were available, reduced as far as possible.

Starting from a general jet data sample, the final mono-jet sample was approached by applying the definition and reducing unsimulated sources.

The final mono-jet sample (charged mono-jets) revealed no excess in data with respect to the Standard Model prediction. The total cross section $\sigma_{[30,\infty]}$ found for data and Monte Carlo agreed within the total errors.

In case of neutral mono-jets an excess of data events with respect to the Standard Model prediction was found. This excess most likely originates from unsimulated noise-jets. However, other sources like atmosherical muons or neutral mono-jets from beyond the Standard Model could not be excluded.

Appendix A

A.1 Units, Coordinate System, Quantities, Conventions

- **Units :**

  All quantities are displayed in natural units. These are defined by setting :

  $$\hbar = 1$$

  $$c = 1$$

  This implies :

  $$[energy] = [mass] = [momentum] = [time^{-1}] = [length^{-1}]$$

  Thus all important quantities can be displayed in units of energy and energy^{-1} respectively. The chosen unit for energy is eV

  $$1eV := 1,602176462(63) \cdot 10^{-19} J$$

  Examples :

  $$1m \simeq 5 \cdot 10^{6} eV^{-1}$$

  $$1s \simeq 1.5 \cdot 10^{15} eV^{-1}$$

- **Coordinate System :**

  The nominal interaction point is chosen to be the origin of the coordinate system. Besides the cartesian system (x, y, z) the combination of (ϕ, η, z) is commonly used, where

  $$\phi := \arctan(\frac{x}{y}) \quad \text{the azimuthal angle}$$

  and

  $$\eta := -\ln(\tan(\frac{\Theta}{2})) \quad \text{the pseudorapidity}$$

  (see also Fig. 2.11).

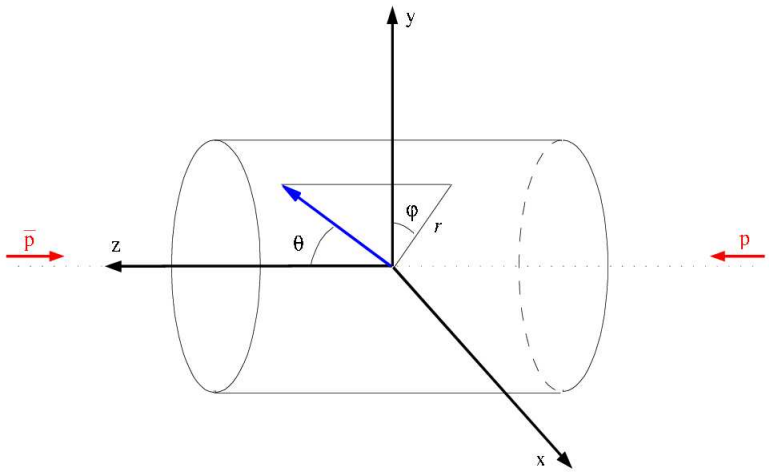

Figure A.1: DØ coordinate system taken from [50].

- **Separation $\Delta\mathcal{R}$**

  Definition :

  $$\Delta\mathcal{R} := \sqrt{(\Delta\phi)^2 + (\Delta\eta)^2}$$

  The separation measures the distance between directions in (η, ϕ)-space.

- **Transverse Momentum** p_t

  Definition :

  $$p_t := \sqrt{(p_x)^2 + (p_y)^2}$$

  where p_x and p_y are the components of the momentum with respect to the x and y axis.

A.2 Request IDs of Monte Carlo Samples

MC Sample	request IDs
$Z + jet \to \nu\bar{\nu} + jet$	18035,18380,18696,18697
$W \to \tau\nu$	12289,12290,12299,12300,12301
$W \to \mu\nu$	12520,12519,12518,12517,12516,12502,12501,12500
$W \to e\nu$	12438,12437,12436,12435,12434,12433,12432,12431,12430,12429
$Z/\gamma^* \to q\bar{q}$:	13359,13356,14181,14180,14178
$Z + 2jet \to \nu\bar{\nu} + 2jet$	18355,18354,18037,18039
QCD	
$10 < \hat{p}_t < 20$	15404,15488
$20 < \hat{p}_t < 40$	15382
$40 < \hat{p}_t < 80$	13324,13325,13326,13368,13369,13370,13371,13702,13703
$80 < \hat{p}_t < 160$	13327,13328,13330,13372,13373,13374,13375
$160 < \hat{p}_t < 320$	13331,13332,13377
$320 < \hat{p}_t < 960$	13378

A.3 The Event Display

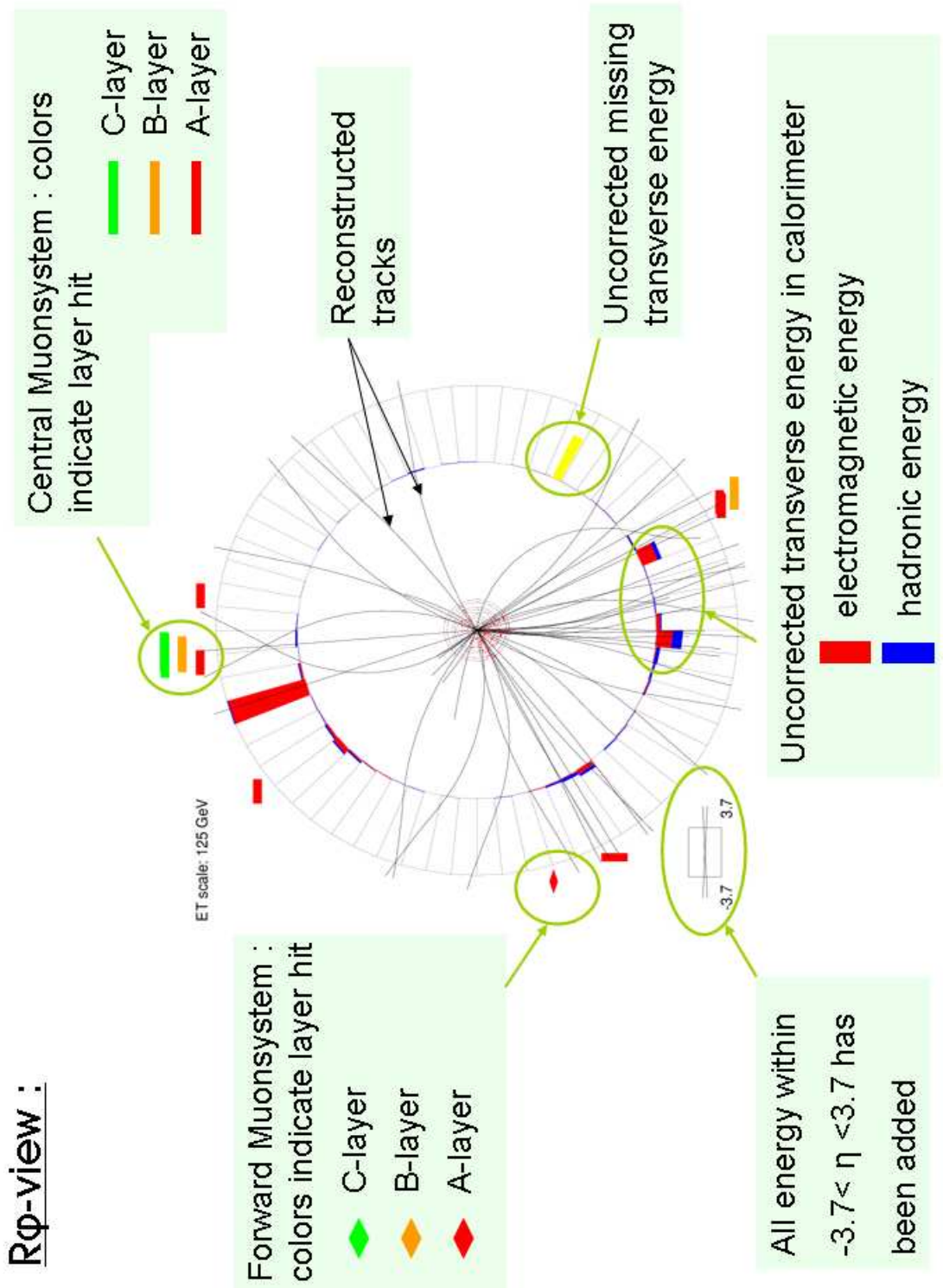

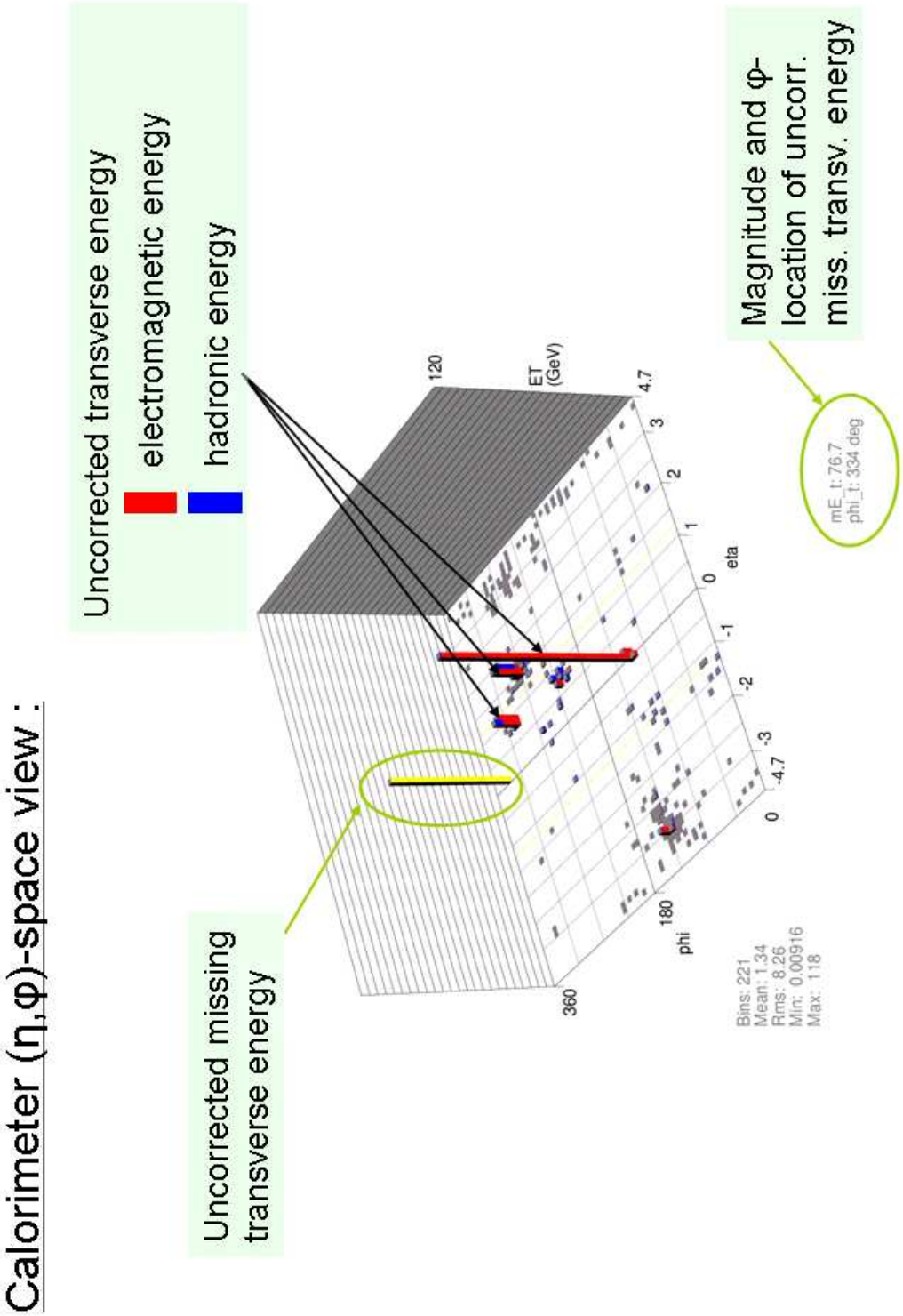
Calorimeter (η,φ)-space view :
Uncorrected transverse energy
electromagnetic energy
hadronic energy
Uncorrected missing transverse energy
Magnitude and φ-location of uncorr. miss. transv. energy
ET (GeV)
120
4.7
3
2
1
0
-1
-2
-3
-4.7
eta
0
180
360
phi
mE_t: 76.7
phi_t: 334 deg
Bins: 221
Mean: 1.34
Rms: 8.26
Min: 0.00916
Max: 118

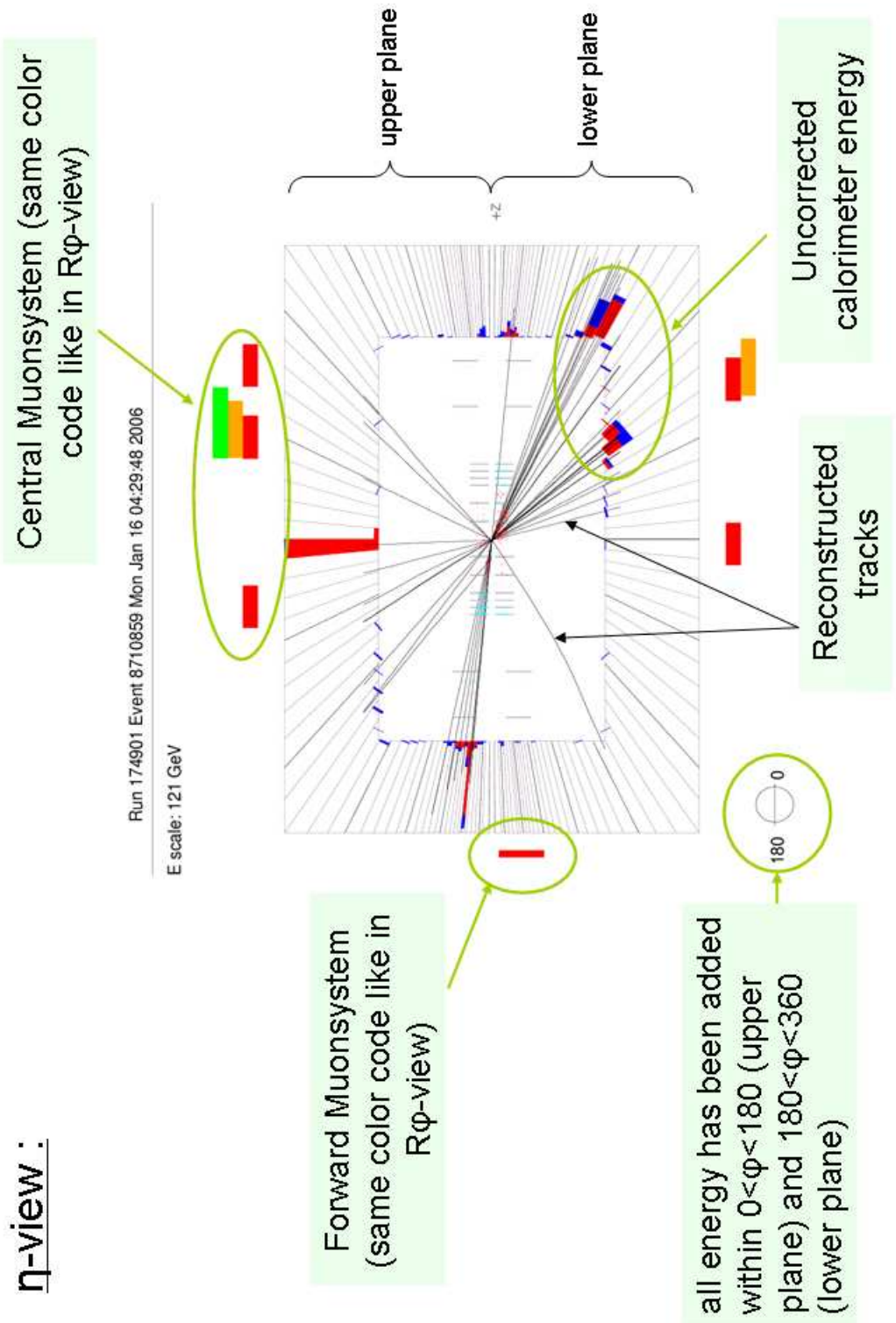
η-view :
Central Muonsystem (same color code like in Rφ-view)
Run 174901 Event 8710859 Mon Jan 16 04:29:48 2006
E scale: 121 GeV
upper plane
lower plane
+z
Uncorrected calorimeter energy
Reconstructed tracks
Forward Muonsystem (same color code like in Rφ-view)
all energy has been added within 0<φ<180 (upper plane) and 180<φ<360 (lower plane)
0
180

A.4 Highest p_t charged Mono-jet Events

1.) $\mathbf{p_t}$**= 337 GeV** (corrected) :

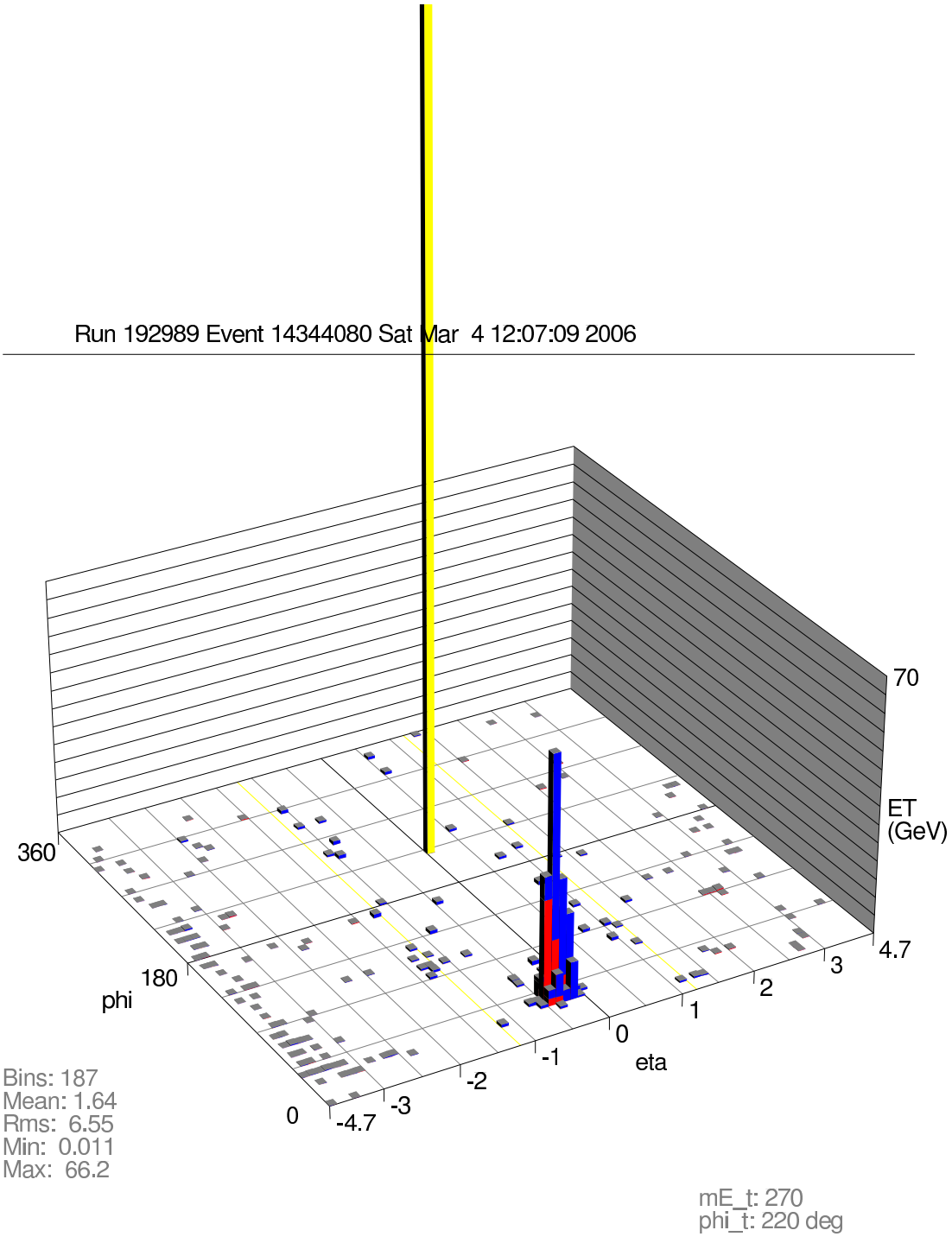

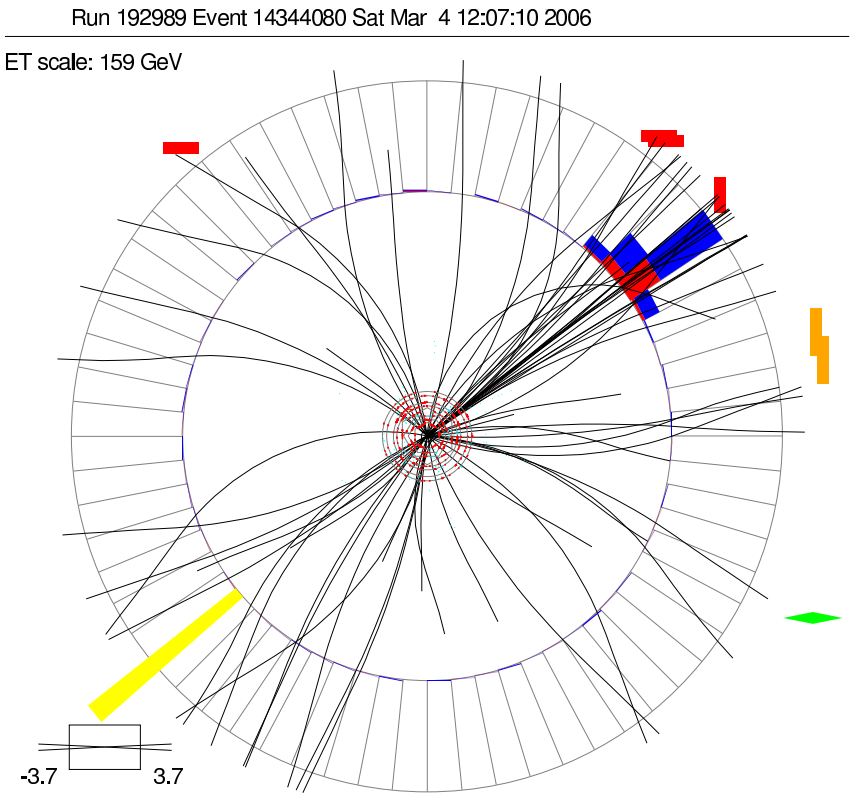
Run 192989 Event 14344080 Sat Mar 4 12:07:10 2006
ET scale: 159 GeV
-3.7
3.7

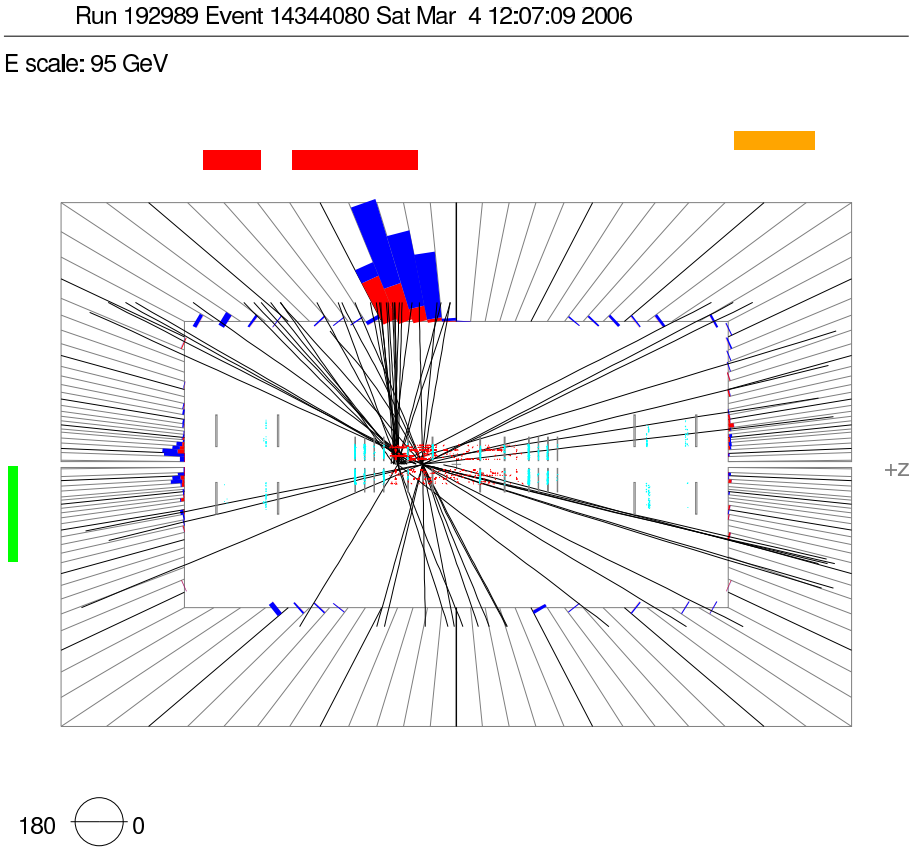
Run 192989 Event 14344080 Sat Mar 4 12:07:09 2006
E scale: 95 GeV
+Z
180
0

2.) $\mathbf{p}_t$**= 290 GeV** (corrected) :

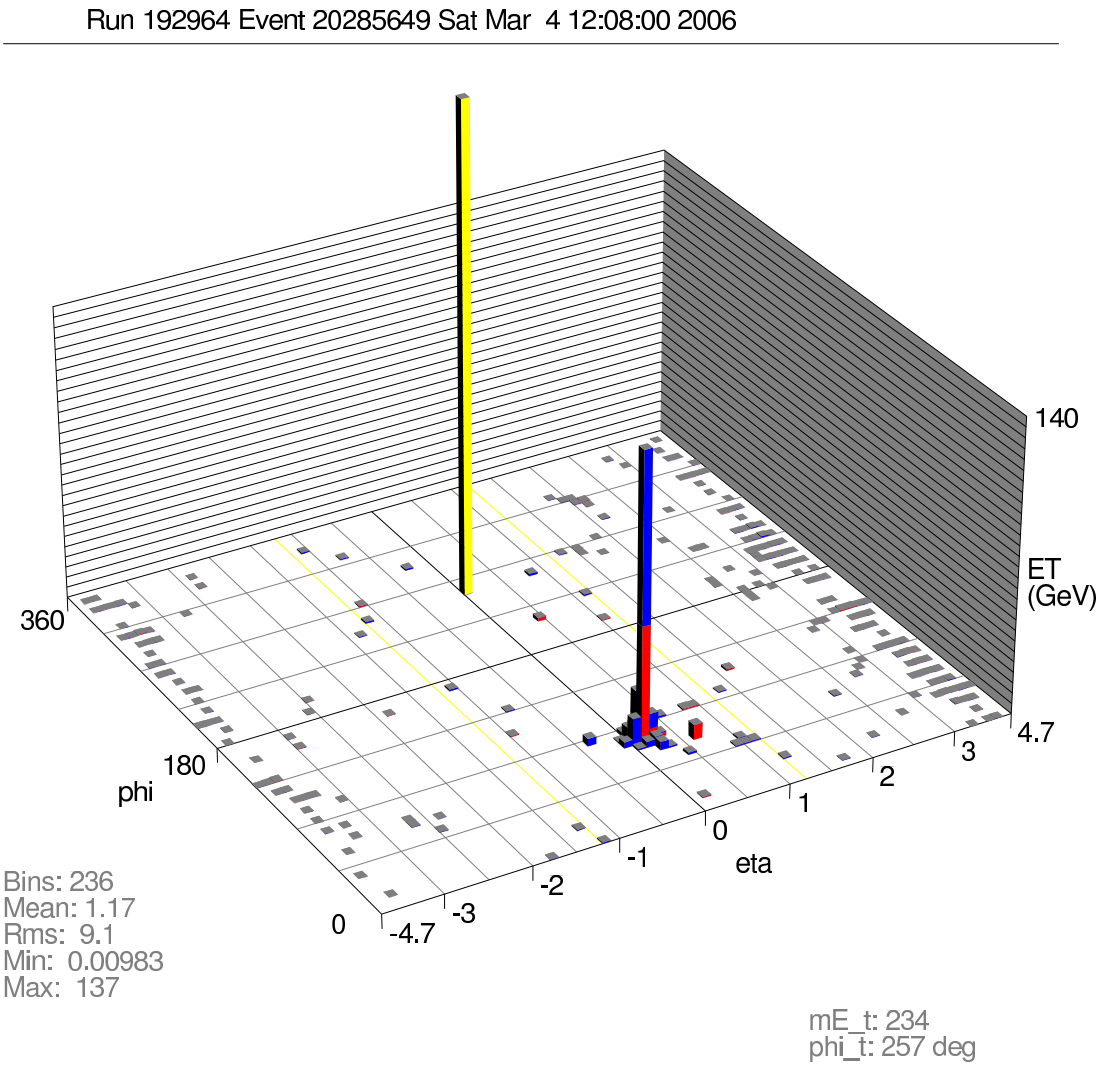

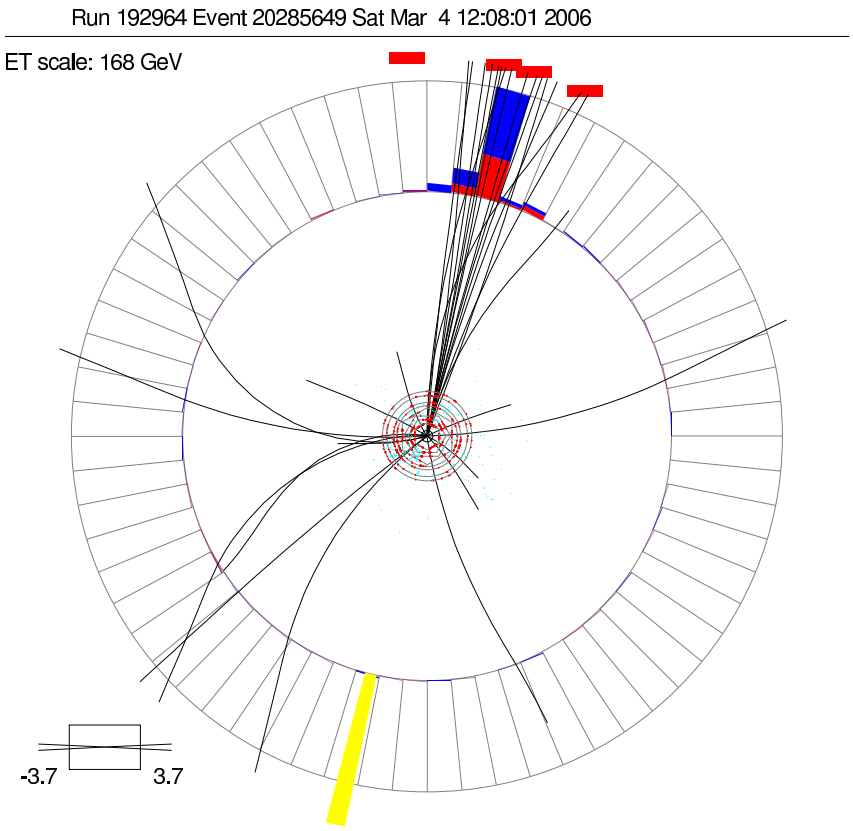
Run 192964 Event 20285649 Sat Mar 4 12:08:01 2006
ET scale: 168 GeV
-3.7
3.7

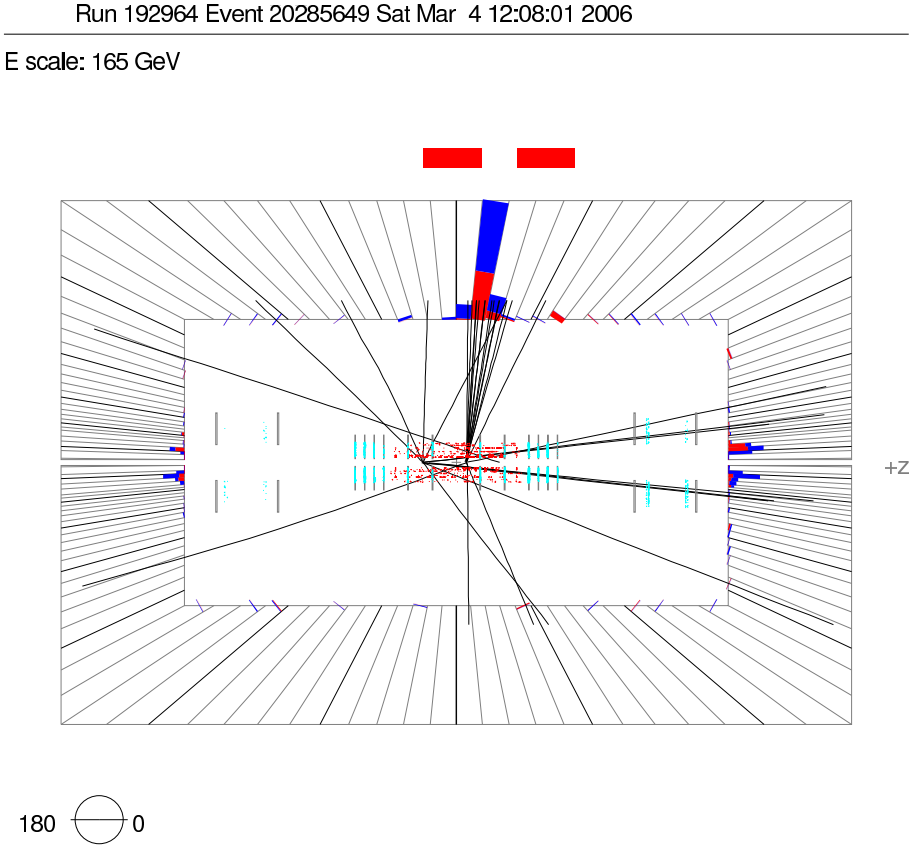
Run 192964 Event 20285649 Sat Mar 4 12:08:01 2006
E scale: 165 GeV
+z
180
0

Bibliography

[1] Affolder T. et al. (CDF Collaboration) "Search for Kaluza-Klein Graviton Emission in $p\bar{p}$ Collisions at $\sqrt{s} = 1.8$ TeV Using the Missing Energy Signature" hep-ex/0309051

[2] Abazov V. et al. (DØ Collaboration) "Search for Large Extra Dimensions in the Monojet + MET Channel with the D Detector" Phys.Rev.Lett. 90, 251802 (2003)

[3] http://www-d0.fnal.gov/runcoor/RUN/run2_lumi.html

[4] Begel M. "DØ Luminosity in Run 2: Delivered" DØ Note 3970

[5] http://www-d0.fnal.gov/Run2Physics/displays/presentations/

[6] Petroff P. "DØUpgrade For Run II" hep-ex/9910028

[7] Nurse E. "A measurement of the Inclusive $Z\gamma^* -> \mu^+\mu^-$ Cross Section and Study of W and Z Events" PhD thesis

[8] Petroff P. "DØUpgrade For Run II" hep-ex/9910028

[9] http:www-d0.fnal.gov/Run2Physics/WWW/drawings/

[10] Parashar N. "The DØ Detector at the Fermilab Tevatron in Run 2" hep-ex/0202047

[11] http:www-d0.fnal.gov/Run2Physics/WWW/drawings/

[12] Kotcher J. "Design, Performance and Upgrade of the DØ Calorimeter" Fermilab-Conf-95/007-E

[13] Electron Identification Page http://www-d0.fnal.gov/phys_id/emid/d0_private /certification/main_v2_2_1.html

[14] DØ Collaboration, Abazov V.M. et al. "Search for Large Extra Dimensions in the Monojet + Missing E_T Channel with the DØ Detector" Phys.Rev.Lett. 90 (2003) 251802

[15] "The muon system of the Run II DØ Detector " Nuclear Instruments and MEthods in Physics Research A552 (373-398)

[16] Abazov V.M. et al. "The Muon System of the Run II DØ Detector" Fermilab-PUB-05-034-E

[17] Zhou B. et al. "Parametrized Monte Carlo Simulation Muon" DØ Note 4065

[18] Edwards T. et al. "The updated DØ Luminosity Determination" DØ Note 4328

[19] Begel M. et al. "DØ Luminosity in Run2 : Delivered " D0-Note 3970

[20] http://www-d0.fnal.gov/trigger_meister/private/www/tl_desc/global.html

[21] Eidelman S. et al "Review of Particle Phhysics " Physics Letters B 592, 1(2004)

[22] Peskin M. E.,Schroeder D. V. "An Introduction to Quantum Field Theory" Westview Press

[23] Veltman M. "Diagrammatica. The Path to Feynman Diagrams" Cambridge University Press

[24] Schmueser P. "Feynman-Graphen und Eichtheorien fuer Experimentalphysiker" Springer Verlag

[25] Arkani-Hamed N. et al "The Hierarchy Problem and New Dimensions at a Millimeter" hep-ph/9803315

[26] Arkani-Hamed N. et al "Phenomenology, Astrophysics and Cosmology of Theories with Sub-Millimeter Dimensions and TeV Scale Quantum Gravity" hep-ph/9807344

[27] Guidice G.F. et al. "Quantum Gravity and Extra Dimensions at High-Energy Colliders" hep-ph/9811291

[28] Blazey G.C. et al."Run II Jet Physics" FERMILAB-Conf-00/092-E

[29] http://www-d0.fnal.gov/phys_id/emid/d0_private/certification/welcome.html

[30] http://www-d0.fnal.gov/computing/algorithms/calgo/met/met_cor_doc.html

[31] http://www-d0.fnal.gov/phys_id/muon_id/d0_private/certif/p14/index.html

[32] hep-ph/0005114 Summary report of the QCD and Standard Model Working Group

[33] Sjoestrand T. et al. "PYTHIA 6.2 Physics and Manual" hep-ph/0108264

[34] Fisyak Y., Womersley J. "D0gstar D0 GEANT Simulation of the Total Apparatus Response" (http://d0sgi0.fnal.gov/d̃0upgrad/d0_private/software/montecarlo/d0gstar/tex/manual.ps) DØ-Note 3191.

[35] http://www-d0.fnal.gov/computing/MonteCarlo/simulation/d0sim.html

[36] Metzger W.J. "Statistical Methods in Data Analysis" Katholieke Universiteit Nijmegen

[37] Busato E. "Jet Algorithms in the DØ-Run II Software : Description and User's Guide" DØ-Note 4457

[38] Brun R. et al. "Root. An object orientated Data Analysis Framework" http://root.cern.ch/

[39] Klute M., Phaf L. and Whiteson D. "TopAnalyze - A Framework Analyze Package For Top Group Analyses" DØ-Note 4122

[40] Offline Run Quality Database http://d0db-prd.fnal.gov/qualitygrabber

[41] JET/MET group http://www-d0.fnal.gov/computing/algorithms/calgo/jet_met /run-sel.html

[42] Runrange_luminosity http://www-d0.fnal.gov/d0dist/dist/packages/lm_access /devel/doc/runrange_luminosity.html

[43] Schwartzman A. "Track-jet studies Using a 3-Dimensional Simple Cone Jet Algorithm" D0-Note 3919

[44] "Beam Tests of the D0 Uranium Liquid Argon End Calorimeter" Fermilab-pub-92/162-E

[45] DØ Collaboration "The Upgraded DØ Detector" arXiv:physics/0507191 v1

[46] http://www-ese.fnal.gov/SVX/Production/SVX_WEB/CPC/barrel/barrel24.jpg

[47] http://d0server1.fnal.gov/projects/silicon/run_2a/d0smtproduction/images/D0-BA-4%20mating/P1010021.jpg

[48] EM ID Certification Results http://www-d0.fnal.gov/phys_id/emid/d0_private/certification/welcome.html

[49] Chapin D. et al. "Measurement of Z-¿ee and W-¿enu Production Cross Sections with —eta—¡2.3" DØ Note 4403

[50] Busato E., Andrieu B. "Jet Algorithms in D0 RunII Software: Description and User's Guide" DØ Note 4457

[51] Kluge T., Rabbertz K., Wobisch M. "Fast NLO, Frontiers in Contemporary physics"

[52] Han T. Lykken J.D. Zhang R. "Kaluza-Klein States from LArge Extra Dimensions" hep-ph/9811350

[53] Kowalczyk S. et al. "Constraints on Large Extra Dimensions"

[54] Martin St. P. "A Supersymmetry primer" hep-ph/9709356

[55] http://www-clued0.fnal.gov/%7Enunne/cross-sections/caps_xsect.html

[56] http://www-d0.fnal.gov/phys_id/jes/d0_private/certified/v5.3/links.html

[57] Miao C. "The DØ Run II Luminosity Monitor" DØ Note 3573

[58] The DØ Collaboration "Measurement of the Inclusive Jet Cross Section in $p\bar{p}$ Collisions at $\sqrt{s} = 1.96$ TeV" DØ Note 4751.

[59] http://www-d0.fnal.gov/computing/MonteCarlo/

[60] Calorimeter Data Quality Page http://d0-france.in2p3.fr/WORKING_GROUPS/DQ/

[61] Nunnemann T. "NNLO Cross-Sections for Drell-Yan,Z and W Production using Modern Parton Distribution Function" DØ Note 4476

[62] Mangano M.L. "ALPGEN, a generator for hard multiparton processes in hadronic collisions" hep-ph/0206293.

Acknowledgements

In the first place I'd like to thank my grandparents and my mother. They supported me throughout my life and never doubted my abilities even when I was taking the wrong turns. And finally they were right ! Damn.

The list of people who made this work possible is endless.

First I must thank the head of the institute Prof.Dr.Thomas Hebbeker. He gave me this intriguing task and remained calm and positive even when things were not looking so good for me. He also gave me the opportunity to join the place where big science is gathered at Fermilab in Chicago.

As well I'd like to thank Prof.Dr.Martin Erdmann for agreeing to be my second-referee.

For supporting my daily work at the institute I must thank Daniela Käfer, Carsten Magass, Steffen G. Kappler, Jan W. Coenen and especially Christian Autermann and Volker Vorwerk, my cubicle mates.

For doing the same but from the other side of the Atlantic Ocean I thank Dr. Arnd Meyer, who always gave straight answers to not so straight questions.

For Root [**?**] and Latex [**?**] support I thank Carsten Hof. For giving me advices right in the beginning of my work I thank Lotte Wilke.

At Fermilab I owe thanks to : Todd Adams, Christophe Royon, Patrice Verdier, Jean-Francois Grivaz, Miroslav Kopal, Jyothsna Rani, Jonas Strandberg, Amnon Harel, Quentin Hanserino, Emmanuel Busato, Ann Heinson, Angela Bellavance, Markus Wobisch and Stefan Anderson for steadily answering my questions.

For proof-reading my thesis I thank again Carsten Magass, Volker Vorwerk and Daniel Lenz.

For helping me to fill out forms and booking flights I thank Irene Gojdie and Frau Rosewick.

For providing a vital part of the III.A atmosphere I thank Tanja Rommerskirchen, Clemens Zeidler, Philipp Biallass, Georg Altenhöfer and Michael Bontenackels.

Special thanks go to Prof. Dr. Jiri Jersak for his nice lectures and comprehensible explanations.

My final "thank you" though, goes out to a flower I recently met and I'm looking forward to spend some time again (In case she wants!).